University of Leoben

Coating Development for Piston Rings

Diploma thesis

by

Andrea Bachmaier
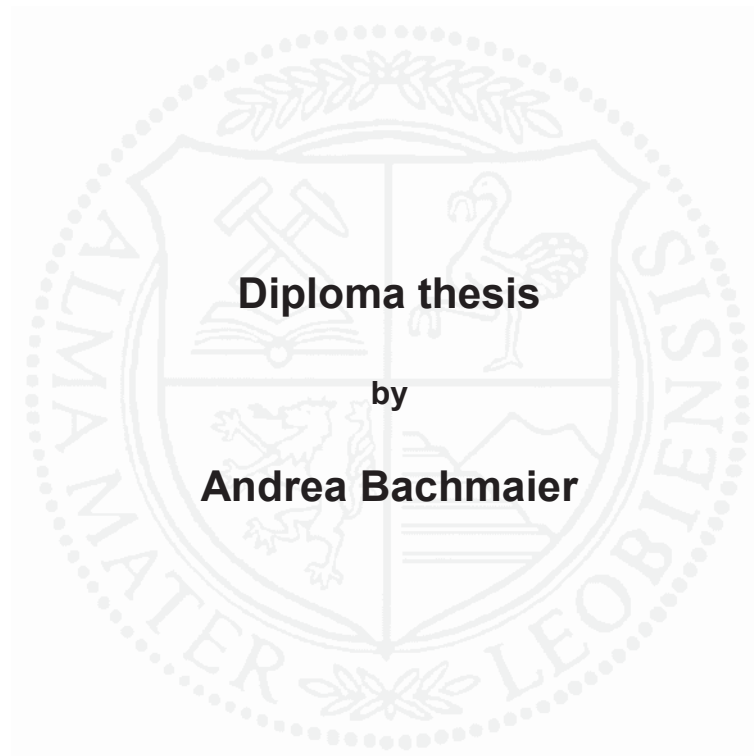
This work has been carried out in cooperation with MAHLE GmbH at the Department of Physical Metallurgy and Materials Testing, University of Leoben, Austria

Leoben, February 2008

I declare in lieu of oath, that I wrote this thesis and performed the associated research myself, using only literature cited in this volume.

Leoben, February 2008

Acknowledgements

I don't want to achieve immortality through my work,

I want to achieve it through not dying.

(Woody Allen)

Contents

List of Abbreviations

Lower Case Letters

at.%   atomic percent
fcc   face-centered cubic

Capital Letters

BSTM   Biaxial stress temperature measurement
CBM   Conventional balanced magnetron
DC   Direct current
DIN   Deutsches Institut für Normung
E   Elastic modulus
EDX   Energy dispersive X-ray
JCPDS   Joint Committee on Powder Diffraction Standards
H   Hardness
HF 1-6   Adhesion
HRC   Rockwell hardness loading mode C
HSS   High-speed steel
K   Wear coefficient
MW   Microwave
PVD   Physical vapour deposition
RF   Radio frquency
SEM   Scanning electron microscopy
SZM   Structure zone model
UBM   Unbalanced Magnetron Sputtering
XRD   X-ray diffraction
VSI   Vertical scanning interferometry

List of Symbols

Roman, Lower Case Letters

d_{hkl}	interplanar spacing of lattice plane
d_o	distance between parallel laser beams
d_i	deflection between the reflected laser beams
f	flow rate
fcc	face centered cubic
h_1, h_2	auxiliary variables
h_p	indentation depth
l_x	length of specimen
l_y	width of specimen
p	pressure
p_{tot}	total pressure
r	radius of curvature
s	sliding distance
t	time
t_c	coating thickness
t_s	substrate thickness
u	velocity
w_{hm}	full width at half maximum
x_c	position of peak maximum

Roman, Capital Letters

A	Area
Ai/A	Area ratio
Ar	Argon atom
Ar^+	Argon ion
Di	Inner diameter of wear crater
Do	Outer diameter of wear crater
E_c	Elastic modulus of coating
E_s	Elastic modulus of substrate
$E_c \cdot \left(1 - v_c\right)^{-1}$	Biaxial elastic modulus of the coating
$E_s \cdot \left(1 - v_s\right)^{-1}$	Biaxial elastic modulus of the substrate
F	Force
F_N	Normal force
I	Current

I-V	Current-voltage correlation
K	Wear rate
P	Indentation force
R	Radius
R_a	Average roughness values
R_q	Mean square roughness
T	Temperature
T_m	Melting temperature
U	Potential
U_m	Ion etching potential
V	Worn volume

Greek Letters

α_c	linear thermal expansion coefficient of coating
α_s	linear thermal expansion coefficient of substrate
η	cauchy content
θ	diffraction angle
λ	wave length
μ	coefficient of friction
σ	electrical conductivity
σ_{int}	intrinsic stress
σ_{res}	residual stress
σ_{th}	extrinsic thermal stress
σ_{xx} σ_{yy} σ_{zz}	stress component in x, y and z direction
ρ	electrical resistance
υ_c	poison's ratio of coating

1 Introduction

The European Commission is developing new strategies to ensure that the EU meets its greenhouse gas emission targets under the Kyoto Protocol and beyond. On this regard, one of the goals is to reduce the average CO_2 emissions to 120 grams per km by 2012. Studies have shown that a substantial decrease of about 3 g/km for CO_2 emissions can be gained by reduction of internal engine friction. The discussions on the reduction of CO_2 emissions have been forcing car manufactures to find new possibilities to improve the performance of various engine components. One example is the development of new coatings for piston rings, which has been focused so far primary on carbon-based low friction coatings or hard wear resistant coatings.

A piston ring is a split metal ring which acts as a seal between the combustion chamber and the crankcase of the engine. The main function is to inhibit oil from passing into the combustion chamber and combustion gases from passing into the crankcase. Piston rings are subject to continuous growing operational demands like high wear, high temperature and high pressure. Thus, one main goal is the reduction of friction and wear. Reduced wear and friction result in better control of the oil consumption which in turn decreases oil consumption, and consequently, emissions are also reduced. To enhance the performance of piston rings, which are made from wear resistant material such as cast iron or steel, they are additionally nitrided or coated. At the moment, a multitude of coatings are used such as chromium or chromium-nitride coatings, which are basically manufactured by electro-plating or thermal spraying. Another method is the fabrication of coatings by Physical Vapour Deposition (PVD) techniques. For example, 30-40 µm thick chromium-nitride coatings deposited by arc-evaporation are used for highly-stressed piston rings. Although the wear resistance is improved at room temperature, these coatings show high wear at temperatures above 200℃ which can be related to their open, porous structure.

The present work was designed to develop new coating concepts for piston rings based on an optimisation of the CrN-coatings in use. To improve the performance of these coatings, porosity must be reduced and resistance against oxidation as well as abrasive wear must be enhanced. It is known that hardness as well as oxidation and abrasive wear resistance are improved by alloying Al to CrN [1]. High Al contents in CrN coatings result in high hardness but also in high residual stresses which limits the deposition of thick films. Therefore, $Cr_{1-x}Al_xN$ coatings with Al contents x ≤ 0.25 should be deposited in this work.

Secondly, the coatings should show low friction, low wear and also self-lubricating properties in a temperature range from 200℃ to 500℃, which might be the actual

working temperature of piston rings. It is known that self-lubricating properties of AlCrN coatings above 600℃ are improved by alloying vanadium due to the formation of vanadium oxide films on the coating surface [2]. To optimize the performance of piston rings, vanadium alloyed CrAlN coatings are not suitable for several reasons like the too high formation temperature of vanadium oxide or possible reactions of vanadium with combustion gases. Hence, the properties of the CrAlN coatings must be improved by alloying with other elements. Alternative choices might be rhenium or niobium. Both elements form oxides (Re_2O_7, Nb_2O_5) with self-lubricating properties above a temperature of 200℃. Another possibility is silver, which enhances the self-lubricating properties in a temperature range from 400℃-500℃ [5].

The aim of this work is to deposit CrAlN coatings with different concentrations of silver, niobium and rhenium by reactive sputtering using a laboratory-scale unbalanced DC magnetron sputtering system. Structure, composition as well as mechanical properties such as hardness, elastic modulus, electrical resistance and adhesion of these coatings are subsequently characterized. Furthermore, the tribological behaviour and residual stresses of the coatings are investigated

2 Theoretical Background

2.1 Physical Vapour Deposition

2.1.1 General

Physical vapour deposition (PVD) is a technology which allows the thin-film deposition of a very large number of inorganic materials like metals, alloys, compounds, mixtures, metal oxides, nitrides and carbides as well as some organic materials on almost any technically relevant substrate. Developed in the 1960s, there is a wide range of different versions of PVD techniques. All of them are based on the use of various physical phenomena taking place under vacuum conditions [4-6].

The first step in the PVD process includes the transition of a liquid or solid phase to the vapour phase. There are different possibilities to obtain the vapour phase of the material source: thermal evaporation by induction, resistance, electron beam, arc or laser heating; thermal sublimation (continuous or pulsed arc discharge) and sputtering (conventional or magnetron). The next step is the transport of the vapour phase to the substrate; and afterwards, condensation, film nucleation and growth take place [4, 5, 7].

A classification of PVD processes can be made, for example, based on the deposition technique, differentiating between evaporative deposition, ion plating and sputtering (see Fig. 2.1). Another possibility is to classify into plasma assisted and non-plasma assisted processes.

In the **evaporation deposition process**, the coating material is heated by various methods in vacuum until it evaporates. Assuming that vacuum is high enough (10^{-3} to 10^{-6} Pa), there is nearly no particle interaction during the transport to the substrate and therefore, the particles are not deflected before they are deposited. The evaporation rates are high and the coatings have an evenly distributed coating thickness with sufficient adhesion. Depending on power density and possible chemical reactions between source material and evaporant, different variations of the evaporation deposition processes have been developed, e.g. arc evaporation [4, 7].

In the **sputtering process**, the coating material is continuously hit by ions with high kinetic energy. As a result of this constant bombardment, the surface atoms transform directly ejected from the solid into the vapour phase. To induce the ion bombardment, an inert working gas like argon and a high voltage source is necessary. By applying a voltage, a glow-discharge plasma is ignited between the cathodic target and the anodic substrate. The deposition rate is relatively low and the coating thickness is not evenly distributed [7, 8]. In this work, a sputtering deposition

system has been used. Therefore, the various sputtering processes will be discussed in detail later.

The **ion plating process** is a hybrid process, i.e. either vaporization of the coating material takes place by thermal energy or momentum transfer in an anodic source or the coating material is directly supplied as vapour. Some of the vaporized atoms are ionized by a glow discharge produced by biasing the substrate to a high negative potential and employing a working gas. Therefore, the substrate and the coating underlie a constant bombardment of high-energy ions leading to better coating adhesion and modified microstructure within the coating. Deposition rates are high, but the coatings have an unevenly distributed coating thickness. The substrate temperature is below 300℃ and, therefore, relative ly low [6-8].
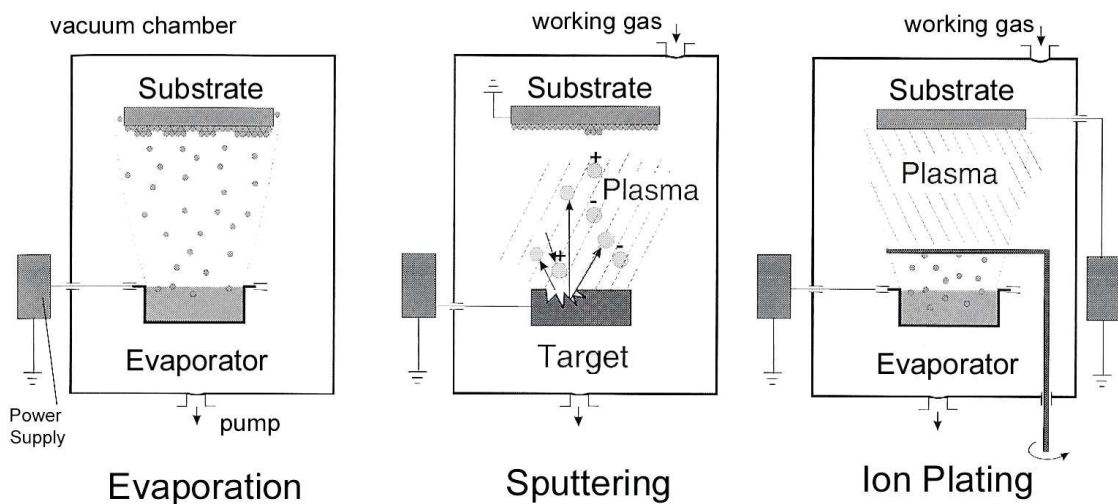
Fig. 2.1 Basic PVD processes [7].

2.1.2 Gas Discharge/Plasma

The ion plating as well as the sputtering process require a plasma environment which is also called the fourth state of matter. Plasma consists of permanently interacting neutrals, radicals, ions and free electrons. However, plasma is in a quasi-neutral state, because the number of positive and negative particles is the same. More precisely, it can be defined as a quasi-neutral gas of charged and neutral particles which show collective behaviour resulting from Coulomb interactions. The electric fields are generated by the movement of charged particles in the plasma, which induces local concentrations of positive and negative charge. The movement of charged particles also induces a current and therefore, magnetic fields. For this reason, the movement of charged particles which are far away is also influenced [7, 9].

There exist several types of plasmas: some which are in complete thermodynamic equilibrium, some which are in local thermodynamic equilibrium and some which are not in any local thermodynamic equilibrium. The latter is also called cold plasma, and is characterized by low pressures and relatively low temperatures. Cold plasmas are used in thin film technology and can be produced by applying a DC-voltage between two conductive electrodes to a gas, for example argon. Cold plasmas are furthermore produced by radio frequency (RF) or microwave (MW) power. The applied power generally influences the electrons whereas the ions stay almost unaffected due to their higher weight. The electrons are accelerated and gain energy. The nearly unaffected ions just transfer their energy by collision. Therefore, the electrons can reach temperatures up to 10000K, while the temperatures of the ions remain almost at room temperature. Due to the differing temperatures, cold plasmas are not in any thermodynamic equilibrium and temperature stays relatively low, because electron temperature only makes a small contribution to the overall temperature [9].

The process, where electrical charges are transported in a gas or vapour by mobile charge carriers (ions and electrons), is called gas discharge. As mentioned above, a gas discharge is generated by applying a voltage between two electrodes which lead to a small current created by free electrons. Due to naturally occurring radioactivity or cosmic radiation, these free electrons are always present. With increasing voltage, the energy of the electrons increases. If they gain enough energy, charge carriers are generated by inelastic collisions between neutral atoms and these accelerated electrons. This leads to ionisation of the atoms. The new ions are now also accelerated by the electric field and ionise other atoms. The ions are now accelerated towards the cathode, where they might produce secondary electrons after impact. Hence, the number of charge carriers is multiplied. The current increases while the voltage remains constant. Besides charge generation, recombination of positive and negative carriers takes place. The gas discharge process is self sustaining, if more charge carriers are generated than removed by recombination. Fig. 2.2 shows a typical I-V curve of a glow discharge with its fields of Townsend-, normal-, abnormal- and arc discharge. If the number of generated charge carriers is the same as the number of the removed ones, a steady state is reached, which is called Townsend-Discharge. Subsequently, the normal glow discharge region follows: the gas starts to glow, the voltage decreases and the current rises suddenly. The current is now proportional to the electrode area covered by the glow discharge. If the total electrode area is covered with the glow discharge, the abnormal glow discharge region is reached. It is used for most sputter deposition processes. Afterwards, the voltage decreases and the glow changes into an arc, which marks the beginning of the region of arc-discharge [6, 9, 10].

The motion of the electrons can not only be influenced by electric but also by magnetic fields, which exert a force on the moving charged particles. The ions stay nearly unaffected due to their higher weight. The electrons are accelerated proportional to their mass of charge, which leads to higher speed and impact energy. Therefore, the ionisation efficiency is better. Another advantage is the reduction of recombination, which lessens the electron loss [11].
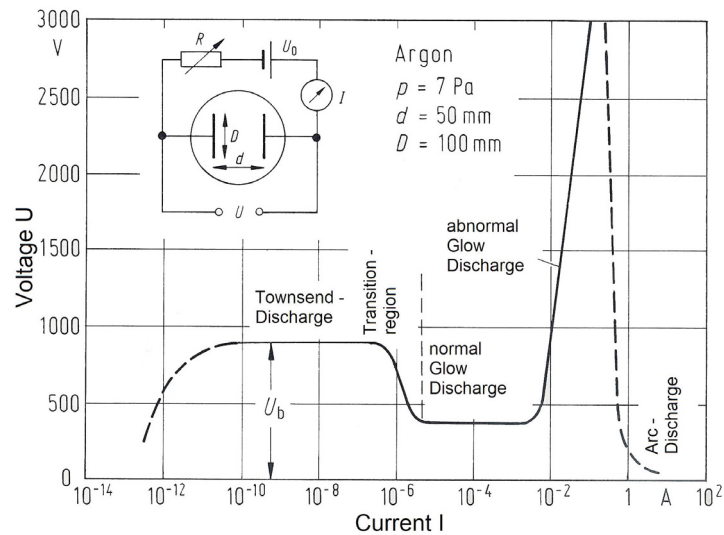
Fig. 2.2 Voltage-Current characteristics of a DC gas discharge process [6].

2.1.3   Reactive DC Magnetron Sputtering

As briefly mentioned in Chapter 2.1.1, sputtering is the direct ejection of atoms from the target surface due to ion bombardment, usually Ar^+ ions. The argon ions are provided by the argon working gas in a glow discharge. Before the gas discharge is ignited, the specimen chamber is evacuated to low pressures. A DC sputtering system consists of two electrodes facing each other in the deposition chamber. The cathode has two functions: it is the target material as well as the negative electrode which maintains the glow discharge by the production of secondary electrons. The substrates are placed on the anode [11].

The ejected atoms form the vapour phase and are afterwards transported to the substrate surface, where they condense [7, 8]. During their way to the substrate, collision with plasma particles is possible. Possible particle interactions during sputtering are shown in Fig. 2.3: ionisation by electron impact (Fig. 2.3.a), ion induced electron emission from the cathode (Fig. 2.3.b), electron induced emission of secondary electrons from the anode (Fig. 2.3.c), sputtering initiated by ion impact (Fig. 2.3.d) and charge transition processes (Fig. 2.3.e). Due to interaction with plasma particles, the sputtered atoms move with a defined angle and energy

distribution to the substrate in a disordered way. Hence, they condense on the substrate as well as on the chamber walls [6].

Fig. 2.3 Particle interactions which can occur during sputtering [6].

The sputtering yield is the number of atoms ejected per incident ion. Angle of incidence, mass ratio, surface energy, the condition of the target (roughness, crystalline structure, temperature) and the target material's sublimation heat have an effect on the sputtering yield [12].
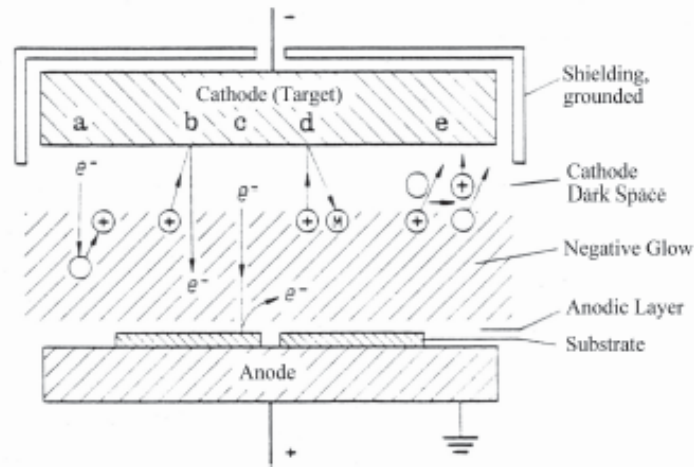
It is also common to apply a negative bias voltage on the anode or substrate. Due to the now additional ion bombardment of the anode or substrate, changes in the adsorption and nucleation process can occur, and e.g. a denser film can be deposited. If a too high negative bias voltage is applied, backsputtering effects can occur, which lead to a reduction in the deposition rate. For target surface cleaning and for gathering of possible left gas atoms in the chamber, sputtering with a shutter device between target and substrate preventing coating deposition is feasible [13].

In the magnetron sputtering process, a permanent magnetic structure is placed behind the target. The permanent magnetic structures are classified into circular, cylindrical or planar magnetrons [11]. The plasma is confined and concentrated to a so-called racetrack area close to the target due to trapping of the electrons by the induced magnetic field. Fig. 2.4 shows schematically a planar magnetron. The movement of the charged particles is affected by the interaction of the electrical and the magnetic field by the Lorentz-force. The electric field acts perpendicular, the magnetic field above the racetrack parallel to the target. The electrons move on a cycloidal path with a higher concentration of charged particles, leading to a higher ionisation efficiency. Therefore, the positive ion production rate is enhanced and the probability of electron loss by wall reactions is diminished. As a result, the deposition rate at lower working gas pressures increases and the deposition time decreases.

Moreover, the bombardment of the substrates by fast electrons and thus, excessive heating is avoided [10, 12].
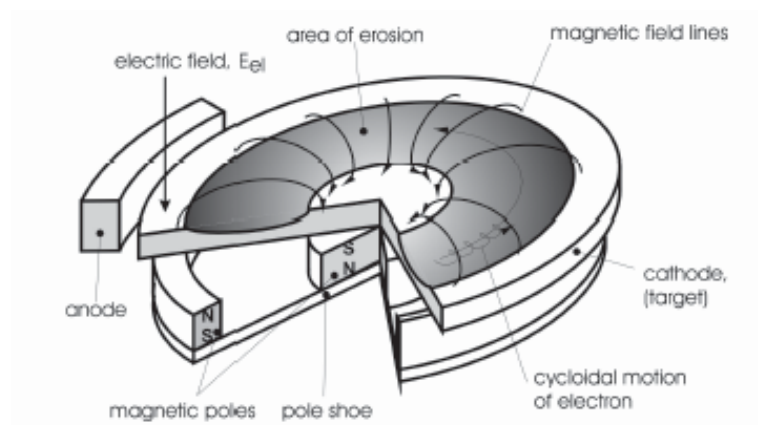
Fig. 2.4 Schematic of planar magnetron [11].

The different magnetron devices can be classified into two types: conventional balanced magnetrons (CBM) and unbalanced magnetrons (UBM). In conventional balanced magnetrons, all magnetic field lines loop ideally between the outer and inner magnet of the magnetron configuration, which means that they are balanced against each other. Therefore, the discharge is forced close to the target [4, 14]. In unbalanced magnetrons, either the inner or the outer magnetron is stronger. Therefore, some magnetic field lines do not loop and open towards the substrate, which lead to an expansion of the plasma away from the target (Fig. 2.5). The plasma density close to the substrate is now adjustable by varying the magnetic field. Due to a potential difference between the plasma and the substrate (for instance by applying a bias voltage to the substrate), ions are attracted to the substrate. As a result, the ion bombardment of the substrate is increased, whereas the energy of the impinging ions can be regulated [4, 15, 16].
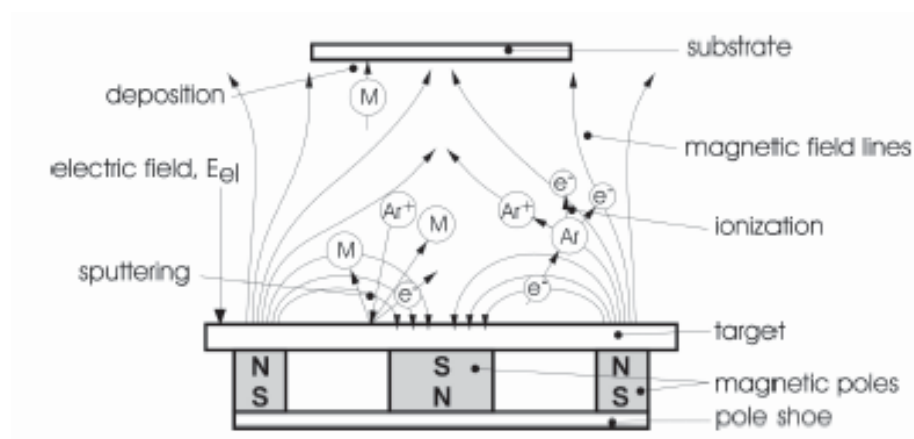
Fig. 2.5 Schematic of unbalanced magnetron configuration [17].

In the non-reactive sputtering process, the sputter deposition is carried out in an inert gas atmosphere (e.g. argon). Hence, the chemical composition of the sputtered film is nearly the same as the target composition. In the reactive magnetron sputtering process, one or more film components are supplementary inserted into the deposition chamber as gaseous species. The sputtered atoms interact with this reactive gas, such as N_2, CH_4 or O_2, which becomes part of the plasma and makes a contribution to the film formation process. The reaction between the sputtered atoms and the reactive gas takes place either at the target surface, in the gas phase or at the substrate surface. A so called poisoning of the target can occur, if the reaction takes place on the target surface. Sputtering rates are lowered due to higher lattice energy of the compound compared to the pure target material [18].

2.2 Nucleation and Growth

2.2.1 Nucleation and Growth

Properties of thin films are highly determined by their microstructure. In particular, in the case of coatings produced by condensation from the vapour phase, the properties are normally different to their bulk materials. The nucleation and growth processes, which occur during the deposition process, determine these properties and the final structure of the coating. Generally, the substrate and the deposited coating have different chemical compositions. Therefore, there is no instant condensation possible, if atoms from the vapour phase impinge on the substrate surface. In the following, two different interactions are possible: either the atom is reflected from the surface or adsorption on the surface occurs. Condensation takes place, if several adsorbed atoms combine and form small clusters, also called nuclei. The cluster formation itself is called nucleation. Growth is the following extension of the nuclei to form a coherent film. Nucleation and growth often occur at the same time during coating deposition. The sequence of the nucleation and growth process can be divided into the following steps [19-22]:

- Nucleation:
    - Formation of adsorbed monomers
    - Formation of subcritical embryos of various sizes
    - Formation of critically sized nuclei (nucleation step)
    - Growth of these nuclei to supercritical dimensions with the resulting depletion of monomers in the capture zone around them
    - Concurrent with the previous steps there will be nucleation of critical clusters in areas not depleted of monomers

- Clusters touch and coalescence to form a new island occupying an area smaller than the sum of the original two, thus exposing fresh substrate surface
- Monomers adsorb on the freshly exposed areas and 'secondary' nucleation occurs
- Large islands grow together, leaving channels or holes of exposed substrate
- The channels or holes fill via 'secondary' nucleation to give a continuous film

- Crystal growth: Coalescence of individual crystals on the substrate and grain boundary migration in the polycrystalline structure

As shown in Fig. 2.6, the impinging atoms arrive with a specific arrival rate on the substrate surface. As mentioned above, either the atoms are now reflected from the surface or become loosely bonded 'adatoms'. The adatoms, which transfer their kinetic energy to the lattice, may diffuse on the substrate surface for a while, before they either get desorbed again or become trapped at low-energy lattice sites. The adatom mobility is controlled by the kinetic energy of the adatom, the temperature of the substrate and the bonding strength between substrate and adatom. At very small arrival rates, the coverage is small which inhibits nucleation or film formation. Therefore, an equilibrium between adsorption and desorption is reached. High arrival rates lead to the formation of metastable and stable clusters. The clusters grow through adding of other arriving atoms from the substrate surface or directly from the vapour phase. Bulk diffusion of incorporated atoms to readjust their position is possible as well. Meeting clusters combine by growth or motion. This coalescence results in the formation of a more or less dense coating [6, 13, 23].
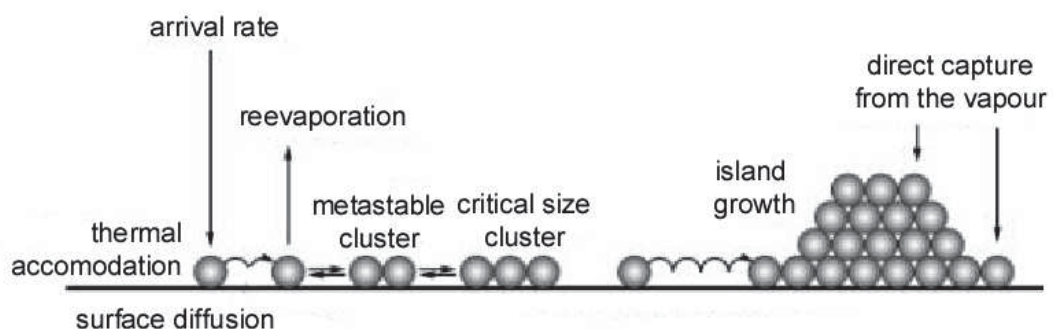
Fig. 2.6 Schematic representation of nucleation and growth processes [24].

The following Fig. 2.7 shows three possible modes of crystal growth on substrates in the early stages. In the first one, the Frank-van der Merwe mode (Fig. 2.7 (a)), the

film grows by the formation of layer by layer. Fig. 2.7 (c)) shows the Volmer-Weber mode. It is also called island mode, because small clusters nucleate immediately on the substrate surface and grow into islands. The Stranski-Krastanov mode is the intermediate case: at first there is a formation of monolayers, afterwards islands are formed (Fig. 2.7 (b)) [22, 25, 26].
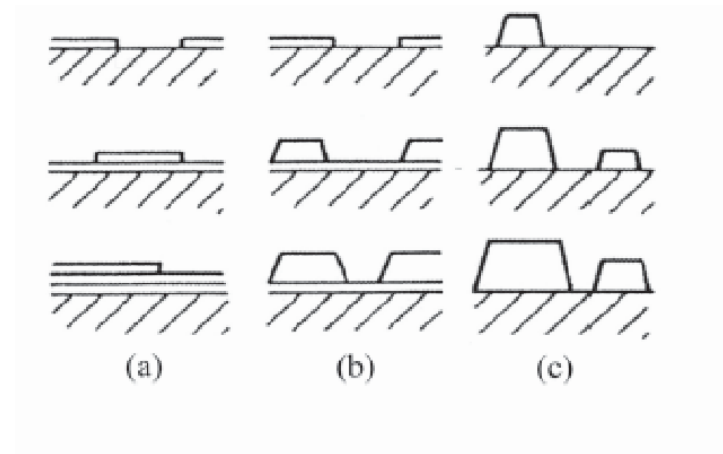
Fig. 2.7 The three different film growth mechanisms: (a) Frank-van der Merwe mode (b) Stranski-Krastanov and (c) Volmer-Weber [25].

The occurring crystal growth modes depend on the affinity of the film material to the substrate, the activation energy of diffusion and the binding energies between film-film and film-substrate [4, 22]. For example, when the atom-atom binding is stronger than the atom-substrate binding then island growth occurs. Frank-van der Merwe growth occurs when the atom-atom binding is equal or less strong than atom-substrate.

2.2.2 Morphology-Structure Zone Model

Structure zone models (SZM) were developed to show the correlation between coating structure and deposition parameters. In this way, morphology and microstructure of a film can be predicted as a function of adatom mobility independent on the material. Shadowing, desorption, surface diffusion, bulk diffusion and recrystallization are the basic processes in the atomic process of nucleation and growth of films. Shadowing is caused by the interaction of surface roughness and the angle of incidence of the arriving atoms. It prevents a constant coating for all areas of the surface [4, 27].

A quantification of these basic processes is possible by the characteristic surface roughness, the activation energy of surface and bulk diffusion, and the sublimation energy. There is a correlation between these energies and the melting point T_m for many pure metals. The basis of structure zone models is that several of these basic processes can be expected to dominate a certain field of homologous temperature (T/T_m) ranges. T is the substrate temperature, T_m the melting temperature [6, 27].

The first structure zone model was defined by Mochvan and Demchishin (1969). They defined three different structural zones with distinct properties and structures, and studied the influence of substrate temperature on condensation, structure and properties [28]. Thornton (1977) took the influence of the sputtering gas pressure (argon) into account. As shown in Fig. 2.8 (a), he also introduced a transition zone T between zone I and zone II. Due to the increasing number of collisions between particles with rising gas pressure, the kinetic energy of the impinging adatoms decreases. Messier et al. modified the Thornton model (see Fig. 2.8 (b)) by taking the influence of the energy of the impinging ions into account. The ion bombardment induces mobility of the surface atoms, which lead to a broadening of zone T in the lower temperature range.
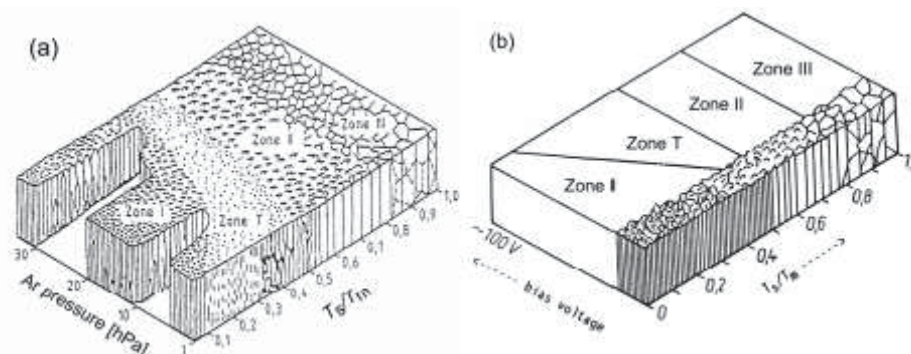

Fig. 2.8 (a) Structure zone model after Thornton [31] and (b) after Messier et al. [29].

In general, higher gas pressure or lower bias voltages cause a reduction of the kinetic energy, which lower the adatom mobility. Therefore, higher deposition temperatures are necessary to determine a certain coating structure.

Zone I consists of structures, which form by low T/T_m ratio. Due to low adatom mobility, shadowing effects occur, which lead to the formation of tapered, porous crystals separated by voids. The density of lattice imperfections is high.

Zone T is the transition zone from Zone I to Zone II. Due to the higher homologous temperature ratio, the adatom mobility is higher, which leads to a dense array of poorly defined fibrous grains without voided boundaries.

In Zone II, the adatom diffusion controls the growth of the crystals, which consist of columnar grains with distinct, dense grain boundaries. With increasing T/T_m, the crystal diameter increases.

Zone III: bulk diffusion is the dominating process. The columnar grains are equiaxed (recrystallized grain structure) [6, 29-30].

Fig. 2.9 shows various conditions which lead to the different structure zone models of vapour deposited coatings. Important steps for the further growth of the film are the same as for the first nuclei: condensation, surface diffusion and desorption. Bulk diffusion plays a role at higher temperatures.

In the case of zero surface diffusion, a slightly varying direction of impinging atoms and a unity condensation coefficient (Fig. 2.9 (a)), and spherical initial nuclei, a dense columnar coating structure with a relatively smooth surface topography is formed. The developed structure corresponds to Zone T. Fig. 2.9 (b) illustrates the case if the initial nuclei have different orientations and therefore, different surface energies and condensation coefficients. Due to the preferred growth of crystal planes with high condensation, the coating structure is open and relatively rough (corresponds to Zone I). Fig. 2.9 (c) shows a dense columnar structure with a smooth but facetted surface. Due to higher substrate temperatures, differences in the condensation coefficient are easily balanced. This leads to the same growth rate for all crystal planes (Zone II). When repeated nucleation on the surface of the growing crystals occurs, a structure as shown in Fig. 2.9 (d) is formed.
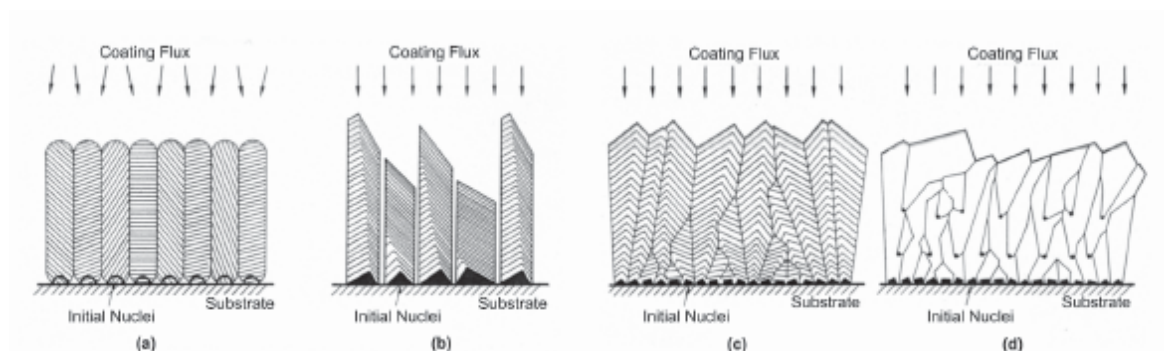
Fig. 2.9 Structure development for several cases of adatom surface diffusion: (a) zero surface diffusion, equal condensation coefficient, (b) zero surface diffusion, condensation coefficient depends on crystallographic surface, (c) infinite surface diffusion and (d) infinite surface diffusion with periodic nucleation [27].

2.3 Tribology

2.3.1 General

Tribology, the term is derived from the Greek word 'tribos' meaning rubbing, is a field of science often defined as *the science and technology of interacting surfaces in relative motion and all practices related thereto* [32]. It is a broad, interdisciplinary field which involves friction, wear and lubrication.

Industrialized societies have always made an attempt to reduce or control friction and wear by design changes, choosing improved bulk material or by applying lubrication techniques [33, 34]. The reason is that malfunctioning tribological systems cause considerable economic losses.

The most important aspect to be considered when dealing with tribology is, that tribological properties are not material but system properties. The tribological system, also called tribosystem, is a physical volume which includes all relevant elements in the tribological contact of interest. The elements of the tribosystem include the contacting materials, the geometry of the contacting bodies, surface topography, contact configuration, nature of the relative motion, nature of the loading, lubrication and environment.

A tribosystem might be seen as a black box which transforms inputs into outputs (see Fig. 2.10). Material input parameters are the material composition and the chemical and physical properties of the counterparts. Environmental parameters are, for example, temperature, lubrication or humidity. Other input parameters are the geometry, the normal force (F) and the velocity (u). The change of a single parameter can lead to a complete change in the response of the tribosystem.
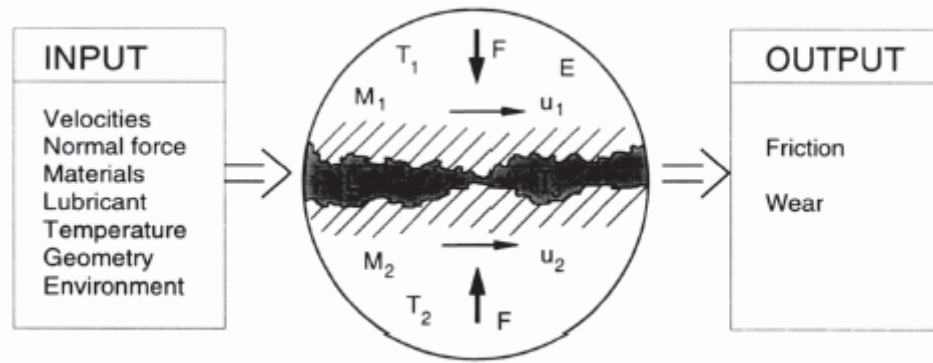
Fig. 2.10 Parameters which influence the dynamic tribophysical and –chemical contact processes which control friction and wear [33].

2.3.2 Friction

Friction is the tangential resistance to motion which is experienced when one body moves relative to another [33]. The coefficient of friction (µ) is the ratio between the frictional force (F), which acts tangentially to the interface, and the normal load (F_N) [33].

$$\mu = \frac{F}{F_N} \tag{2.1}$$

As shown in Fig. 2.11, three components might be identified in sliding friction. The original concept was developed by Bowden & Tabor (1950). They explained the mechanism of friction in sliding contact between two materials by the adhesional effects between surface asperities due to attractive forces (see Fig 2.11 (a)). The regions, where these interactions occur, are called junctions. The sum of all junctions is the real area of contact. The adhesional component of friction originates from the force which is necessary to shear the microwelded junctions and break them, when one of the materials is moved in tangential direction. Bowden & Tabor also considered the ploughing effect in their concept. As shown in Fig. 2.11 (b), a resistance to motion is induced, when a hard asperity or a hard particle is forced into a softer material and ploughs out a groove by plastic flow in the softer material. Ploughing can also appear if wear particles are entrapped between the two materials. However, friction force and the number of wear particles are increased, which increases subsequent friction and wear [32, 33]. Bowden & Tabor believed, however, that adhesion was the main reason for friction. Since this concept has been criticized for several reasons, like not involving the surface roughness effect of friction and a bad agreement between the theoretically calculated and the experimentally achieved values, new models were developed.
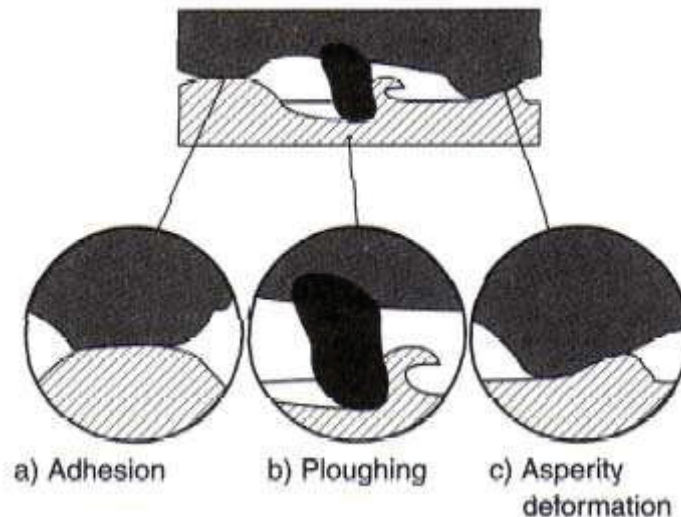
Fig. 2.11 The three components of sliding friction: (a) adhesion, (b) ploughing and (c) asperity deformation [33].

For example, Green (1955) developed a theory, which takes the influence of plastic deformation of the asperities into account. This theory was extended by Edwards and Halling (1968). It demonstrates that resistance to motion originates from the work done when asperities are plastically deformed as they slide over each other (see Fig. 2.11 (c)) [33, 34].

Rabinowicz (1965) postulated another theory in which the surface energy of adhesion as well as the roughness angle of the surface and the radius of the junctions are regarded.

Suh and Sin (1981) developed a new concept called 'genesis of friction' [35]. In this theory, the frictional force, and therefore the friction coefficient μ, is influenced by the time-dependant contributions of the three components of sliding friction shown in Fig. 2.11: adhesion (Fig. 2.11 (a)), ploughing (Fig. 2.11 (b)) and asperity deformation (Fig. 2.11 (c)). As shown in Fig. 2.12, Suh and Sin identified several stages of different frictional mechanisms a unlubricated sliding contact goes trough in the running-in period until steady-state friction is reached. In the first stage (1), ploughing of the surface by asperities is the dominating mechanism. Adhesion does not contribute much due to surface contamination, which prevents sticking. In the first stage, the coefficient of friction is widely independent of material combination, the surface conditions and the environmental conditions. After the surface contamination is removed by ploughing, the adhesion increases and, therefore, the coefficient of friction increases slightly (stage 2). During stage 3, the coefficient of friction is rising due to the large increasing number of entrapped wear particles which cause further ploughing of the surface. The subsequent formation of more abrasive particles results in a larger contribution of adhesion and surface deformation to the friction coefficient. Finally, the coefficient of friction reaches a maximum. In stage 4, the

coefficient of friction remains constant as a consequence of a constant number of wear particles entrapped in the contact zone. The number of entrapped particles is the same as the number of particles, which leave the interface. Stage 4 describes the steady-state friction in case of two equal materials sliding against each other. If two different materials are rubbed together (e.g. a hard stationary slider is slid against a soft specimen), the asperities of the hard surface are worn away, which leads to a polished surface. Asperity deformation and ploughing diminish because wear particles cannot stay in the contact area. As a result, the friction coefficient decreases (stage 5). In stage 6, the coefficient of friction reaches a steady-state value because the softer counterpart gets the same polished surface.

The shown stages of the friction coefficient are valid for a steel contact and they can differ for other material combinations [33, 35, 36].

Fig. 2.12 Stages of friction mechanisms vs. sliding distance in sliding steel contacts [35].

Friction is a particularly complex interaction between the surfaces of two materials. Until now, there is no theoretical model which can predict the friction coefficient of two materials in sliding contact.

2.3.3 Wear

Wear may be defined as the material removal or surface damage that results from the relative motion between contacting solid surfaces. Wear occurs at the same time as friction because they are the result of the same tribological contact processes. It is necessary to quantify and compare wear effects; for this purpose, the dimensional wear coefficient K [mm³/Nm] might be used. It shows the relationship between the worn volume V, the normal load F_N and the sliding distance s [33]:

$$K = \frac{V}{F_N \cdot s}$$ (2.2)

There are different mechanisms which lead to material removal from the surface. Wear might be classified in adhesive wear, abrasive wear, surface fatigue and tribochemical wear (see Fig. 2.13). In a real contact, typically more than one wear mechanism acts at the same time.

Asperity junctions are formed between two surfaces of solid materials which are sliding against each other (Fig. 2.13 (a)). Due to relative tangential movement of the surfaces, shearing of the junctions occurs, which causes the fracture of the junction in the original interface. However, the fracture occurs sometimes in the weaker material, if the force required to break through the bulk material is smaller than to break trough the interface. This leads to a removal of material or a transfer of fragments to the opposing contact surface. Material removal which follows the mechanism explained above is called adhesive wear [32-34].

Abrasive wear is the displacement of material caused by hard particles or protuberances [37]. Asperities of a hard surface or hard particles slide on the surface of a softer material and the asperities are pressed into the softer surface, and plough or cut the softer counterface (see Fig. 2.13 (b)). Abrasion might be classified as two-body and three-body abrasion: If fixed particles or hard asperities plough the counter surface, the wear mechanism is called two-body abrasion. In case of three-body abrasion, the abrasive material is loose between the two surfaces. In three-body abrasion, wear is about one or two orders of magnitude lower than in two-body abrasion. The possible mechanisms of abrasive wear are microploughing, microcutting, microfatigue and microcracking [33, 34].

Surface fatigue occurs during repeated rolling and sliding at a stress level in the material which can bear it once but not if repeated many times. The formation of surface or subsurface cracks might be induced. These cracks grow and after a critical number of cycles a break-up of the surface occurs. This results in delamination of large fragments which can act as abrasive particles as well (see Fig. 2.13 (c)) [33, 34].

In chemical wear, the determining factors are the detrimental chemical reactions of the sliding materials. These reactions are activated by the influence of the environment and the mechanical contact, as shown in Fig. 2.13 (d). Elevated temperatures at the surface caused by rubbing have a supportive effect for tribochemical reactions. It results in removal of material and wear debris formation. The most common wear process is oxidational wear. The oxide layer, which normally protects the material from further oxidation in the absence of motion, is continuously rubbed away during relative motion.
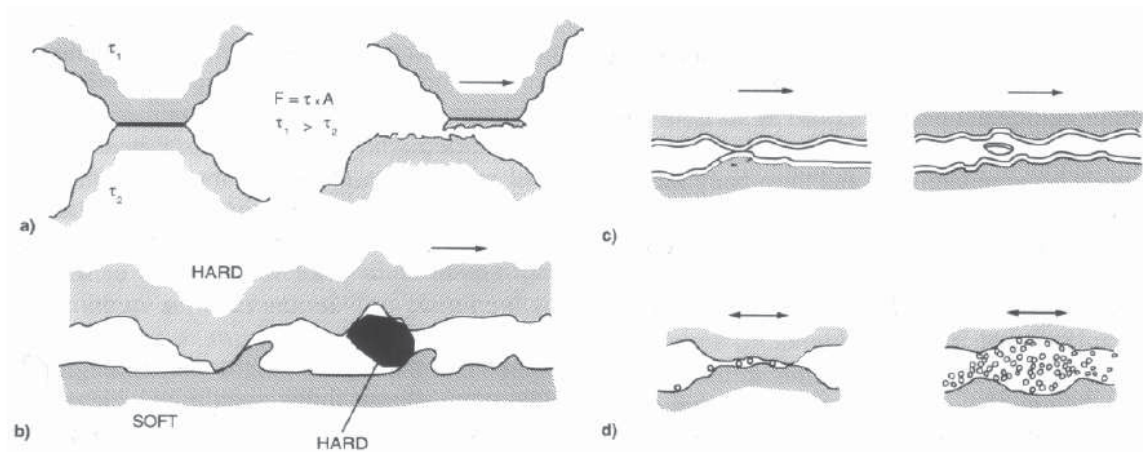
Fig. 2.13 The four basic wear mechanisms: (a) adhesion, (b) abrasion, (c) fatigue and (d) chemical reaction [33].

Like friction, wear is not a material but a system property. So far, the occurring wear between any material combinations under given sliding conditions cannot be predicted by theoretical models.

2.3.4 Coatings Tribology

A newer approach to friction and wear control is the use of surface treatments and coatings, which resulted in a new discipline called surface engineering. Tribological coatings are defined as coatings, which are sufficiently thin that the substrate material has a part in determining the friction and wear behaviour. The coated surface must often have an appropriate combination of properties like elasticity, shear strength, fracture toughness, hardness and adhesion. As shown in Fig. 2.14, there might be four different zones with different relevant tribological properties which must be regarded. Most of these required properties cannot easily be achieved at the same time. Therefore, the final coating has always to be a compromise between them [32, 33].

Coatings have now a wide appliance in controlling friction and wear, whereas it is possible to reduce the coefficient of friction up to two orders of magnitude in the most successful solutions. Also wear can be reduced by several orders of magnitude.

Friction and wear mechanisms of coatings are dependent on lots of parameters regarding coating, interface and substrate. Important parameters are the stress and strain distribution in the whole contact area, the following elastic and plastic deformations and the total wear particle formation process and its dynamics.

For the analysis of the tribological phenomena in a coated contact area, it is important to take macromechanical and micromechanical as well as tribochemical changes into account. Macromechanical tribological mechanisms are associated to the whole contact area and they describe the friction and wear phenomena in

consideration of the coating to substrate hardness relationship, the surface roughness, the thickness of the coating and the size and hardness of the debris in contact. These parameters have a huge influence on the tribological response. Micromechanical mechanisms affect the stress and strain distribution at an asperity level, material liberation, crack generation and single particle formation in micrometer to nanometer dimension. Tribochemical mechanisms at the contact interface result in the formation of stable compounds or layers like oxides after some time of rubbing, which control the subsequent friction and wear behaviour. Elevated temperatures may enhance the compound formation and change the different acting mechanism [33].
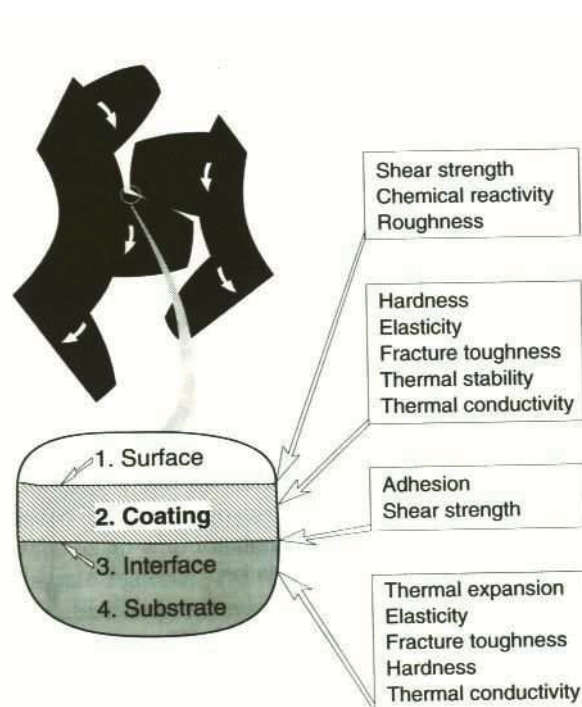
Fig. 2.14 Important tribological properties in different zones [33].

The friction and the wear mechanisms will be discussed in the following according to a number of different tribological contact conditions resulting from the relationship between the four main parameters mentioned above [33].

The hardness of the coating and its relationship to the substrate hardness influences the tribological behaviour of a coated surface to a great extent. There are two cases possible: The first is the deposition of a soft coating on a harder substrate. In this case, the contact area as well as the interfacial shear strength are reduced which leads to a reduction of the friction coefficient. In general, it is advantageous that the substrate material is as hard as possible. It avoids fracture of brittle coatings by deformation as well as it improves the load support and decreases the area of contact. The deposition of a hard coating on a relatively soft substrate reduces wear.

The friction coefficient of hard coatings decreases too, if an easy shearable microfilm, for example an oxide layer, is formed on the top of the coating. The hard coating now replaces the role of the hard substrate. Therefore, the load is well supported by the hard coating and the shearing will take place in the microfilm.

Fig. 2.15 shows twelve contact conditions which influence friction, when a hard spherical slider moves on a relatively hard or soft coated flat surface. Fig. 2.16 shows the same schematic representation for wear mechanisms as used for the friction mechanisms in Fig. 2.15. Eight typical wear mechanisms can be defined.

First we consider the case of soft coatings deposited on hard substrates. If the film is thin enough (Fig. 2.15b), the friction force might be calculated as the product of the shear strength of the film and the contact area. A low friction coefficient is achieved, if the film has low shear strength and the substrate has high hardness or a high elastic modulus, which reduces the contact area [33, 38]. Furthermore, the plastic deformation and thus, the ploughing effect and the adhesion are small. However, constant sliding can lead to adhesive and fatigue wear (Fig. 2.16b).

As shown in Fig. 2.15a and 2.16a, in case of a soft thick film, the coefficient of friction increases with increasing coating thickness due to the lower load-carrying capacity of the surface and induced plastic deformation (ploughing). Moreover, high adhesive wear appears because an enlargement of the contact area [33].

If the surface roughness is smaller than the coating thickness and the coating is sufficiently stiff to carry the load, there is nearly no influence on friction. On the opposite side, if the surface roughness is larger than the coating thickness, scratching for thick coatings (Fig. 2.15e and 2.16c) and penetration for thin coatings (Fig. 2.15f) occur. Thus, friction and wear increase [33, 39].

If small hard particles (with a diameter smaller than the coating thickness) are in the contact area, there is no fundamental effect on the friction behaviour due to embedding of these particles in the soft coating (Fig. 2.15i). In case of hard particles which have the same or larger size as the coating thickness and the surface roughness, the friction increases. The particles are caught by the surface roughness and scratch or plough the surface resulting in high wear (Fig. 2.15j and Fig. 2.16d) [33].

Now we consider the situation of a hard coating deposited on a soft substrate. As mentioned above, hard coatings show good wear protection. They protect the substrate against ploughing due to their higher hardness. However, due to their higher shear strength, they normally have a high coefficient of friction.

In the case of a thin coating, the coating cannot support the load and therefore, deformation of the softer substrate occurs. This results in an increased ploughing and thus, the friction increases (see Fig. 2.15d). Therefore, the substrate should be as hard as possible. Moreover, the formation of fatigue cracks in the coating and at the

substrate surface is possible, resulting from stresses in the coating and interface (Fig. 2.16e).

As shown in Fig. 2.15c, a thicker coating is able to carry part of the load which leads to smaller deformation of the substrate and less deflection of the coating. Therefore, the frictional behaviour is better.

Surface roughness causes a reduction of the contact area and thus, reduces the adhesion. Sliding occurs only on the asperities and the coefficient of friction decreases (Fig. 2.15g,h). If both surfaces have a high roughness, the coefficient of friction may increase due to interlocking and breaking of the asperities. Wear increases during sliding, if hard and sharp wear debris is formed due to coating failure (Fig. 2.16f). If the soft substrate is plastically deformed, the number of asperity contacts increases. This causes a higher contact area, and therefore, the friction coefficient increases. Delamination of flake-like wear debris can occur if the adhesion between the substrate and the coating is not strong enough (Fig. 2.16g) [33, 40].

Small particles introduced in the sliding contact can be hidden in the valleys formed by the asperities. Therefore, they have no influence on the friction coefficient as shown in Fig. 2.15k. Large particles which are softer than the surface will be crushed and destroyed under the applied load in the contact area. This results in a higher coefficient of friction (see Fig. 2.15l). Particles with a higher hardness than the surface will plough and scratch the surface leading to a high wear rate (Fig. 2.16h). [33].
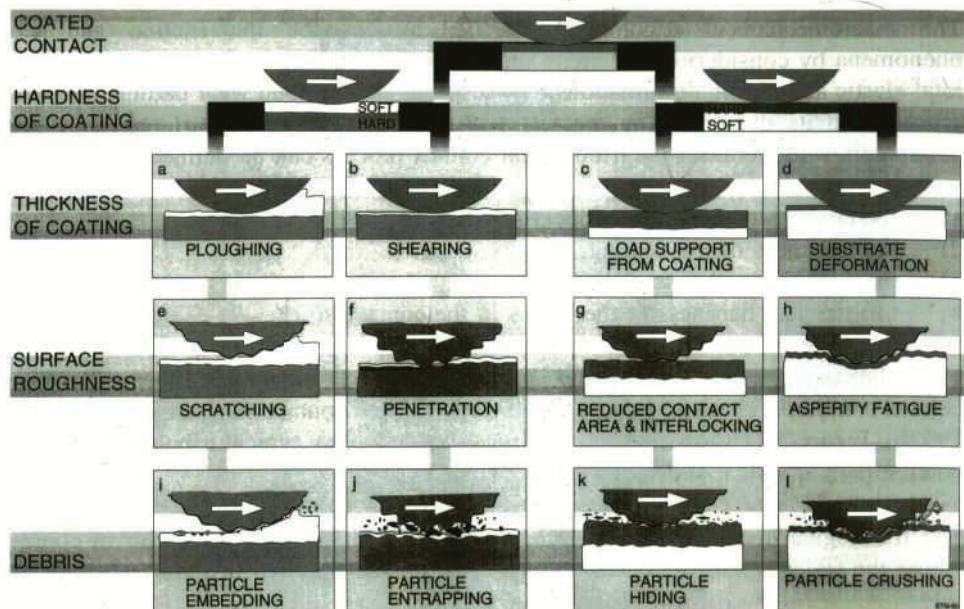

Fig. 2.15 Contact conditions for different mechanisms which influence friction [33].
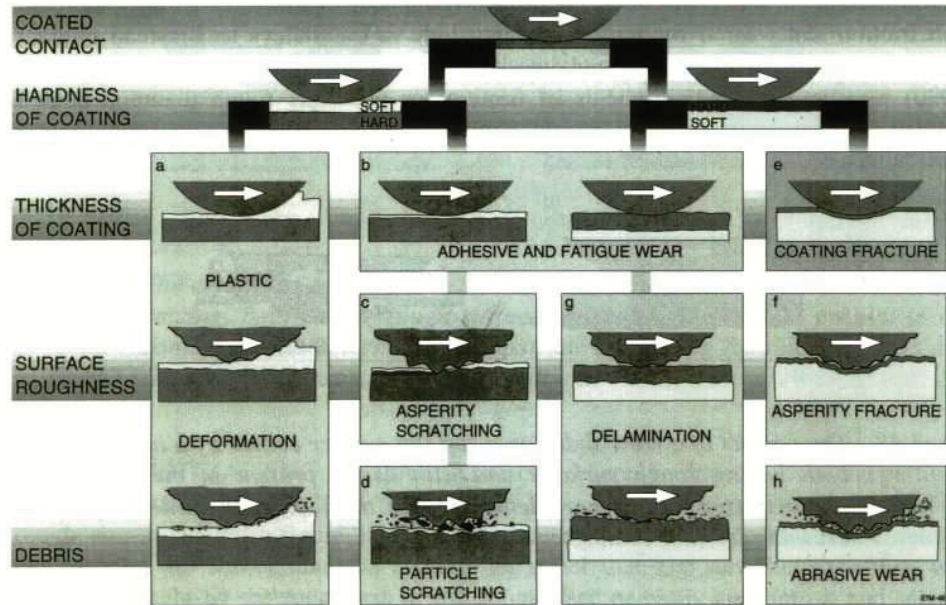
Fig. 2.16 Contact conditions for different mechanisms which influence wear [33].

3 Experimental

3.1 Coating deposition

3.1.1 Coating facility

The coatings investigated in this work have been deposited with a laboratory-scale DC/pulsed DC sputtering system with an Aja magnetron cluster (3 magnetrons with 2" diameter) with nitrogen as reactive and argon as working gas (Fig. 3.1). A schematic arrangement can also be seen in Fig. 3.1.
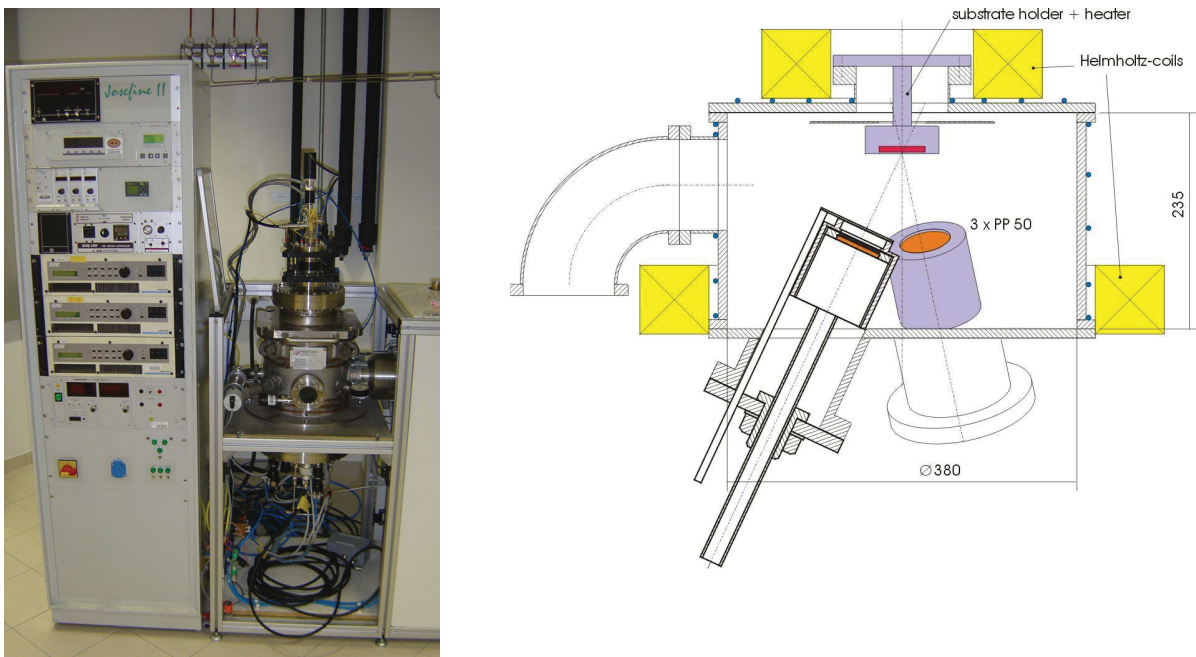
Fig 3.1 The DC/pulsed DC sputtering system and a schematic arrangement of the deposition plant [41].

The cylindrical vacuum chamber has a size of $\varnothing$ 380 mm x 235 mm. The magnetron power supplies for the different targets are two bipolar pulsed DC generators (ENI RPG-50, programmable frequency 50-250 kHz, duty cycle from 2.5 to 40%), of which one supplies two targets simultaneously. The ENI generators can be applied in dc and pulsed dc mode. To apply a negative voltage to the substrates for sputter cleaning prior to deposition and for supplying the bias voltage during the deposition, another pulsed DC generator (ENI RPG-50) is used. The pumping system consists of a dual stage rotary vane pump (Pfeiffer Vacuum Duo 20, pumping speed 24 m³/h N_2) and a turbomolecular pump (Pfeiffer Vacuum TMH 521 P, pumping speed 300 l/s N_2).

The lower part of the chamber contains 3 water-cooled targets ($\varnothing$ 50.4 mm) with shutters which can be rotated sideways. The upper part contains the heated substrate holder which can be heated up to 700℃. Substrates with a size up to $\varnothing$ 50 mm can be mounted on the substrate holder and substrate ion energies up to 300 eV can be reached.

3.1.2 Deposition procedure

The deposition procedure includes following steps:

- Ultrasonic cleaning of the substrates in acetone for five minutes followed by the same cleaning process in ethanol. Afterwards the substrates are air-dried.
- Mounting the substrates in the sample holder onto the substrate plate assembly in the deposition chamber.
- Starting the pumping system and the evacuation process. After reaching a pressure of 2×10^{-3} Pa, the chamber is heated up to 350℃.
- After the heating process is finished and a pressure of 2×10^{-3} Pa is reached again, ion etching of the substrates is carried out. In a pure argon atmosphere (pressure ~0.4-0.5 Pa, ~50 sccm), a plasma is ignited between the substrates and the chamber wall. The etching voltage and the etching frequency are set to -500 V and 250 kHz with a resulting etching current of approximately 0.6 A. The duration of the etching process is varied between 5 and 30 minutes depending on the type of substrate.
- Subsequently, the deposition parameters are adjusted depending on the different systems (see chapter 3.1.4), the shutters are removed and the deposition process is started. Additionally, the substrates are biased with a bias voltage of -80 V and a resulting bias current of 0.01 A. The reactive gas flow rate (N_2) and the work gas flow rate (Ar) are set to 20 sccm and 25 sccm during the deposition process. The total pressure is kept constant at 0.4 Pa. After a deposition time of 55 up to 90 minutes, an average coating thickness of 3 µm is reached.
- Cooling down, stopping the pumping system after reaching a temperature below 100℃, venting the chamber and dismounting the substrates.

During the deposition process, the deposition parameters are continuously controlled and, if necessary, readjusted. A summary of the constant process parameters can be seen in Table 3.1.

Table 3.1 Summary of the process parameters and the various steps.

Evacuation, Heating – 90 min			
Ion Etching			
Voltage U_M [V]	**Pulse [kHz]**	**Time [min]**	**Temperature**
-500	250	Silicon wafer: 5 HSS:15-30	350℃
Deposition			
BIAS voltage U [V]	**f(Ar) sccm**	**f(N_2) sccm**	**Time [min]**	**Temperature**
-80	25	20	55-90	350℃

3.1.3 Targets and Substrates

The different targets used in the deposition process are listed in Table 3.2.

Table 3.2 Targets used.

Target composition	**Dimension [mm]**	**Purity [%]**	**Manufacturer**
Chromium	$\varnothing$ 50.4 $\times$ 6	99.9	GfE
Aluminium	$\varnothing$ 50.4 $\times$ 6	99.5	GfE
CrAl25	$\varnothing$ 50.4 $\times$ 6	99.5	Plansee
Silver	$\varnothing$ 50.4 $\times$ 6	97	ÖGUSSA
Niobium	$\varnothing$ 50.4 $\times$ 6	99.9	GfE
Rhenium	$\varnothing$ 50.4 $\times$ 2	99.95	Osnabruegge

Two types of substrates have been used:
- Single crystal silicon (100) samples of size 20 x 7 x 0.35 mm^3 which are used for coating thickness evaluation, structure analyses, biaxial stress temperature measurements and composition analyses.
- Böhler S600 (HS 6 5 2, AISI 611) high speed steel discs of the size $\varnothing$ 30 x 10 mm which are used for tribological testing, evaluation of micro hardness and Young's Modulus, adherence evaluation and determination of surface morphology.

3.1.4 Coating Deposition Parameters

3.1.4.1 Preliminary Tests

In order to obtain the stoichiometric CrN, several different coatings were deposited on silicon substrates by varying the gas flow rate of Ar and N_2 (see Table 3.3.). These coatings were deposited on silicon samples of the size 20 x 7 x 0.5 mm³ instead of 20 x 7 x 0.35 mm³. A current of 0.35 A was kept constant at each Cr target. The coatings were then characterized by X-ray diffraction (XRD) as summarized in Fig. 4.1.

Table 3.3 Deposition parameters for the CrN coatings on silicon.

| Coating	Number of targets	I_{Cr} [A]	f(Ar) [sccm]	f(N_2) [sccm]	pN_2/ (pN_2+pAr) [%]	P_{tot} [Pa]	Substrate	Time [min]
CrN N°1	2xCr	0.35	25	20	40	0.4	Si	60
CrN N°2	2xCr	0.35	25	10	26	0.32	Si	60
CrN N°3	2xCr	0.35	25	15	34	0.36	Si	60

A pN_2/(pN_2+pAr) ratio of 40% at p_{tot}=0.4 Pa was defined as optimum parameter for the deposition of stoichiometric CrN based on the XRD results (cf. Fig. 4.1). The same parameters were further used for the deposition of CrAlN and CrAlXN coatings (X stays for Ag, Nb or Re). As will be shown later (see chapter 4.1), a N_2 partial pressure of 26% results in the formation of Cr_2N. At a pN_2 /p_{tot} of 34%, there is still some Cr_2N phase present.

For the deposition of CrN on high speed steel, the same deposition parameters were used as for the coating CrN N°1 listed in Table 3.3, only substrate and etching time (15 min) were varied.

In a second step, an Al target and a two Cr targets were used to deposit CrAlN coatings. The goal of these preliminary tests was to investigate the dependence of the coating chemical composition as function of the magnetron current of the Al target. For this purpose, the magnetron currents were kept constant at 0.35 A at each Cr-target (see Table 3.4) and the Al magnetron current was varied between 0 and 0.62 A. In this way, the Al content in the CrAlN coating could be varied between 0 and 12 at.% (see Fig 3.2). It was not possible to use higher currents due to the possibility of melting of the Al target.

Table 3.4 Deposition parameters for the CrAlN coatings.

Coating	Number of targets	I_{Cr} [A]	I_{Al} [A]	f(Ar) [sccm]	f(N$_2$) [sccm]	P_{tot} [Pa]	Substrate	Time [min]
CrAlN N°1	2x Cr, 1x Al	0.35	0.175	25	20	0.4	Si	120
CrAlN N°2	2x Cr, 1x Al	0.35	0.09	25	20	0.4	Si	60
CrAlN N°3	2x Cr, 1x Al	0.35	0.05	25	20	0.4	Si	60
CrAlN N°4	2x Cr, 1x Al	0.35	0.26	25	20	0.4	Si/HSS	60
CrAlN N°5	2x Cr, 1x Al	0.35	0.54	25	20	0.4	Si	60
CrAlN N°6	2x Cr, 1x Al	0.35	0.62	25	20	0.4	Si/HSS	60
CrAlN N°7	2x Cr, 1x Al	0.35	0.42	25	20	0.4	Si	60
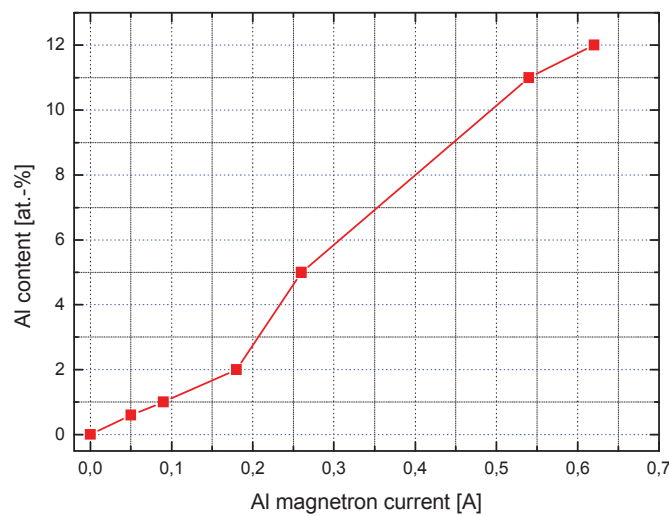
Fig. 3.2 Variation of the Al content as a function of Al magnetron current.

Tribological tests of $Cr_{1-x}Al_xN$ coatings at elevated temperatures indicated that higher Al-contents are beneficial for their wear resistance. For manufacturing CrAl targets using powder metallurgy, a minimum content of 25% Al is necessary. For these two reasons, CrAl25 targets were used to deposit CrAlN coatings with a content >12 at.%. By using two CrAl25 targets instead of separate Cr and Al targets, a chemical composition of the coating of $Cr_{74}Al_{26}N$ could be reached. The deposition parameters are summarized in Table 3.5. Coating N° 8 was deposited at 350℃, whereas coating N°9 was deposited at 500℃.

Table 3.5 Deposition parameters for the CrAlN coatings deposited with two CrAl25 targets.

Coating	Number of targets	I_{CrAl} [A]	f(Ar) [sccm]	f(N_2) [sccm]	Temperature [°C]	Substrate	Time [min]
CrAlN N°8	2x CrAl25	0.35	25	20	350	Si/HSS	90
CrAlN N°9	2x CrAl25	0.35	25	20	500	HSS	90

After the $Cr_{74}Al_{26}N$ coating was tribologically tested at elevated temperatures, and the results showed the best wear behaviour of all $Cr_{1-x}Al_xN$-coatings, additional coatings of the form $Cr_{1-x}Al_xZ_yN$ were deposited, were Z is Ag, Nb or Re. For these coatings, the deposition parameters concerning reactive and working gas, magnetron current for the CrAl25 targets, bias voltage and p_{tot} were kept constant, namely, the same values as listed for the CrAlN N°8 in Table 3.5 were used.

3.1.4.2 CrAlN-Ag

Table 3.6 lists the parameters of the different coatings deposited in the system CrAlN-Ag. The Ag magnetron current was varied between 0.02 and 0.06 A to obtain different chemical compositions of the coatings. The bias voltage was set to -80 V and the deposition temperature was 350°C for all co atings. To reach a coating thickness of approximately 3 µm, the deposition time was set to 90 minutes.

Table 3.6 Deposition parameters for the CrAlN coatings with Ag.

Coating	Number of targets	I_{Cr} [A]	I_{Ag} [A]	P_{tot} [Pa]	Substrate	Time [min]
Ag N°1	2x CrAl25, 1x Ag	0.35	0.02	0.4	Si/HSS	90
Ag N°2	2x CrAl25, 1x Ag	0.35	0.04	0.4	HSS	90
Ag N°3	2x CrAl25, 1x Ag	0.35	0.06	0.4	Si/HSS	90

3.1.4.3 CrAlN-Nb

Table 3.7 lists the different coatings deposited in the system CrAlN-Nb. The Nb magnetron current was varied between 0.35 and 1 A to obtain different chemical compositions of the coatings. The bias voltage was set to - 80 V and the deposition temperature was 350°C for all coatings. To reach a coating thickness of approximately 3 µm, the deposition time was varied between 55-90 minutes.

Table 3.7 Deposition parameters for the CrAlN coatings with Nb.

Coating	Number of targets	I_{Cr} [A]	I_{Nb} [A]	P_{tot} [Pa]	Substrate	Time [min]
Nb N°1	2x CrAl25, 1x Nb	0.35	0.35	0.4	Si/HSS	90
Nb N°2	2x CrAl25, 1x Nb	0.35	0.7	0.4	Si	90
Nb N°3	2x CrAl25, 1x Nb	0.35	1	0.4	Si	90
Nb N°4	2x CrAl25, 1x Nb	0.35	0.7	0.4	HSS	60
Nb N°5	2x CrAl25, 1x Nb	0.35	1	0.4	HSS	55

3.1.4.4 CrAlN-Re

Table 3.8 lists the different coatings deposited in the system CrAlN-Re. The Re magnetron current was varied between 0.02 and 0.1 A to obtain different chemical compositions of the coatings. The bias voltage was set to -80 V and the deposition temperature was 350°C for all coatings. To reach a coating thickness of approximately 3 µm, the deposition time was varied between 60-90 minutes.

Table 3.8 Deposition parameters for the CrAlN coatings with Re.

Coating	Number of targets	I_{Cr} [A]	I_{Re} [A]	P_{tot} [Pa]	Substrate	Time [min]
Re N°1	2x CrAl25, 1x Re	0.35	0.02	0.4	Si	60
Re N°2	2x CrAl25, 1x Re	0.35	0.06	0.4	Si	60
Re N°3	2x CrAl25, 1x Re	0.35	0.1	0.4	Si	60
Re N°4	2x CrAl25, 1x Re	0.35	0.02	0.4	HSS	90
Re N°5	2x CrAl25, 1x Re	0.35	0.06	0.4	HSS	90
Re N°6	2x CrAl25, 1x Re	0.35	0.1	0.4	HSS	90

3.2 Coating Characterization

3.2.1 Coating Thickness Evaluation

The thickness of a film is a fundamental information because many thin film properties like coating adhesion or residual stresses depend on thickness. Furthermore, other testing parameters depend on the knowledge of the film thickness, for example to define the depth of indentation for the evaluation of nanoindentation hardness. There are different ways to measure film thickness which can be divided in non-destructive and destructive methods. In this work, a quick and simple method belonging to the destructive methods, the ball crater technique (CSM Calotest), was used. A round crater is grinded in the coating surface due to the interaction of abrasive particles present in a slurry (liquid diamond suspension) with the coating surface, under the load of a rotating steel ball (see Fig. 3.3). The outer

diameter (Do), which marks the film surface and the inner diameter (Di), which marks the interface film/substrate are measured by using a light optical microscope. Given that the film thickness is significantly smaller than the radius of the steel ball R, the film thickness t_c can be calculated with the equation [42]:
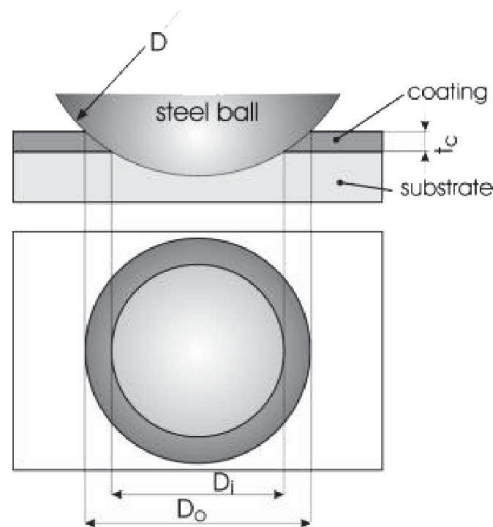
$$t_c = \frac{Do^2 - Di^2}{8 \cdot R}.$$ (3.1)

Fig. 3.3 Schematic view of the ball crater technique [17].

## 3.2.2 X-ray Diffraction Analysis

X-ray diffraction (XRD) is a non-destructive testing method for determining the internal structure of solids. The main applications are phase and texture analyses, but also stress and grain size might be determined [43]. In this work, XRD was used mainly for phase analysis. The measurements were carried out with a Siemens D500 Diffractometer with Bragg-Brentano geometry. Table 3.9 lists the main parameters for the measurement. Fig. 3.4 shows the beam path of the diffractometer, which irradiates the sample at an angle θ to the surface. The diffracted beam is detected at an angle 2θ with respect to the incident beam. The sample rotates at half angular velocity with respect to the detector. This is called a θ-2θ scan, which allows investigating lattice planes with the plane normal parallel to the diffraction vector. The diffraction pattern results from the interference of the scattered beam with the investigated sample. If the Bragg condition [43]

$$n \cdot \lambda = 2d_{hkl} \cdot \sin\theta$$ (3.2)

is fulfilled, constructive interference occurs. n indicates the class of diffraction, λ is the wavelength of the radiation, d_{hkl} is the interplanar spacing of a lattice plane with the Miller indices h, k and l and θ designates the diffraction angle.

Table 3.9 Parameters for XRD measurements.

λ Cu Kα [nm]	High Voltage [kV]	Tube Current [A]	Step Time [s]	2θ step [']	2 θ range [']
0.154056	40	30	1.2	0.02	35-85
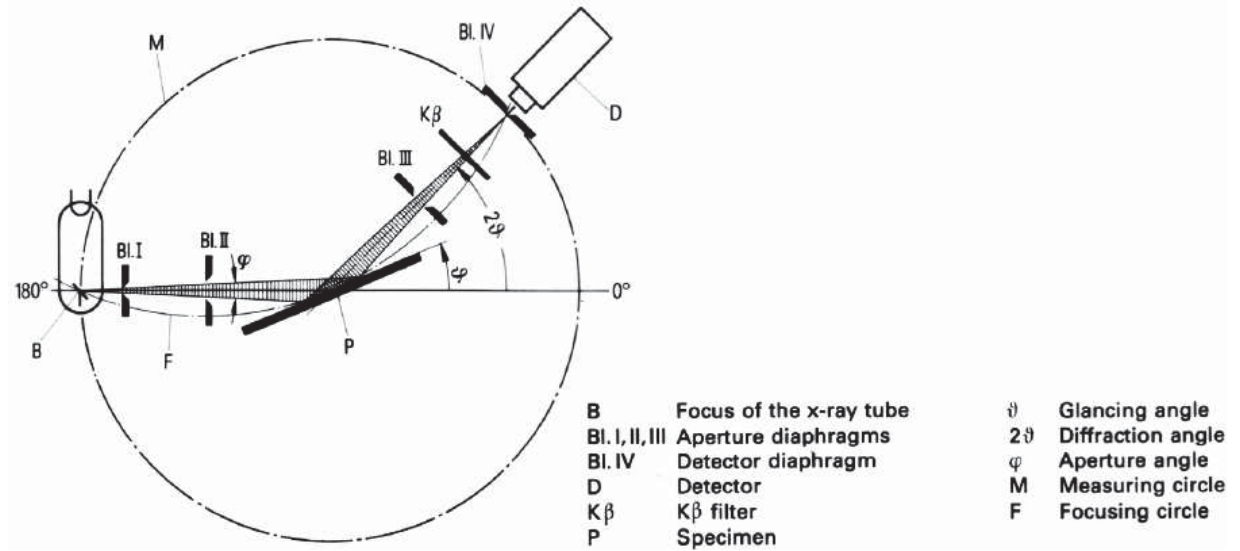
Fig. 3.4 Beam path of the Siemens D500 diffractometer [44].

Phase identification was carried out by comparing peak positions (2θ) and relative line intensities with the JCPDS power diffraction files.

Additional information about the crystal is given by the position of the peaks and the peak broadening in the diffraction pattern. Grain size and inhomogeneous strain, so called micro-stress, are the contributions to the peak broadening. Micro-stresses in crystallites are produced from coating defects like vacancies. Deviations of the peak position indicate the presence of uniform strain in the material, so called macro-stress [45].

It is possible to separate the contributions to the peak profile whether size (Cauchy function) or strain (Gaussian function) effects are dominating with a Pseudo-Voigt function. This is the linear combination of a Cauchy and Gaussian function [17]:

$$f(x) = f_o + A \cdot \left[\eta \cdot f_{Cauchy} + (1-\eta) \cdot f_{Gaussian} \right] \qquad (3.3)$$

$$f(x) = f_o + A \cdot \left[\eta \cdot \frac{2}{\pi} \cdot \frac{w_{hm}}{4(x-x_c)^2 + w_{hm}^2} + (1-\eta) \cdot \frac{\sqrt{4\ln 2}}{\sqrt{\pi} \cdot w_{hm}} \cdot e^{\frac{4\ln 2}{w_{hm}^2} \cdot (x-x_c)^2} \right] \qquad (3.4)$$

A indicates the peak area, f_o the mean background level, η the Cauchy content, w_{hm} the full width at half maximum and x_c the position of the peak maximum. The Cauchy and Gaussian components can be calculated by the ratio of the FWHM to the integral breath ($\frac{2w_{hm}}{\beta}$). The integral breath β can be calculated from the ratio of the peak area and the maximum intensity ($\frac{A}{f(x_{c)}}$) [17]:

$$\frac{\beta_c}{\beta} = 2.0207 - 0.4803 \frac{2w_{hm}}{\beta} - 1.7756 (\frac{2w_{hm}}{\beta})^2 \tag{3.5}$$

$$\frac{\beta_G}{\beta} = 0.642 + 1.4187 \cdot \sqrt{\left(\frac{2w_{hm}}{\beta} - \frac{2}{\pi}\right)} - 2.2043 \cdot \frac{2w_{hm}}{\beta} + 1.8706 \cdot \left(\frac{2w_{hm}}{\beta}\right)^2 \tag{3.6}$$

C and G indicate the Cauchy and Gaussian components. The crystallite size d is calculated by [17]:

$$d = \frac{\lambda}{\beta_C \cdot \cos\theta_C} \tag{3.7}$$

and the strain is given by

$$e_{st} = \frac{\beta_G}{4\tan\theta_G} . \tag{3.8}$$

where λ is the wavelength of the used radiation and θ is the position of the peak maximum.

3.2.3 Scanning Electron Microscopy

A scanning electron microscope (Zeiss Evo50 SEM) was used for the investigation of the coating morphology and structure, and of the wear tracks after tribological testing. The chemical composition of the coatings were measured using an attached energy-dispersive X-ray analysis (Oxford Instr. INCA EDX) system with a Co-standard.

Images of the surfaces and fracture cross-sections of the silicon substrates were recorded with secondary electron imaging mode, where low energy (<50 eV) secondary electrons are monitored which originate from a depth around several Ángstroms beyond the surface. High resolution and information on the surface topography can be achieved.

The images of the wear tracks were also recorded with backscattered electron imaging mode. Backscattered electrons have high energies and, since the probability for backscattering is rising with the atomic number Z, it can lead to development of images with high contrast between areas of the sample which have different atomic numbers. This allows the detection of oxide phases, for example. The disadvantage is the lower topological contrast in the images compared to the secondary electron imaging mode [46].

3.2.4 Evaluation of Micro hardness and Elastic Modulus

Measurements of hardness (H) and Young's modulus (E) were performed with an UMIS nanoindenter. A hard indenter, which has a precisely calibrated shape, is pressed into the surface of the specimen and the resulting indentation depth and the load is continuously monitored [47]. In this work a Berkovich indenter, which is a three-sided diamond pyramid with a sharply pointed tip, was used (see Fig. 3.5) [4, 48].
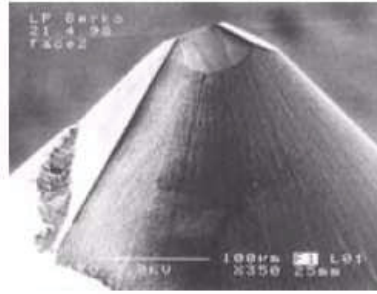

Fig. 3.5 The Berkovich indenter: a three-sided (triangular-based) pyramid with a nominal angle of 65.3° between the side face, and t he normal to the base at apex, an angle of 76.9° between edge and normal, and with ti p radius less than 0.1 μm [4, 48].

The nanoindenter can perform in force or depth control mode. In the force control mode, the indenter is moved until the requested force is reached. In the depth control mode, the indenter moves until the requested depth is reached. In this work, all measurements were conducted in the force-controlled mode [47].

Fig. 3.6 shows a typical load-displacement curve. The hardness can be calculated by dividing the indentation force (P) by the contact area (A) [48]:

$$H = \frac{P}{A} \cdot \left(\frac{Ai}{A} \right) \tag{3.9}$$

The contact area A is calculated from the knowledge of the geometry of the tip and the indentation depth h_p.

The unloading curve is assumed to be elastic, even if the loading curve has a plastic deformation fraction. From the slope of the unloading curve, which correlates with the stiffness (dP/dh), the elastic modulus can be calculated [48]:

$$E = \frac{dP}{dh} \cdot \frac{\sqrt{\pi}}{2\beta\sqrt{A}} \cdot \sqrt{\frac{Ai}{A}} \tag{3.10}$$

Ai/A is the area ratio, which is applied to the results as a correction for the non-ideal indenter geometry.
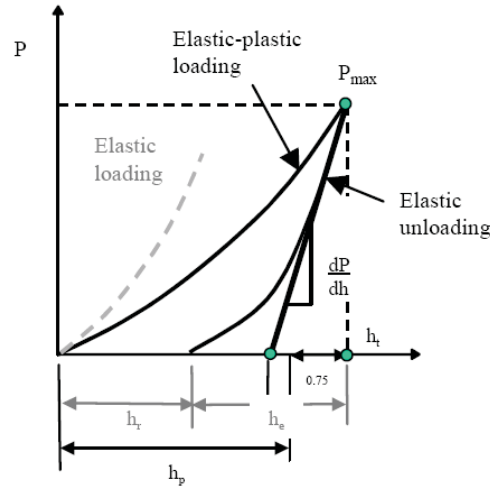
Fig. 3.6 Load-displacement curve [48].

To eliminate the influence of the substrate during the measurements, the indentation depth has to be small compared to the coating thickness. In this work, the coating is harder than the substrate. If the plastic zone reaches the coating-substrate interface, the measured hardness decreases. On the opposite side, if the indentation depth is not large enough and thus the plastic zone is not entirely developed yet, the result coincides with the theoretical hardness of a single crystal [49-51]. For this reason, the indentation depth was chosen in the range of 1/10 of the coating thickness. In order to find out the right testing load, indentation tests with varying load from 5 to 50 mN were conducted. The right load was chosen in such a way that the two conditions were fulfilled, namely no influence from substrate and fully developed plastic zone. The CrN, CrAlN and the CrAlN-Ag coatings were tested with a load of 15 mN, while 25 mN was applied on the CrAlN-Re and CrAlN-Nb coatings. All values of hardness and elastic modulus were calculated from 15 indents with constant load.

3.2.5 Coating Biaxial Stress Temperature Measurements

General failure mechanisms of thin films in technical applications are the loss of adhesion, film cracking and film yielding which are driven by stresses in the films. There are two components which contribute to the residual stresses (σ_{res}): the extrinsic thermal residual stresses (σ_{th}) and the intrinsic residual stresses (σ_{int}). The former originate due to different thermal expansion coefficient of coating and substrate and arise during cooling and heating. The latter are generated by inhomogeneous strains during nucleation and growth [4, 52]:

$$\sigma_{res} = \sigma_{th} + \sigma_{int} \tag{3.11}$$

After deposition and during cooling, extrinsic stresses increase according to [19]

$$\sigma_{th} = -\frac{E_c}{1-v_c} \cdot (\alpha_c - \alpha_s)(T_c - T_o) \tag{3.12}$$

$\dfrac{E_c}{1-v_c}$ indicates the biaxial elastic modulus of the coating, v_c the Poison's ratio of the coating, α_s and α_c are the thermal expansion coefficients of substrate and coating respectively, T_c is the current temperature and T_0 is the initial temperature.

If the coating is deposited only on one side of the substrate and is not too thick, the stresses in the coating force the whole sample to bend. The resulting curvature can be observed mainly in the length direction of a rectangular substrate, and less pronounced in its width direction. Residual compressive stresses lead to a downward bending, residual tensile stresses to an upward bending, if the coated surface is the upper surface [4].

A method to measure the residual stresses is to determine the curvature of the sample. A schematic view of a bended sample is given in Fig. 3.7. l_x is the length of the sample, l_y the width, t_c the coating thickness and t_s the substrate thickness. The stress components in x, y, and z direction are σ_x, σ_y and σ_z.
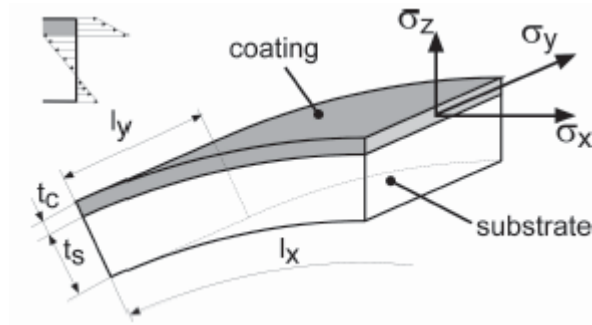

Fig. 3.7 Schematic view of a bended sample with the typical stress distribution through the thickness of the sample [24].

The normal stress σ_{zz} and the corresponding shear stresses τ_{xz} and τ_{yz} can be neglected, if the coating is very thin compared to the substrate ($100 \cdot t_c = t_s$) because then no forces can act on the upper surface. For l_x, l_y >> $t_c + t_s$ the sample should demonstrate biaxial stresses in the x and y- direction. The modified Stoney equation can then be taken to calculate the residual biaxial stresses using the radius of curvature (r) [24]

$$\sigma = \frac{E_s}{1-v_s} \cdot \frac{t_s^2}{6t_c} \cdot \left(\frac{1}{r} - \frac{1}{r_0} \right) \tag{3.13}$$

if the following conditions are fulfilled: the substrate curvature is much larger than the substrate thickness and the width of the substrate is less than half the length. σ indicates the biaxial stress in the x-direction, $\dfrac{E_s}{1-v_s}$ is the elastic modulus of the

substrate, v_s is the Poisson's ratio and r_o is the radius of curvature before the deposition. The measurement assembly is shown in Fig. 3.8. The curvature of the sample is measured with two parallel laser beams by detecting the position of the reflected beams during the heating and cooling steps. To fulfil the conditions mentioned above, the thickness of the coatings deposited on the silicon samples (20 x 7 x 0.35 mm³) was approximately 3 µm [53].
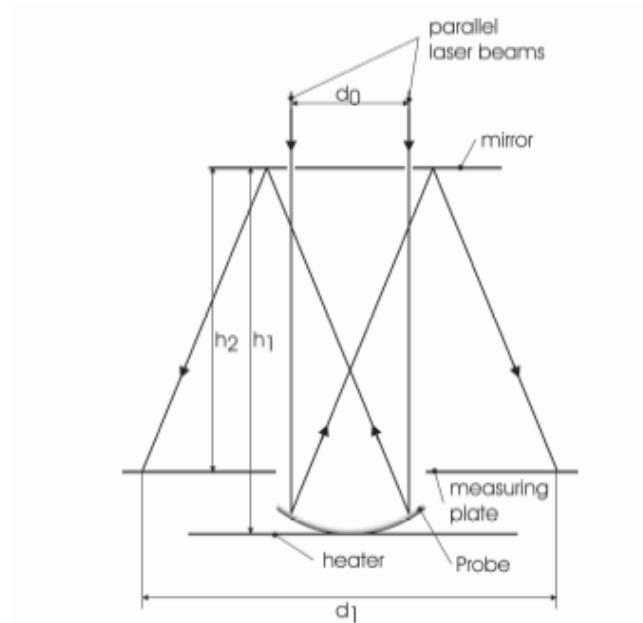

Fig. 3.8 Principle of the residual stress measurement [53].

The radius of curvature is given by the equation [24]

$$r = \frac{2 \cdot (h_1 + h_2) \cdot d_o}{d_o + d_1}$$

(3.14).

d_o is the distance between the two parallel laser beams, d_1 is the deflection between the measured laser beams and (h_1+h_2) is the total distance between the sample and the measuring plate. The samples are put onto a heating plate and to prevent oxidation during the heating, the measurements are conducted under vacuum (pressure~10^{-6} Pa). All samples were heated up to a maximum temperature of 500℃. The heating and the cooling rate were set to 5 K/min. During heating, the deflection d_1 was measured every 25℃ and during cooling, every 50℃.

3.2.6 Electrical Resistance

The electrical resistance was measured with a MDC Multi Height Probe System on the coated silicon samples. The principle of this system is based on the measurement of the area resistance. It consists of a 4-point probe of 4 equal tungsten tips (see Fig. 3.9). Through the two outer tips a current is provided from a

high impedance current source. Between the inner tips, the voltage decreases as a result of the resistance of the measured coating. This voltage is measured with a voltmeter. The electrical resistance ρ of the samples is calculated by [54]

$$\rho = \frac{\pi \cdot t_c}{\ln 2} \cdot \frac{U}{I} \qquad (3.15)$$

t_c is the coating thickness, U is the measured voltage and I is the adjusted current. The electrical conductivity σ is calculated by [55]

$$\sigma = \frac{1}{\rho} \qquad (3.16).$$

Requirement of this measurement is that the current is driven through the coating and not trough the substrate. This is achieved by using a substrate that has a higher electrical resistance than the coating.
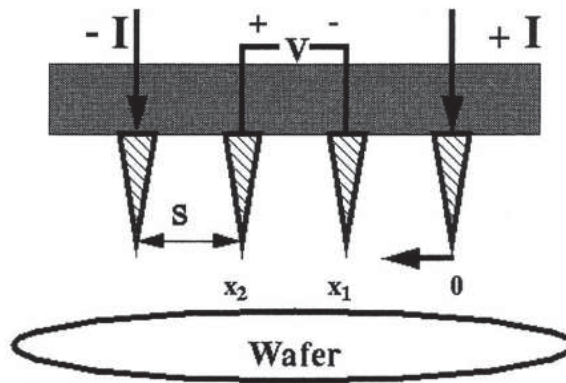

Fig. 3.9 Schematic image of the electrical resistance measurement [54].

3.2.7 Tribological Testing

3.2.7.1 Friction

A CSM high temperature ball-on disc tribometer was used to determine the friction and wear behaviour of the investigated coatings. The CSM assembly is shown in Fig. 3.10. It consists of a stationary top-mounted ball that grinds against a unidirectional rotating disc, which can reach a speed up to 500 RPM. The lever with the ball assembly can be loaded with well-defined weights in the range from 1 N to 20 N and the lever can be adjusted to the position of the wear track on the specimen. The tribometer can perform in a temperature range from room temperature up to 1000°C. During the experiment, the coefficient of friction is recorded as function of the sliding distance.
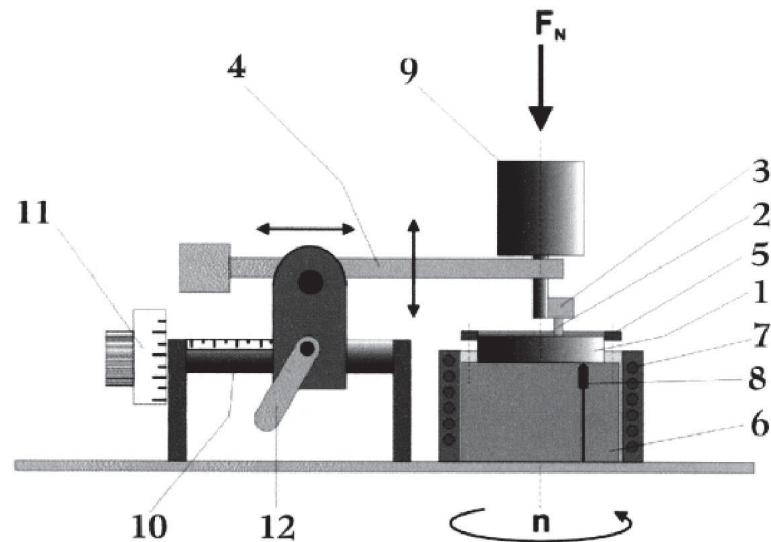
Fig. 3.10 Schematic of the tribometer. 1...specimen, 2…ball, 3…ball holder, 4…lever, 5…locking ring 6…rotation cylinder, 7…heating, 8…thermocouple, 9…cylindrical force, 10…variable axis for adjustment of radius, 11…adjusting screw for radius, 12…lock for the lever arm [56].

All coatings investigated in this work were deposited on high speed steel and tested at room temperature and 200℃ using Al_2O_3 balls ($\varnothing$ 6 mm) as counterface in air with humidities around 30-40%. Load, linear speed and sliding distance were kept constant at 2 N, 0.1 m/s and 100 m respectively. The radius of the wear track was 7 mm for the room temperature tests and 5 mm for the 200℃ tests.

3.2.7.2 Surface Morphology and Wear

Measurements of surface roughness, 2D and 3D depth profiles of the wear tracks after tribometer testing were done with a Vecco Wyko NT1000 optical profilometer in the VSI (vertical scanning interferometry) mode. Fig. 3.11 shows the principle of an optical profilometer. A white light beam is reflected down to the objective after filtering with a neutral density filter which retains the short coherence length of the white light. A second beam splitter in the Mirau interferometer splits the light beam into two beams. One beam passes through the objective to the sample surface, the other is reflected at the reference mirror within the interferometer. After reflecting at the different surfaces, the beams recombine and form an interference pattern which can be detected by a CCD camera. The highest contrast (or modulation) appears for a surface point which is in focus, and it drops rapidly when moving away from the focus position. The objective moves vertically and rasters the surface at varying heights with the aim to get information about the vertical position of each point on the surface. A motor with feedback from a linear variable differential transformer precisely controls the motion. The irradiance signal is sampled at fixed intervals as

the optical path difference is varied by a continuous translation of the vertical axis through focus. The system uses a series of computer algorithms to demodulate the envelope of the fringe signal. Finally the vertical position corresponding to the peak of the interference signal is extracted for each point on the surface. In this way, a 3D surface profile reconstruction and 2D cross sections can be calculated [57, 58]. Roughness statistics, originally defined as 2D parameters, were adjusted to describe 3D surfaces. In this work surface roughness was characterized using Ra (roughness average) and Rq (root mean square (RMS) roughness). Ra is the arithmetic mean of the absolute values of the surface deviations from the mean plane. Rq is obtained by squaring each height value and then taking the square root of the mean. Ra is calculated by [58]

$$Ra = \frac{1}{M \cdot N} \sum_{j=1}^{M} \sum_{i=1}^{N} |Zji| \qquad (3.17)$$

and Rq by [58]

$$Rq = \sqrt{\frac{1}{M \cdot N} \sum_{j=1}^{M} \sum_{i=1}^{N} Z^2(xi, yj)} \qquad (3.18).$$

M and N indicate the number of data points, and Z designates the respective height of the data point relative to the reference mean plane.
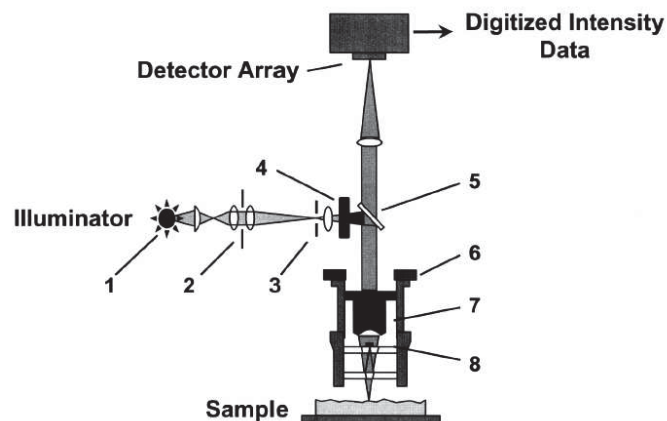

Fig. 3.11 Schematic of an Interference Microscope. 1…Light source,2…Aperture stop, 3…Field stop, 4…Filter, 5…Beam splitter, 6…Translator, 7…Microscope objective, 8…Mirau Interferometer [58].

3.2.7.3 Evaluation of Coating Adhesion

The adhesion of the coatings to the high speed steel substrates was investigated with a Rockwell indentation test (Rockwell C, DIN 50103 Part 1). After indentation, an image of the indent was made with a light optical microscope which is connected to a CCD camera. The indent was compared with the adhesion table shown in Fig. 3.12.

The VDI standard defines six different categories, where HF1 shows the best adherence with a fine crack network around the indent. It is diminishing towards HF5 which shows worse adherence with massive crack propagation and delamination of the coating. HF6 shows the worst adherence. HF5 and HF6 do not have adequate adhesion for technical applications.
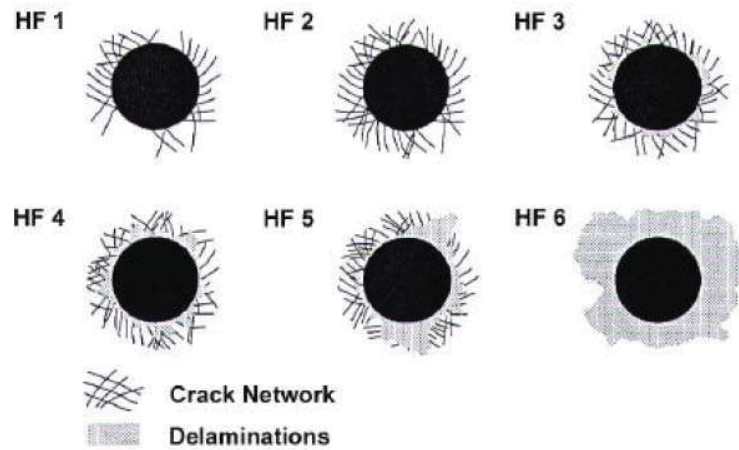

Fig. 3.12 Adhesion table [59].

4   Results and Discussion

4.1 Preliminary Tests

The first step of the present work was to deposit different CrN_x films on silicon substrates by varying the gas flow rates of Ar and N_2 in order to find the right parameters to deposit stoichiometric CrN films. The as-deposited coatings were investigated by XRD in order to determine the phases present in the different coatings. Fig. 4.1 shows XRD patterns of the deposited CrN_x films as function of the total pressure p_{tot} and N_2 fraction in the working gas. The N_2 fraction is defined as the partial pressure of N_2 divided by p_{tot} and expressed as percentage of p_{tot}. The strong peak at approximately 70° belongs to the silicon su bstrate.
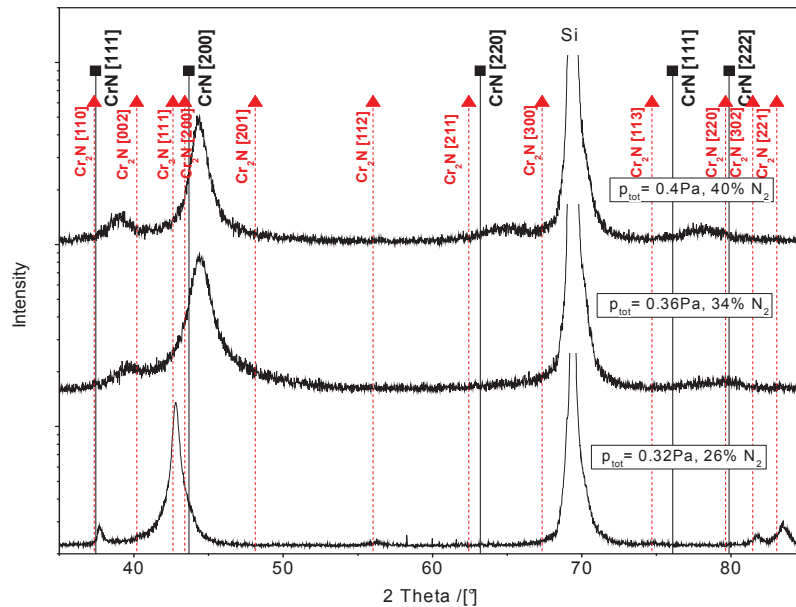

Fig. 4.1 XRD-patterns of CrN coatings deposited on silicon substrates with varying total pressure p_{tot} and N_2 fraction in the working gas.

The XRD pattern at the bottom of Fig. 4.1 belongs to the film deposited with a N_2 fraction of 26%. The pattern shows peaks which are close to the position of the hexagonal Cr_2N phase at $2\theta=37.35°$ (110), 42.611° (111), 56.012° (112), 81.441 ° (302) and at 83.050° (221) (cf. JCPDS 00-035-0803). The coating grows with a preferred [111] orientation. Increasing p_{tot} and the N_2 fraction in the working gas (34% N_2) results in a film which consists basically of the face-centered cubic (fcc) CrN phase. The strong peak at $2\theta\sim44.2°$ is considered to be the $2\theta=43.738°$ (200) peak of the fcc CrN phase, which is slightly shifted to higher 2θ angles (cf. JCPDS 00-11-0065). This broad and slightly asymmetric peak in the pattern at $2\theta\sim39°$ reveals

probably the presence of some hexagonal Cr_2N phase in the film. Beside this peak, only a very broad reflection at a 2θ angle of about 39° and a weak peak between 78° and 81° can be detected which might be a superposit ion of Cr_2N and CrN peaks in both cases. A further increase in both p_{tot} and in the N_2 fraction in the working gas (40% N_2) results in the formation of a single phase CrN coating. The strong peak at 2θ~44.2° is again regarded as the (200) peak of the C rN phase. The weak and broad peaks at 2θ~39°, 2 θ~65° and 2 θ~78° are considered to be the 2 θ=37.539° (111), 2θ=63.541° (220) and 2 θ=76.156° (311) peak of the fcc CrN phase. This reve als that the coating grows with a preferred [200] orientation. All CrN peaks are shifted to higher 2θ angles indicating the presence of tensile stresses which might be the result of the growth structure of the coating due to the relatively low deposition temperature. No clear Cr_2N peaks are observable. Therefore, a $pN_2/(pN_2+pAr)$ ratio of 40% at p_{tot}=0.4 Pa was defined as optimum parameter for the deposition of CrN and further on CrAlN and CrAlXN coatings.

4.2 Phase Analysis and Chemical Composition

4.2.1 Chemical Composition

The chemical composition of the coatings was measured by energy-dispersive X-ray analysis (EDX). Tables 4.1-4.4 show the chemical composition of the different coating systems. The denomination of the coatings was calculated assuming a substitution of Cr atoms by other metallic atoms starting from 100% Cr in CrN due to the uncertainty of N analysis by EDX.

Table 4.1 Chemical composition of the CrAlN coating.

coating composition [at.%]				coating	coating thickness [μm]
N	Cr	Al	-		
58.8	28.6	9.9		$Cr_{75}Al_{25}N$	2.7

Table 4.2 Chemical composition of the CrAlN-Ag coatings.

coating composition [at.%]				coating	coating thickness [μm]
N	Cr	Al	Ag		
58.8	28.6	9.9	2.8	$Cr_{69}Al_{24}Ag_7N$	3.4
64.0	23.1	7.6	5.3	$Cr_{64}Al_{22}Ag_{14}N$	2.5
65.7	20.1	6.5	7.8	$Cr_{58}Al_{19}Ag_{23}N$	2.8

Table 4.3 Chemical composition of the CrAlN-Nb coatings.

coating composition [at.%]				coating	coating thickness [µm]
N	Cr	Al	Nb		
53.0	29.6	10.3	7.0	$Cr_{63}Al_{22}Nb_{15}N$	3.6
54.8	23.4	8.0	13.8	$Cr_{52}Al_{17}Nb_{31}N$	3.5
55.6	20.3	6.9	17.2	$Cr_{45}Al_{16}Nb_{39}N$	3.6

Table 4.4 Chemical composition of the CrAlN-Re coatings.

coating composition [at.%]				coating	coating thickness [µm]
N	Cr	Al	Re		
51.7	35.2	11.6	1.5	$Cr_{72}Al_{25}Re_3N$	3.0
48.4	33.9	11.2	5.9	$Cr_{66}Al_{22}Re_{12}N$	3.1
47.4	32.6	10.0	10.0	$Cr_{61}Al_{19}Re_{20}N$	3.2

4.2.2 Coating Morphology

The coating morphology was determined on fracture cross-sections by SEM, as shown in Fig. 4.2 for one sample of each coating system. All coatings exhibit a dense and columnar structure. For the deposition of the different films, constant sputtering process parameters like sample temperature, total pressure and bias voltage have been used. Although different target powers were used for the Ag, Nb and Re targets, which might have yield changes in the plasma during deposition, there seems to be no apparent consequences to the morphology of the coatings.

4.2.3 Phase Analysis

CrAlN

Fig. 4.3 shows the XRD-patterns of CrN and CrAlN coatings deposited on HSS substrates. For both coatings, a bias voltage of -80 V was applied during the deposition. The HSS substrate peaks are indicated in Fig. 4.2 by blue drop lines. The peaks at 2θ angles of ~37°, ~43°, ~63°, ~76° and ~80° match the fcc CrN peaks at $2\theta=37.539°$ (111), $2\theta=43.738°$ (200), $2\theta=63.541°$ (220), $2\theta=76.156°$ (311) and $2\theta=80.110°$ (222) for both patterns. In the CrN pattern, the peaks are shifted to higher diffraction angles. In case of CrAlN, the peaks nearly perfectly match the standard positions of the fcc CrN peaks. In the upper pattern (CrAlN), the intensity of the (111) peak is increasing, whereas the intensity of the (200) and (220) peaks diminishes compared to the pattern of CrN. The intensity of the (311) and (222) peaks do not vary significantly.
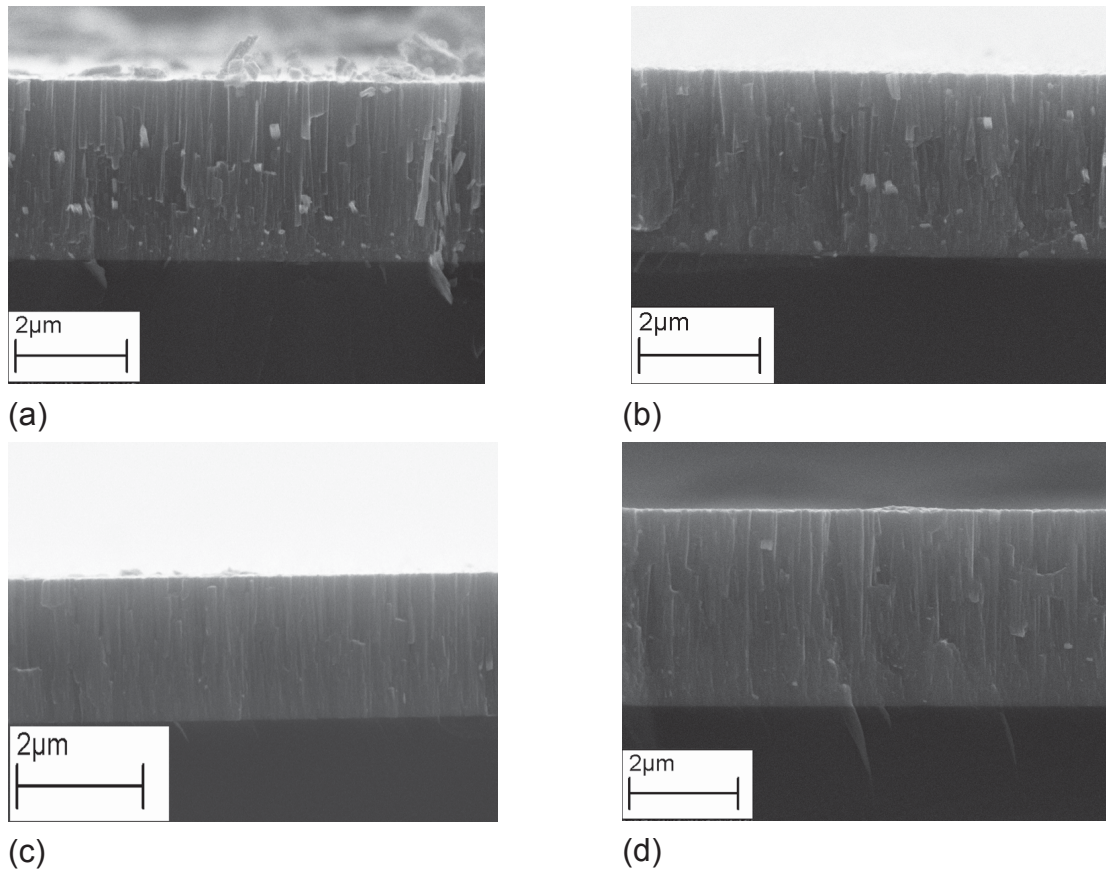
Fig. 4.2 SEM fracture cross-sections of (a) a CrAlN coating, (b) a CrAlN coating with 2.8 at.% Ag, (c) a CrAlN coating with 1.5 at.% Re and (d) a CrAlN coating with 7 at.% Nb on silicon substrate.

The peak deviation to higher diffraction angles in the CrN coating results from the presence of tensile stresses as mentioned before. In case of the CrAlN coatings, it is assumed that the Al atoms in the CrAlN coating are built in the CrN lattice. Due to the larger size of the Al atoms, the lattice parameter should increase, and consequently, the peaks shift to lower diffraction angles compared to the CrN coating. There is no evidence for the formation of the hexagonal Cr_2N phase or the AlN phase in the CrAlN coating. On account of this, it is obvious that the CrAlN coating exhibits a single phase structure. Furthermore, the preferred (200) orientation of the CrN coating changes into a (111) orientation for the CrAlN coating.
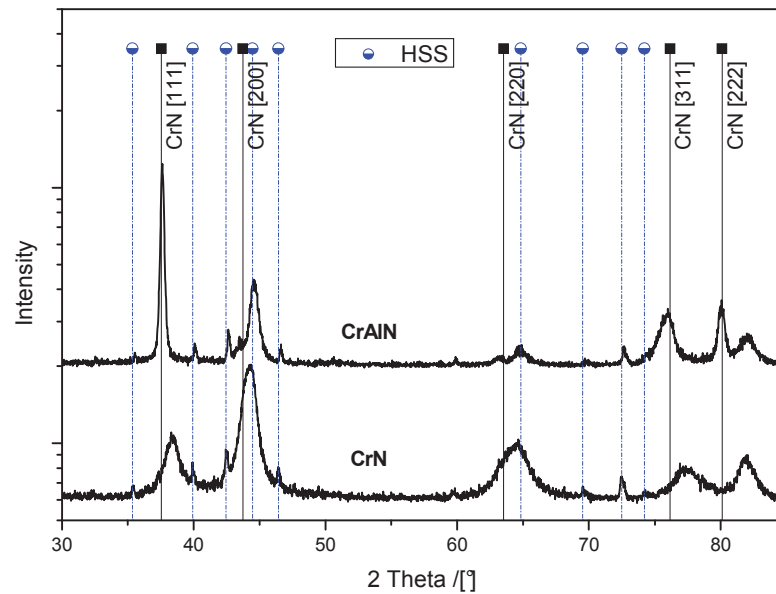
Fig. 4.3 XRD-patterns of a CrAlN and a CrN coating on HSS substrate.

CrAlN-Ag

Fig. 4.4 shows the XRD-patterns of coatings with increasing Ag content on silicon substrate. The Ag-content in the coatings ranges between 2.8 at.% and 7.8 at.%. The strong peak at approximately 70° and the small peak at $2\theta=32°$ correspond to the silicon substrate. The peaks in both patterns match perfectly with the JCPDS data for the fcc CrN peaks at $2\theta=37.539°$ (111), $2\theta=43.738°$ (200), $2\theta=76.156°$ (311) and $2\theta=80.110$ (222) (cf. JCPDS 00-11-0065). The (111), (200) and the (222) peaks have almost the same intensity independent of the Ag content in the coating, while the intensity of the (311) peak decreases with increasing Ag content. Unfortunately, most CrAlN peaks overlap with the positions of the fcc Ag peaks. The peak at 38.116° shows an asymmetry on the right side which is more visible the higher the Ag content is. This is a clear signal of the overlapping of CrAlN and Ag peaks. An additional peak at ~63° can be detected in the pattern of the sample with 7.8 at.% Ag which might correspond to the (220) CrAlN peak or to the (220) Ag peak.

A solid solution of Ag in the CrAlN lattice is possible. However, due to the presence of the shoulder in the (111) peak for all Ag contents, it can be assumed that Ag forms an additional metallic phase. The fraction of the Ag phase in the coating increases with increasing Ag-content as the shoulder height increases as well. The peak at $2\theta\sim63°$ might belong to Ag as it appears only for the highest Ag content.

A slight shift of the peaks to higher diffraction angles indicates lower stresses with increasing Ag-content.
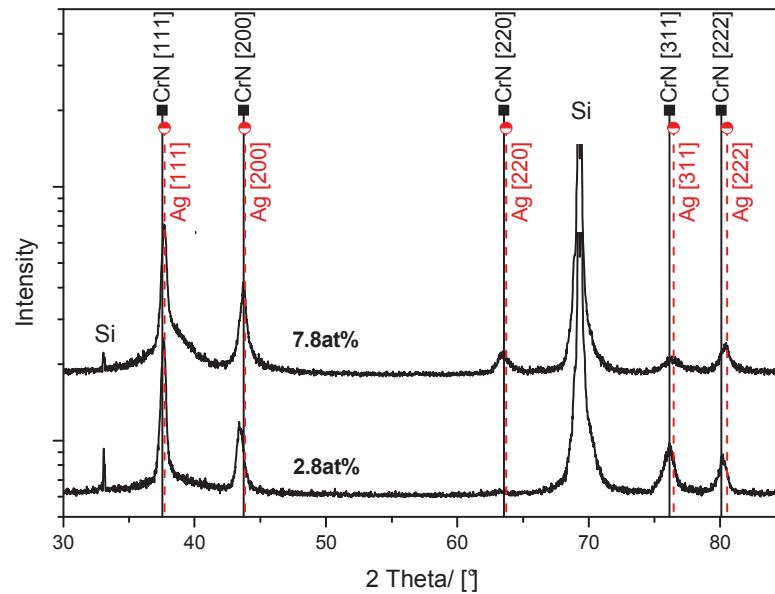
Fig. 4.4 XRD-patterns of CrAlN coatings with different concentrations of Ag on silicon substrate.

CrAlN-Nb

Fig. 4.5 shows the XRD-patterns of coatings with increasing Nb-content on silicon substrate. The coatings have a Nb-content of 7 at.%, 14 at.% and 17 at.%. The strong peak at approximately 70° and the small peak at $2\theta=32°$ correspond to the silicon substrate. All patterns show peaks which correspond to the CrAlN phase (cf. chapter 4.2.1). In general, the CrAlN peaks are shifted to lower diffraction angles. The peak shift for the patterns with Nb-contents of 14 at.% and 17 at.% is larger, but there is nearly no difference in the peak positions between these two patterns. For Nb-contents of 14 at.% and 17 at.%, hexagonal ε-NbN peaks can be detected as well. Most of the hexagonal ε-NbN peak positions are overlapped with the positions of the CrAlN peaks. Therefore, the CrAlN peaks exhibit a broadening in these patterns. An additional hexagonal ε-NbN peak at $2\theta=34.967°$ (100) can be observed. It seems that the (111) peak of CrAlN has a right and left shoulder which might possibly originate from the overlapping of the (111) peak with the hexagonal ε-NbN peaks at $2\theta=35.907°$ (101) and $2\theta=38.525°$ (102). The intensity of both the (200) peak and the (220) peak is increasing with increasing Nb content. The (111) peak exhibits a maximum intensity in the pattern with a Nb-content of 14 at. %. The intensity of the peak at $2\theta\sim74°$ increases in case of the coating with 14 at. % Nb.
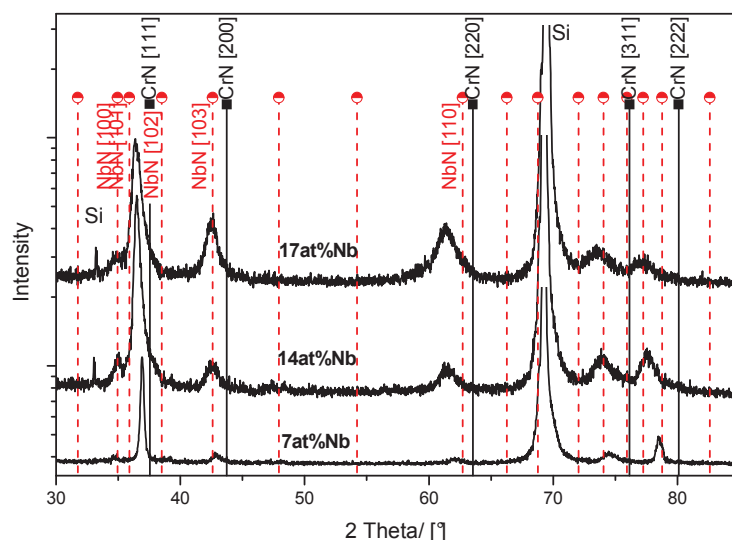
Fig. 4.5 XRD-patterns of CrAlN coatings with different concentrations of Nb on silicon substrate.

Concluding, it can be said that the coating with a Nb-content of 7 at. % might exhibit a single phase structure with Nb atoms incorporated in the CrAlN lattice. The formation of an additional phase, namely hexagonal ε-NbN, can be observed for the coatings containing 14 at.% and 17 at.% Nb. The peaks at $2\theta\sim42°$ and $2\theta\sim61°$ might be attributed to hexagonal ε-NbN peaks They could be also attributed to the CrAlN (200) and (220) orientations, but the peak shift is too pronounced. The peak broadening of the CrAlN (111) orientation might also indicate a decrease in grain size. The general shift of the peaks to lower diffraction angles results from compressive stresses in the coatings, which increase with higher Nb-content.

CrAlN-Re

Fig. 4.6 shows XRD-patterns of coatings with increasing Re-content on silicon substrate. The coatings have Re-content of 1.5 at.%, 6 at.% and 10 at.%. The strong peak at approximately 70° and the small peak at $2\theta=32°$ correspond to the silicon substrate. The peaks at 2θ angles of ~37°, ~43°, ~63°, ~76° and ~80° match wi th the fcc CrN peaks in all three coatings (cf. JCPDS 00-11-0065). These peaks are shifted to higher diffraction angles with increasing Re content. Unfortunately, some of the hexagonal Re peaks overlap with the CrAlN matrix peaks. The peak at $2\theta=40.439°$ in the pattern of the 10 at.% Re-coating can be attributed to the (002) peak of hexagonal Re. This peak might be already visible in the coating with a Re-content of 6 at.%. With increasing Re content, the intensity of the (111), (200), (220) and (222) CrAlN peaks increases, whereas the (220) peak is only visible in the pattern with the

highest Re-content. The increase in the intensity of the peaks might implicate an increase in crystallinity with increasing Re content.

For 1.5 at.% Re, the coating might only exhibit a single phase structure with solid-soluted Re atoms in the CrAlN matrix. The formation of an additional hexagonal Re phase is clearly observed for the coating containing 10 at. % Re, but probably the hexagonal phase is already formed in the coating containing 6 at.% Re. The same preferred (111) growth orientation as in all the other coating systems is observed. It is possible that, besides grain coarsening, the (200), (220) as well as the (222) orientations are stabilized with increasing Re-content. The shift of the CrAlN peak positions to lower diffraction angles for the sample with 6 at.% Re might indicate slightly higher compressive stresses compared to the sample with 1.5 at.% Re, while the sample with 10 at.% Re shows slightly lower stresses (peak shift to higher diffraction angles). However, the shift in the peak from 1.5 at.% Re to 6 at.% Re might be connected to the formation of the Re phase, as well as the increase in the intensity of the (111) CrN peak. Since there is a shift of the peak to higher 2θ angles from 6 -10 at.% Re and a further increase in the (111) peak height, this might indicate a reduction of stresses with increasing Re-content.
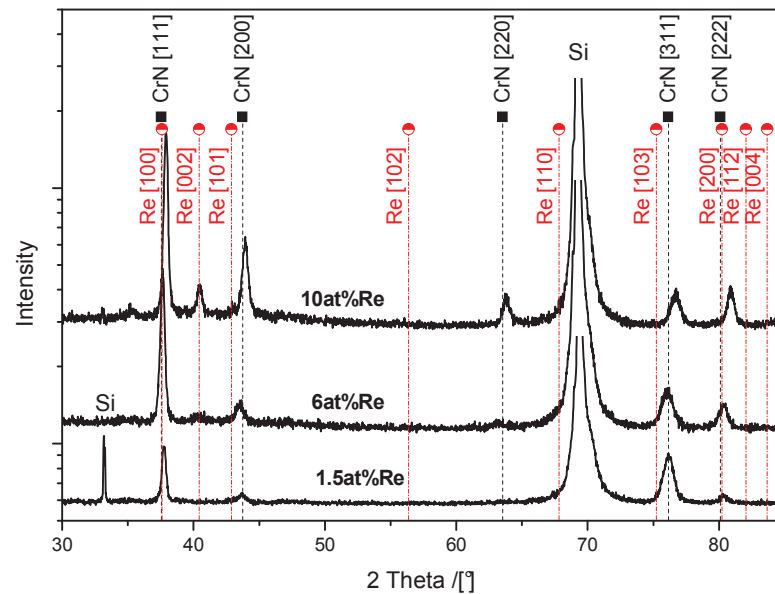

Fig. 4.6 XRD-patterns of CrAlN coatings with different concentrations of Re on silicon substrate.

4.3 Mechanical Properties

4.3.1 Coating Thickness

For characterization of mechanical properties, the knowledge of coating thickness is often necessary, e.g. to determine the maximal indentation depth in nanoindentation. The coating thicknesses of the different coatings deposited on HSS substrates are presented in Table 4.1-4.4. The sputter rate depends on the material, the total pressure, the applied target voltage and current density [4]. Since different target powers were necessary to obtain different film compositions, the deposition time had to be adjusted between 55-90 minutes in order to reach an average coating thickness of approximately 3 µm. Nevertheless, the obtained coating thickness ranges from 2.1 µm to 3.6 µm. The varying coating thickness might play a role in the tribological response of the coatings. However, as will be shown later, no such influence was detected.

4.3.2 Adhesion

Fig. 4.7 shows two images of Rockwell C hardness indents on a CrAlN coating with a Nb-content of 17 at.%. The ion etching time of the substrate was set to 15 minutes in Fig. 4.7 (a) and raised to 30 minutes for the coating in Fig. 4.7 (b). The idea of the Rockwell C indentation method for determining adhesion of the coating is that even under strong plastic deformation, the coating remains attached to the substrate, and in the side of the indentation, where tensile stresses are present, only few cracks are formed. The coating for which the ion etching time was set to 15 minutes shows a very strong delamination. The coating deposited after 30 minutes ion etching only shows small areas of delamination and a few cracks. Classified after the DIN adhesion table (see Fig. 3.12), the coating shown in Fig. 4.7 (a) has a coating adhesion of HF6, while the coating shown in Fig. 4.7 (b) has an improved adhesion of HF3. The adhesion of the other coatings shows no relevant difference to that in Fig. 4.7 and depends only on the different etching times of 15 or 30 minutes. Obviously, the duration of the ion etching pre-treatment is important for the development of the interface between coating and substrate, which is important for the adhesion of the coating. During the ion etching process, the substrate surface is cleaned from contaminated surface layers and modified by crystallographic changes of the substrate by the impinging argon ions [60].
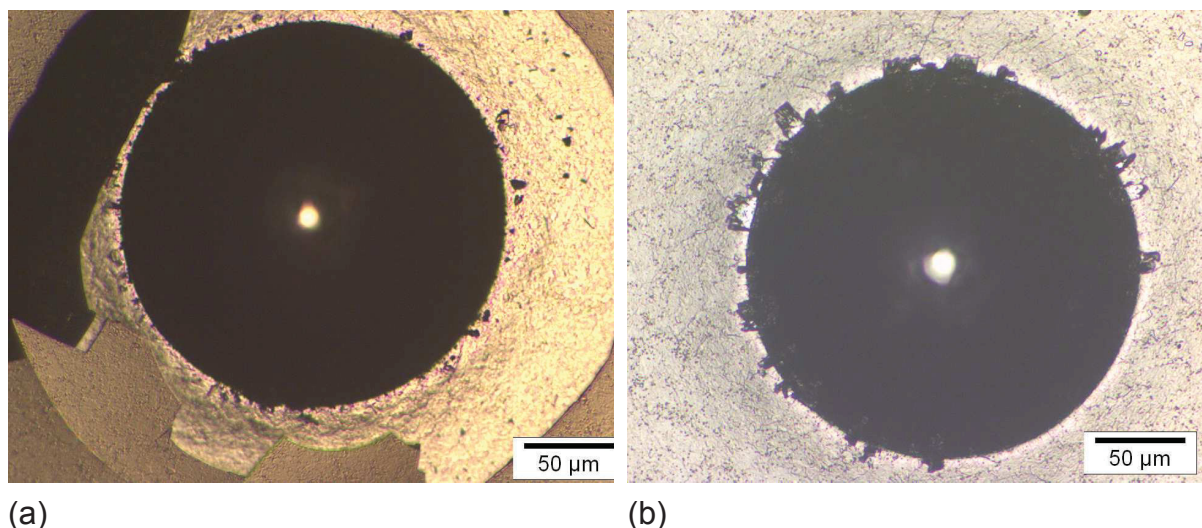
(a)   (b)

Fig. 4.7 Rockwell C indents on a CrAlN coating with 17 at.% Nb on HSS substrates (a) after an ion etching time of 15 minutes and (b) after an ion etching time of 30 minutes.

4.3.3 Roughness

The surface roughness values for the as-deposited state are shown in Fig. 4.8. All coatings display low roughness values. Due to the integration of foreign atoms in the CrN-matrix, the surface roughness should increase because of hindered growth of columnar crystals [20]. A remarkable enhancement of the surface roughness values is only observed in the CrAlN coating deposited at 500℃ and in the CrAlN-Re coatings. In the former case, this might be attributed to the formation of bigger columns at higher temperatures. Roughness tendencies in all other cases are difficult to explain. Roughness might play a role in the tribological testing of the coatings. However, as will be shown later, there seems to be no influence of coating roughness on the tribological response of the coatings.

4.3.4 Biaxial Residual Stresses

Fig. 4.9 (a) shows the biaxial stress temperature measurement (BSTM) curves for the CrN coating and the CrAlN coating deposited at 350°C. Both coatings show residual compressive stresses in the as-deposited state. While the CrN coating exhibits compressive stresses of -1000 MPa, the CrAlN coating shows compressive stresses of -150 MPa. Hence, the assembly of Al atoms in the CrN lattice seems to relieve stresses in the coating due to the open structure with more voids of the CrAlN coating deposited at 350℃.
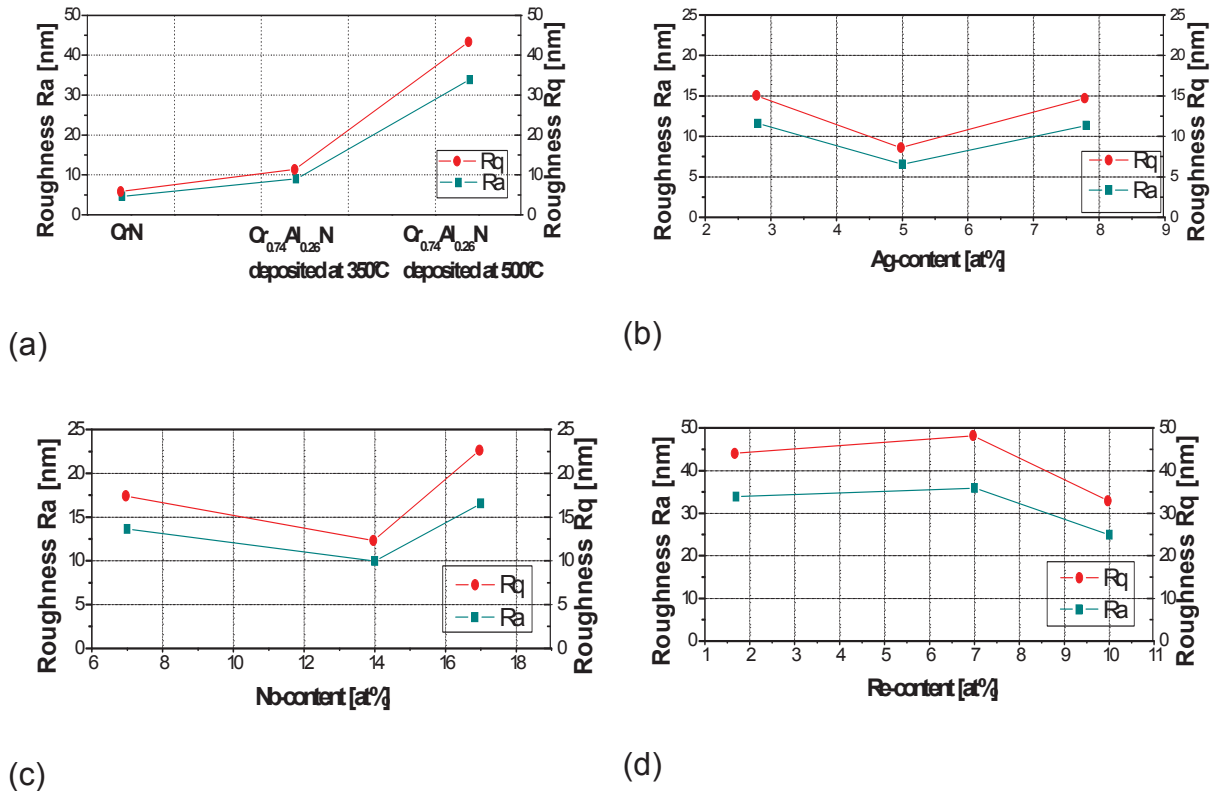
Fig. 4.8 Surface roughness Ra and Rq of (a) CrN and CrAlN coatings, (b) CrAlN coatings with different concentrations of Ag, (c) CrAlN coatings with different concentrations of Nb and (d) CrAlN coatings with different concentrations of Re on HSS substrate.

During heating, the compressive stresses of both coatings increase because of their higher thermal expansion coefficient compared to the substrate. The CrAlN coating shows a change of the slope of the BSTM curve at approximately 250℃ presumably due to defect annihilation, and thus, stress relaxation occurs. After reaching a zero stress level at 460℃, the coating exhibits tensile stresses of about 100 MPa at the maximum temperature of 500℃. The CrN coating shows a steeper slope of the BSTM curve during heating, and onset of recovery and thus stress relaxation can be observed between 150℃ and 400℃. Relaxation of com pressive stresses normally occurs slightly over deposition temperature [61]. In the case of the CrN and CrAlN coating, the onset of recovery starts about 100℃ a nd 200℃ below the deposition temperature, respectively. As will be shown later, stress relaxation in case of the other coatings starts beneath deposition temperature as well. It might thus be assumed, that the temperature in the deposition chamber is lower than the displayed 350℃.

The slope of the BSTM curve changes again for the CrN coating at approximately 400℃. Further heating results in a slight increase of the compressive stresses. This unexpected behaviour might be connected to the formation of at least a new phase in

the CrN coating. Fig. 4.10 shows the XRD patterns of the CrN coating before and after the stress temperature measurement. After the BSTM measurement, the additional formation of the Cr_2N phase can clearly be observed, but there are also some small peaks which can not be identified. During cooling, the BSTM curve of the CrN coating shows again linear elastic behaviour even though crack formation can be observed (Fig. 4.11 (a)). The BSTM curve of the CrAlN coating shows a dissimilar behaviour. During cooling, the tensile stresses decrease, presumably due to the formation of cracks in the coating (see Fig. 4.11 (b)). In this case no phase transformation or decomposition was observed.

In Fig. 4.9 (b), residual stresses within the CrAlN-Ag coatings in the as-deposited state and their thermal evolution are shown. Both coatings exhibit residual compressive stresses. While the coating with 2.8 at.% Ag shows compressive stresses of -440 MPa, the coating with 7.8 at.% Ag shows compressive stresses of 220 MPa. Therefore, it seems that the incorporation of Ag reduces the compressive stresses in the coatings as soon as sufficient Ag is provided. This confirms the observations made in the XRD measurements (Fig. 4.4). During heating, the compressive stresses increase as explained before. For the coating with 2.8 at.% Ag, the slope of the BSTM curve slightly changes above approximately 75℃. It is possible that the soft Ag phase which is embedded in the coating already underlies plastic deformation. A second change in the slope of the curve occurs at about 150℃, where the stresses remain more or less const ant with increasing temperature. Finally, at temperatures between 250℃ and 500℃ co mpressive stresses decrease with increasing temperature. For the coating with 7.8 at.% Ag, there seems to be a change in the slope of the BSTM curve also at approximately 75℃. After that, compressive stresses increase slightly with increasing temperature up to 250℃. After that temperature, compressive stresses decrease with increasing temperature, reaching about -100 MPa at maximum temperature. Again, stress relaxation due to defect annihilation should be the reason for the change in the slope at temperatures above 250℃. During cooling, both BSTM curves show linear thermoelastic behaviour until approximately 350℃. The difference in the sl opes could be connected to differences in the mechanical properties of the coatings [62]. Afterwards, the formation of cracks governs the BSTM curves (see Fig. 4.11 (c)).
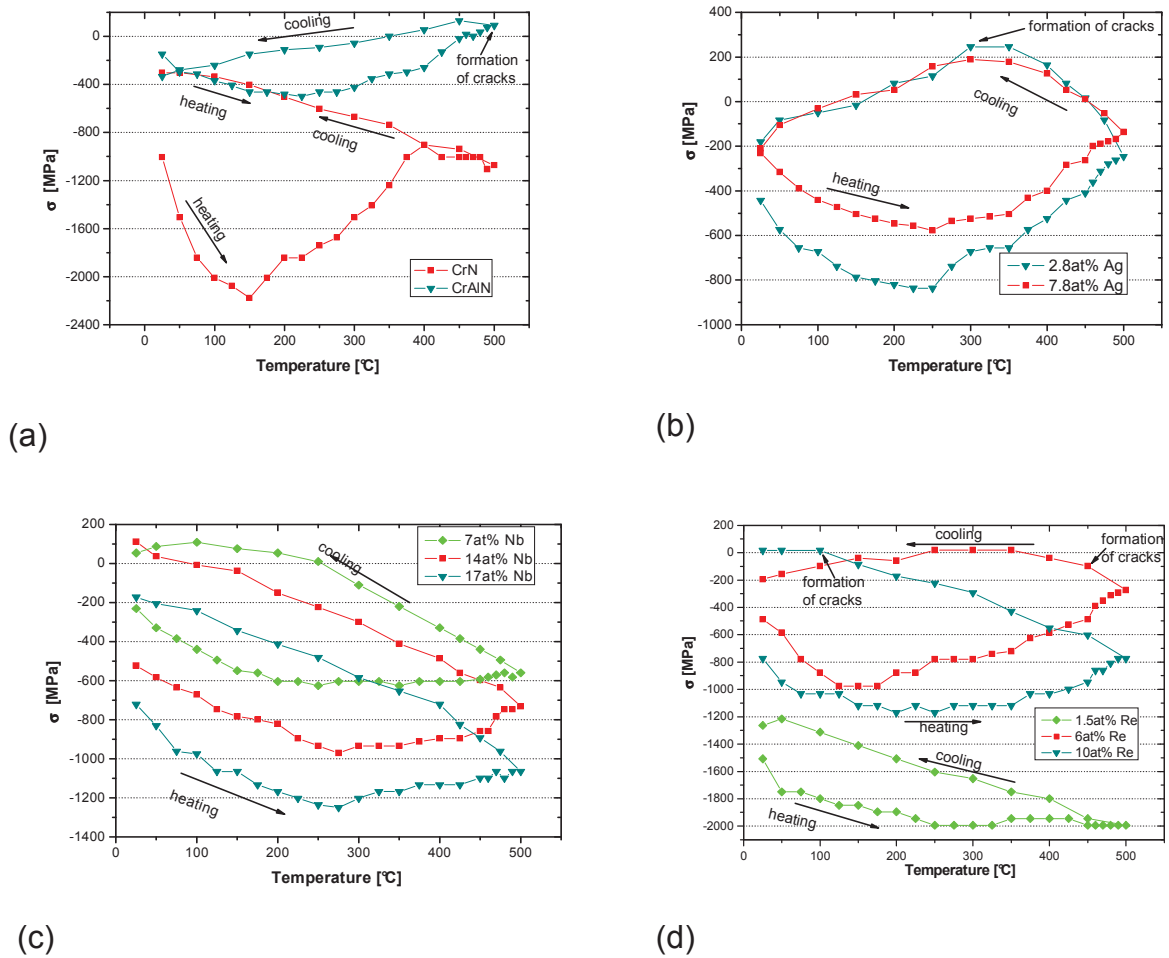
Fig. 4.9 Stress-temperature cycles of (a) CrN and CrAlN coatings, (b) CrAlN coatings with different concentrations of Ag, (c) CrAlN coatings with different concentrations of Nb and (d) different concentrations of Re on silicon substrate.

Fig. 4.9 (c) shows residual stresses within the CrAlN-Nb coatings and their thermal evolution. All coatings show residual compressive stresses ranging from -240 to -720 MPa in the as-deposited state. Higher Nb-contents result in higher compressive stresses, as was already shown in the XRD measurements (cf. chapter 4.2.3, Fig. 4.5). During heating, the compressive stresses increase as explained before. A further increase of the temperature results in a change of the slopes of the BSTM curves. The coating with 7 at.% Nb shows constant compressive stresses at approximately -600 MPa from 200℃ up to 500℃. In c ase of the coatings with 14 at.% and 17 at.%, there is only a slight decrease of compressive stresses from approximately 275℃ up to 500℃. The sample with 17 at.% Nb shows first a steeper slope than the coating with 14 at. %, but the latter shows a stronger decrease of stresses between 450 and 500℃. The change in the s lope during heating is a sign of stress relaxation due to defect annihilation in all three cases. It seems that the

increasing amount of a second phase (presumably ε-Nb, cf. chapter 4.2.3) has an influence in the relaxation behaviour.

During cooling, the stress temperature curves of the CrAlN coatings with 14 and 17 at.% Nb show again linear thermolelastic behaviour with similar slopes of the stress temperature curves. The CrAlN coating with 7 at.% Nb shows the same behaviour until approximately 250℃. Afterwards, it seems lik e crack formation affects the BSTM curve. However, no cracks could be observed in the light optical micrograph. It might be that the change in the slope in the BSTM curve results from plastic deformation of the coating or from cracks within the material or starting at the interface that did not grow up to the surface.

Fig. 4.9 (d) shows BSTM curves for CrAlN coatings with different concentrations of Re. All coatings show residual compressive stresses ranging from -490 to -1500 MPa. The CrAlN coating with 1.5 at.% Re exhibits the highest compressive stresses due to its single phase structure with Re atoms dissolved in the CrAlN matrix as shown in Fig. 4.6. The CrAlN coating with 6 at.% Re shows the lowest compressive stresses, which might be a result of the formation of an additional Re phase and subsequent stress relaxation in the coating (see Fig. 4.6). The compressive stresses of the CrAlN coating with 10 at.% Re lie in between. Due to the increasing amount of the additional Re phase, the residual stresses might increase again.

During heating, the compressive stresses of the coating with the lowest Re-content increase until a temperature of 250℃ is reached. T he compressive stresses remain then constant at approximately -2000 MPa from 250° up to 500℃. Here, again, relaxation should take place. The coating with 6 at.% Re shows a decrease in compressive stresses from approximately 150℃ up to 500℃. The coating with 10 at.% Re shows constant compressive stresses at approximately -1180 MPa from 150℃ to 350℃. After that, compressive stresses de crease with increasing temperature. In this case, as a dual phase structure is present, not only relaxation by defect annihilation should play a role in the stress-temperature behaviour, but also plastic deformation of the metallic phase in the coating. During cooling, the BSTM curve of the CrAlN coating with 6 at.% Re shows linear thermoelastic behaviour until approximately 450℃. The BSTM curves of the CrAlN c oating with 1.5 at.% Re and 10 at.% Re shows similar linear thermoelastic behaviour until approximately 50℃ and 100℃, respectively. Afterwards, the formation of cracks governs the BSTM curves in all three coatings (see Fig. 4.11 (d)).
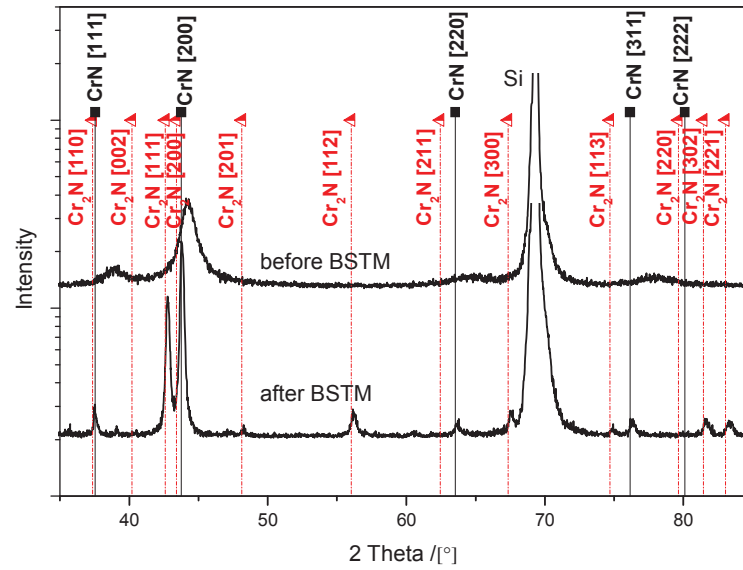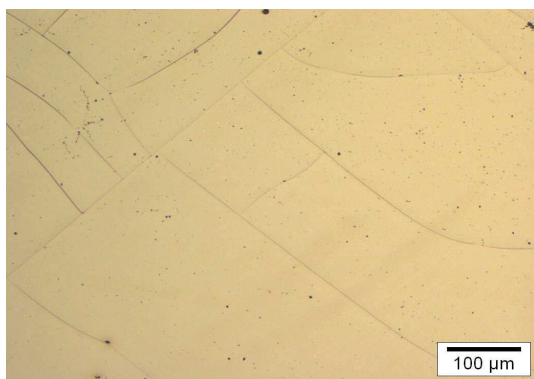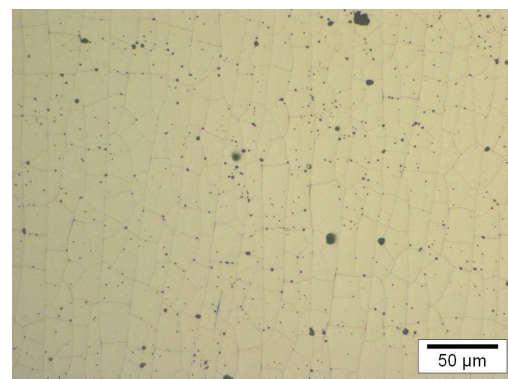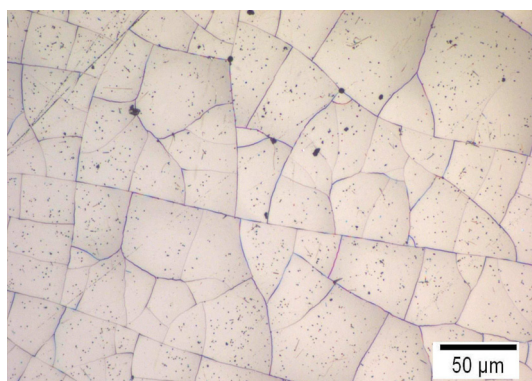
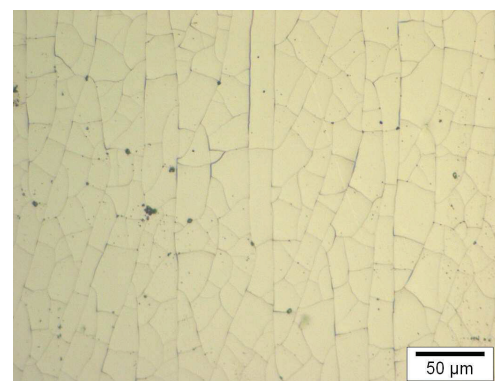**Fig. 4.10** XRD-patterns of the CrN coating deposited on silicon substrates before and after BSTM.

Fig. 4.11 Light optical micrographs of (a) CrN coating, (b) CrAlN coating, (c) CrAlN coating with 7.8 at.% Ag and (d) CrAlN coating with 6 at.% Re after BSTM.

4.3.5 Hardness and Elastic Modulus

The hardness (H) and the elastic modulus (E) of the coatings were determined on samples deposited on HSS substrates. Fig. 4.12 (a) shows the film hardness and the elastic modulus of the CrN coating and the CrAlN coatings. The values for the CrN reference coating are H=17.7 GPa and E=316 GPa. It is known that the hardness and elastic modulus of CrAlN coatings compared to CrN coatings increase with increasing Al-content in the coating. The reason for this is the substitution of Cr atoms by Al atoms in the CrN lattice which leads to solid solution hardening [1, 63]. This behaviour cannot be observed for the CrAlN coating deposited at 350℃, which shows lower values than the CrN coating (H=14.9 GPa and E=311 GPa). The CrAlN coating deposited at 500℃, however, displays highe r values (H=23.6 GPa, E=388 GPa). The difference between the obtained hardness and elastic modulus values for the CrAlN coatings in this work might be related to the different deposition temperatures and its effect in the structure of the coating, i.e., at higher temperatures less voids and a more dense structure are present.

Fig. 4.12 (b) shows the film hardness and elastic modulus of the CrAlN coatings with rising Ag-content. The hardness as well as the elastic modulus decrease with increasing Ag-content. The coatings show hardness values in the range of 14.8 to 13.1 GPa and elastic modulus values ranging from 287 GPa to 277 GPa. The same tendency, but with lower values for the elastic modulus and higher values for the hardness, has been reported before [64]. The difference between the measured values and the literature data might be connected with slightly different deposition parameters. Ag forms a very soft, metallic phase with a fcc crystal structure. As shown in Fig. 4.4, increasing the Ag-content leads to the formation of a dual phase structure in the coating with the fcc Ag-phase embedded in the CrAlN matrix. Therefore, film hardness and elastic modulus decrease.

The hardness and the elastic modulus of the CrAlN-Nb coatings are shown in Fig. 4.12 (c). The coating hardness and the elastic modulus steadily increase with increasing Nb-content. The values of hardness and elastic modulus of the CrAlN coating with the highest Nb content (H=27.8 GPa, E=395 GPa) are the highest measured values of all coatings. As shown in Fig. 4.5, the formation of the ε-NbN phase is not observed until a Nb-content of 14 at.% is reached. At lower Nb-contents, the Nb atoms are presumably dissolved in the CrAlN matrix. Therefore, the slightly raised values of hardness and elastic modulus compared to the CrN and CrAlN coatings deposited at 350℃ might be attributed to solid solution hardening. At higher Nb-contents, a dual phase structure has been detected. Besides the CrAlN matrix, the hexagonal ε-NbN phase forms. Due to its hexagonal crystal structure, the ε-NbN phase is a very hard phase. Therefore, film hardness and elastic modulus increase.

Fig. 4.12 (d) shows hardness and elastic modulus of the CrAlN-Re coatings. The hardness and the elastic modulus increase with increasing Re-content. For the coating with a Re-content of 1.5 at.% (H=15.5 GPa, E=320 GPa), the values are in the range of the CrN and CrAlN coatings deposited at 350℃. As shown in Fig. 4.6, this coating exhibits a single-phase structure with Re atoms dissolved in the CrAlN-matrix, which leads again to solid solution hardening. At higher Re-contents, the formation of an additional phase, namely metallic Re, is observed (see Fig. 4.6). Normally, hardness should decrease when a metallic phase is embedded in the CrAlN matrix, as it is the case for CrAlN-Ag. However, Re has a hexagonal crystal structure. This makes dislocation sliding difficult, and hence, hardness increases.
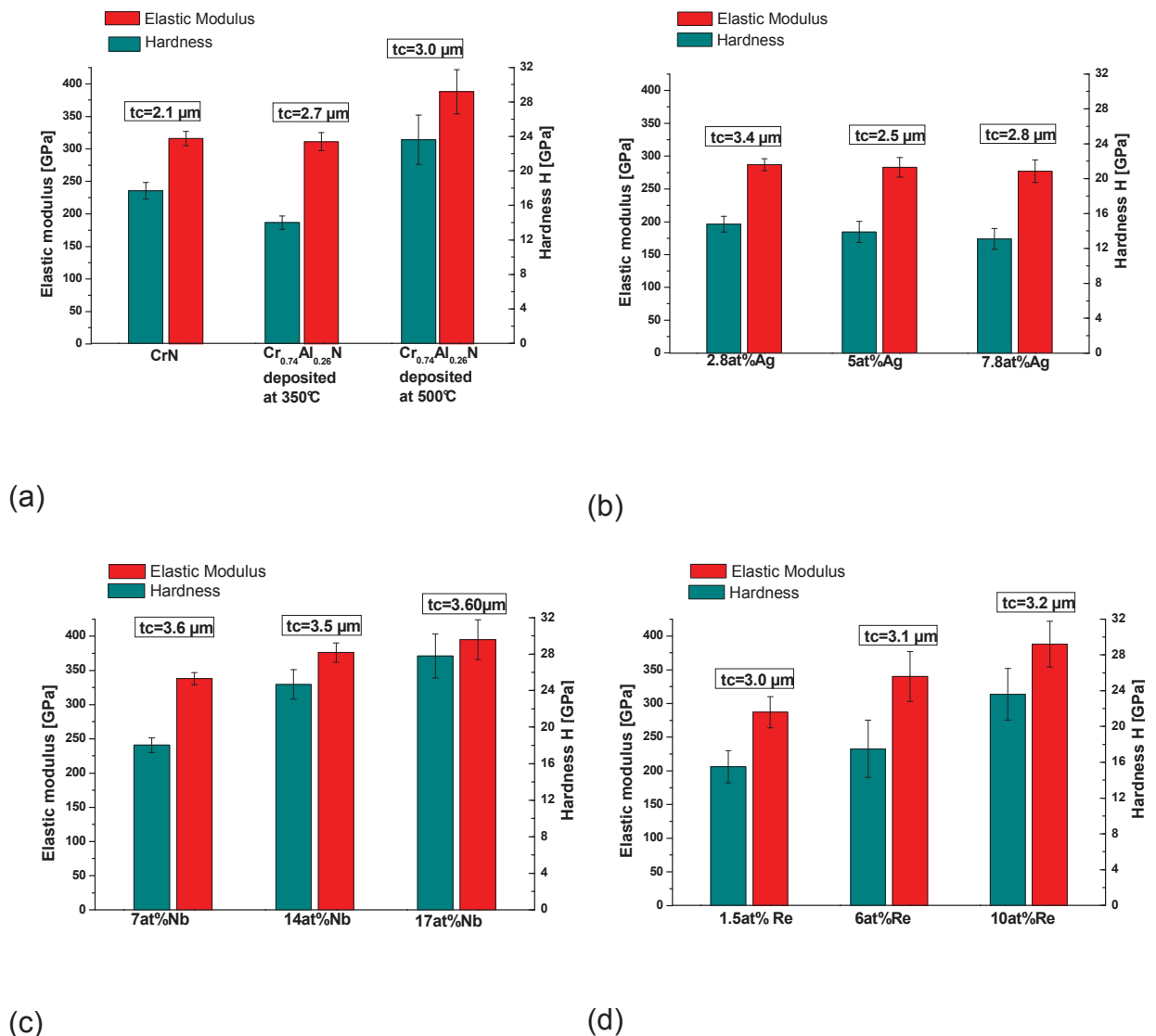

(a)

(b)

(c)

(d)

Fig. 4.12 Hardness and elastic modulus of (a) CrN and CrAlN coatings, (b) CrAlN coatings with different concentrations of Ag, (c) CrAlN coatings with different concentrations of Nb and (d) CrAlN coatings with different concentrations of Re on HSS substrates.

4.4 Electrical Properties

The electrical resistance (ρ) of coatings deposited on silicon substrates was measured by the previously described technique (see chapter 3.2.6). Fig. 4.13 shows the electrical resistance of all coating systems. The measured values demonstrate that the electrical resistance of the silicon substrate is significantly higher (ρ ~7×10^{-2} Ωm), which is a requirement of this measurement technique to obtain proper results. Measurements on HSS substrates failed due to the not sufficient large difference in the electrical resistance of coating and substrate.

The CrAlN coating exhibits an electrical resistance of ρ=5.5×10^{-4} Ωm. Compared to literature data, this value is relatively low [65]. A reason for this may be the slightly different deposition parameters and also the different measurement method (Van der Pauw method) used in [65] for the electrical resistance. The electrical resistance of the CrAlN-Nb coatings decreases with increasing Nb-content, ranging from ~10^{-5} to ~10^{-6} Ωm. The CrAlN coating with the highest Nb-content shows the lowest electrical resistance of all measured coatings. The electrical resistance of the CrAlN-Re coatings also decreases with increasing Re-content. The CrAlN-Ag coatings show the same tendency with increasing Ag content, but the electrical resistance ranges from ~10^{-3} to ~10^{-5} Ωm. Apart from the CrAlN coating with 2.8 at.% Ag, all alloyed CrAlN coatings exhibit an obviously lower electrical resistance than the CrAlN coating. On that account, the measured value of the CrAlN-Ag coating (ρ=1.4×10^{-3} Ωm) seems to be relatively high.

Elemental Ag has the lowest electrical resistance of all metals [66]. Therefore, the lower electrical resistance of the CrAlN coating with 7.8 at.% Ag compared to the CrAlN coating might be explained by the formation of Ag as a continuously distributed second phase in the coating. For the CrAlN-Ag coating with 2.8 at.% Ag, the Ag-content might be too low to form a continuous second phase and therefore, the electrical resistance is higher compared to CrN. ε-NbN and elemental Re have a lower electrical resistance as the CrAlN coating [67, 68]. On account of this, the formation of both phases in the corresponding coatings may reduce the electrical resistance as well.
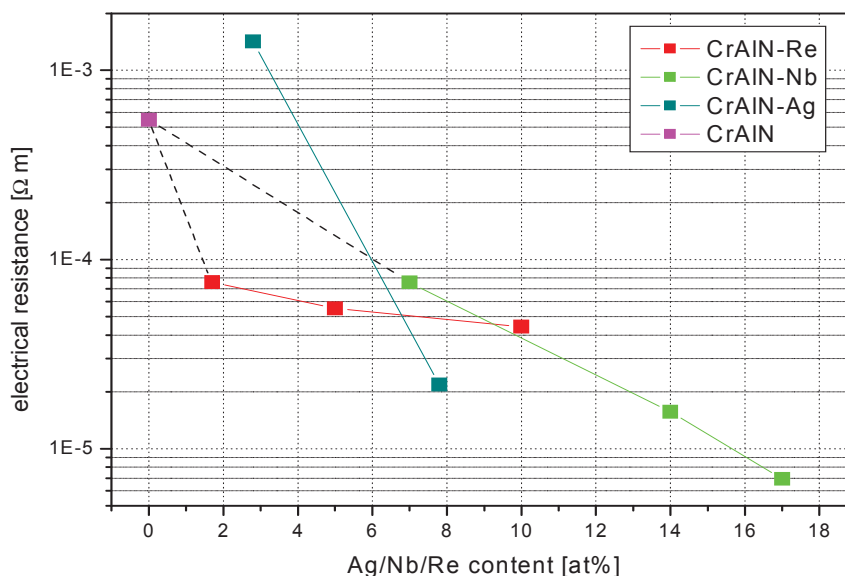
Fig. 4.13 Electrical resistance of the various coating systems measured on silicon substrates.

4.5 Tribological Properties

The coefficients of friction as a function of sliding distance obtained from tribological testing of CrN and CrAlN samples against Al_2O_3 balls at room temperature and 200℃ are shown in Fig. 4.14.

At room temperature, the CrN sample shows a steady-state coefficient of friction of approximately 0.5 which is reached after a running-in period of approximately 12 m. The CrAlN sample deposited at 350℃ shows similar f riction behaviour, but much more pronounced data scattering. After approximately 40 m, steady-state friction with a coefficient of friction in the range of 0.5 was obtained. The CrAlN sample deposited at 500℃ shows an initial friction coefficient of 0 .2, followed by continuous increasing of the friction coefficient up to 0.4.

At 200℃, the CrN sample shows a steady-state coeff icient of friction of approximately 0.7 after a running-in distance of 5 m. After 65 m sliding distance, a significantly higher scattering of the friction curve occurs. This might indicate coating failure. For the CrAlN sample deposited at 350℃, t he experiment starts with a coefficient of friction of 0.6. Afterwards, the coefficient of friction increases slightly and reaches a steady-state value of approximately 0.8. After 79 m sliding distance, a drop in the friction curve occurs. After this, the friction coefficient increases again and reaches a value below the previous coefficient of friction (approximately 0.7). The drop in the friction coefficient should not be relevant, and it might be connected to a

singular sliding event, like a big freely rotating wear particle remaining in the contact for several revolutions. For the CrAlN sample deposited at 500℃, the experiment starts with a low initial coefficient of friction of about 0.2. After a short running-in period, the coefficient of friction increases up to 0.6. After 19 m of sliding, a drop in the friction curve can be observed. This might again be connected to a singular sliding event. Such sudden drops in the coefficient of friction appear also during testing of some other samples as will be shown later.
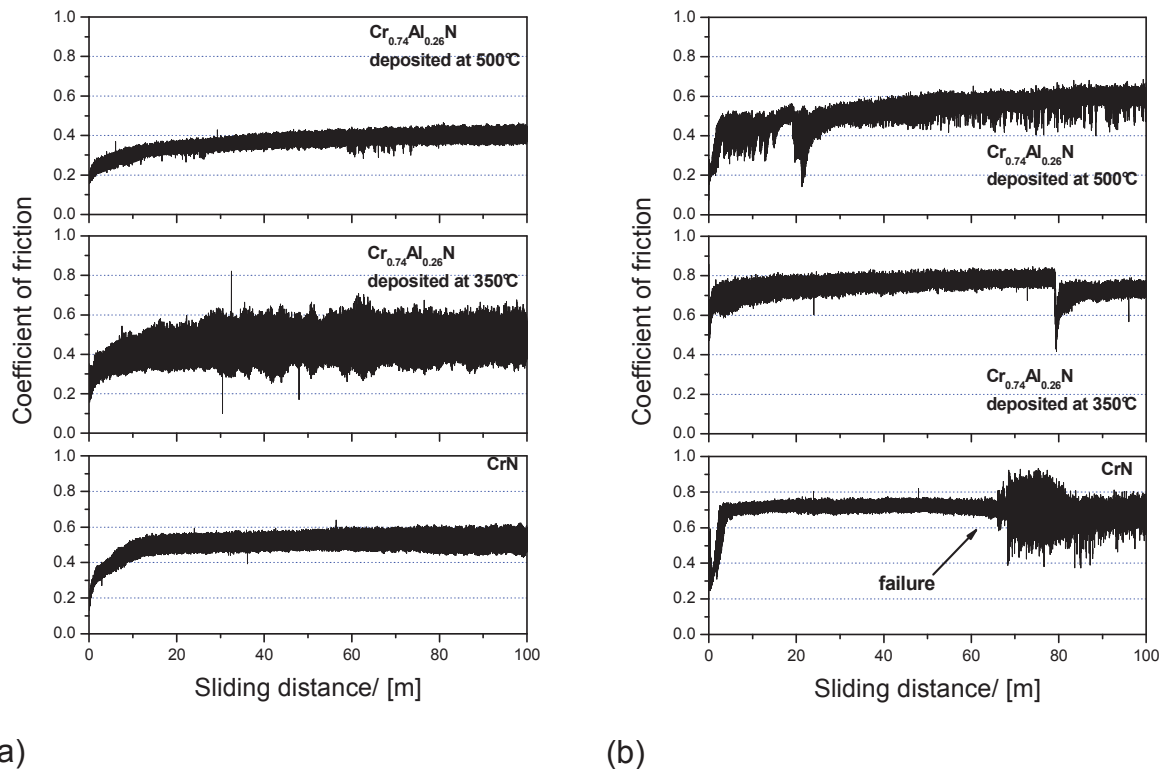

(a)   (b)

Fig. 4.14 Evolution of the coefficient of friction over a sliding distance of 100 m for CrN and CrAlN coatings tested at (a) room temperature and (b) 200℃ against alumina.

The 3D surface profiles of the tested samples were obtained using an optical profilometer. Fig. 4.15 (a-c) shows the surfaces of the CrN and the CrAlN samples after testing at room temperature. No wear tracks can be detected. Therefore, the actual depth of the wear tracks is in the order of the surface roughness. The CrN sample tested at 200℃ shows a wear track which is deeper than the coating thickness (see Fig. 4.16 (a)). Hence, the supposed coating failure can be verified. As shown in Fig. 4.16 (b) and Fig. 4.16 (c), the surfaces of the CrAlN sample tested at 200℃ show no visible wear tracks. The depth of the wear track seems to be as well

At room temperature, a slight reduction in the friction coefficient compared to CrN can only be observed for the CrAlN coating deposited at 500℃. Higher surface

roughness as well as higher hardness of the coating (cf.chapter 4.3.3 and 4.3.5) reduce the contact area [36] which might be the reason for the reduction of the friction coefficient. All coatings show very good wear behaviour. At elevated temperature, the friction coefficient of the CrAlN coating deposited at 350℃ is slightly higher compared to CrN. The friction coefficient of the CrAlN coating deposited at 500℃ is again lower compared to CrN which has the same reasons as mentioned above. While the CrN coating is clearly worn through at 200℃, the CrAlN coatings show no detectable wear. The improved wear behaviour of the CrAlN coatings at elevated temperatures can be related to the higher oxidation resistance compared to CrN [1]. Besides the oxidation resistance, the increased hardness of the CrAlN coating deposited at 500℃ compared to the CrN coat ing may contribute to the better wear behaviour, as well. It can thus be concluded that alloying CrN with 25%Al yields to a higher oxidation resistance and better wear behaviour at elevated temperatures. in the range of the surface roughness.
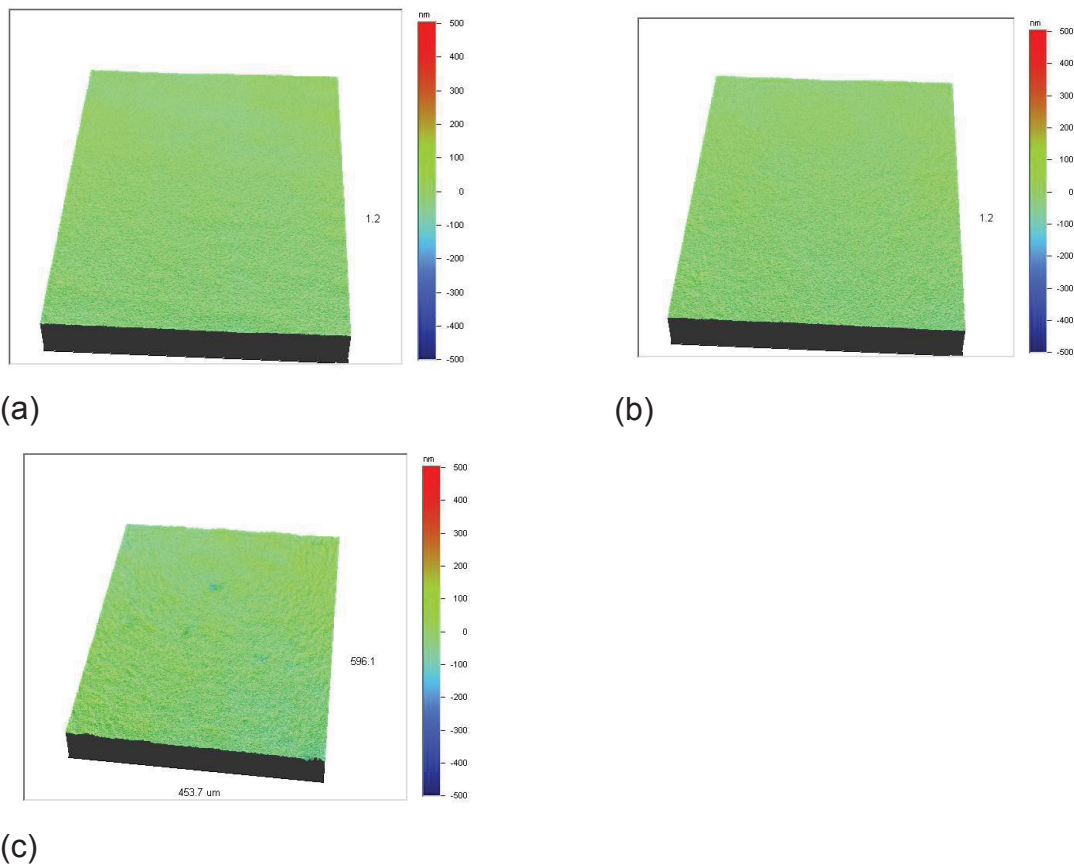

(a)

(b)

(c)

Fig. 4.15 3D-surface profiles of a (a) CrN coating, (b) CrAlN coating deposited at 350℃ and (c) CrAlN coating deposited at 500℃ afte r a sliding distance of 100 m at room temperature.
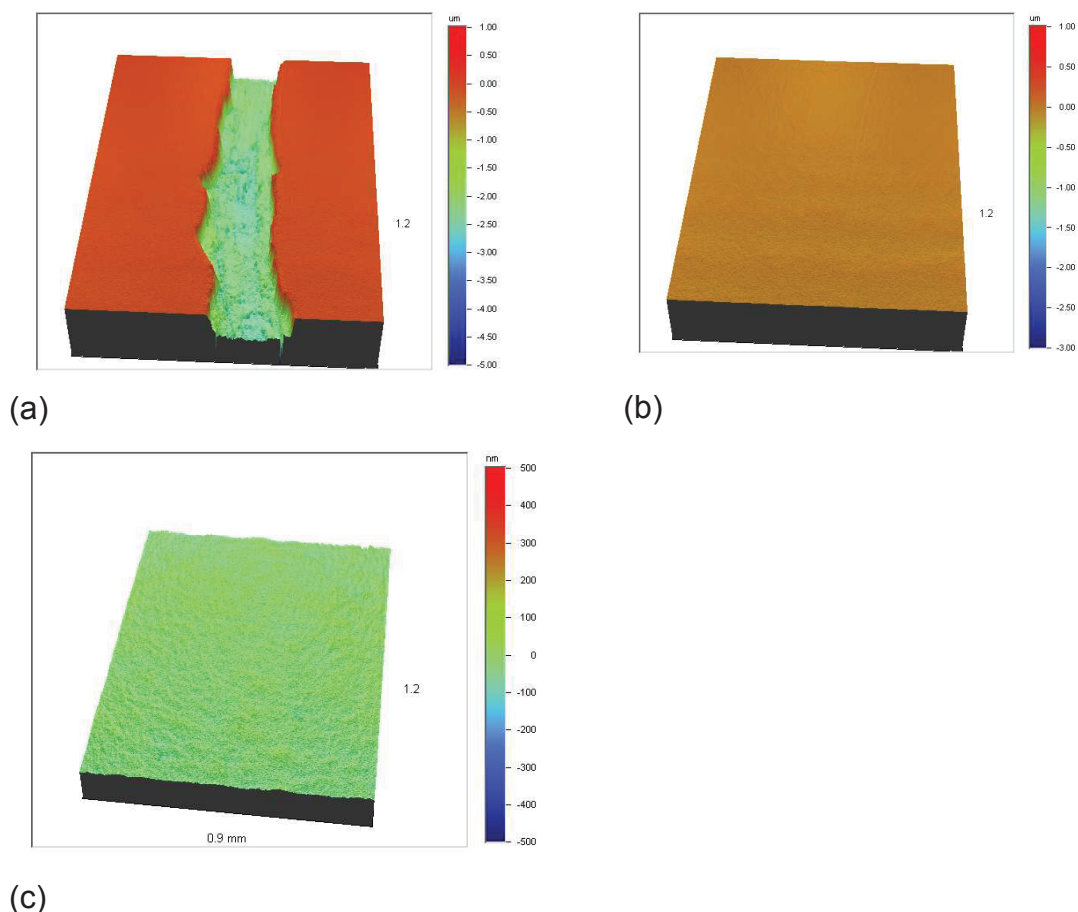
(a)

(b)

(c)

Fig. 4.16 3D-surface profile a (a) CrN coating, (b) CrAlN coating deposited at 350℃ and (c) CrAlN coating deposited at 500℃ after a sl iding distance of 100 m at 200℃.

The friction curves of tribological testing of CrAlN-Ag samples against Al_2O_3 balls at room temperature and 200℃ are shown in Fig. 4.17. Additionally the friction curves of the reference CrN sample are also shown in Fig. 4.17.

At room temperature, the coefficient of friction starts at a value of approximately 0.2 for all coatings. After a short running-in period, the friction coefficient of the CrAlN sample with 2.8 at.% Ag increases during the experiment until a value of approximately 0.5 is reached. The CrAlN samples with 5 and 7.8 at.% Ag show a steady-state friction with a coefficient of friction of approximately 0.6 after a short running-in period.

At 200℃, the CrAlN sample with 2.8 at.% Ag starts with a coefficient of friction of approximately 0.2. After a short running-in period, a steady-state friction with a value of approximately 0.5 is reached. The CrAlN sample with 5 at.% Ag shows a slightly higher initial coefficient of friction and reaches again a steady-state coefficient of friction of approximately 0.5 after a running-in period of approximately 50 m. For the CrAlN sample with 7.8 at.% Ag, a steady-state coefficient of friction of approximately 0.6 is reached after a short running-in period.
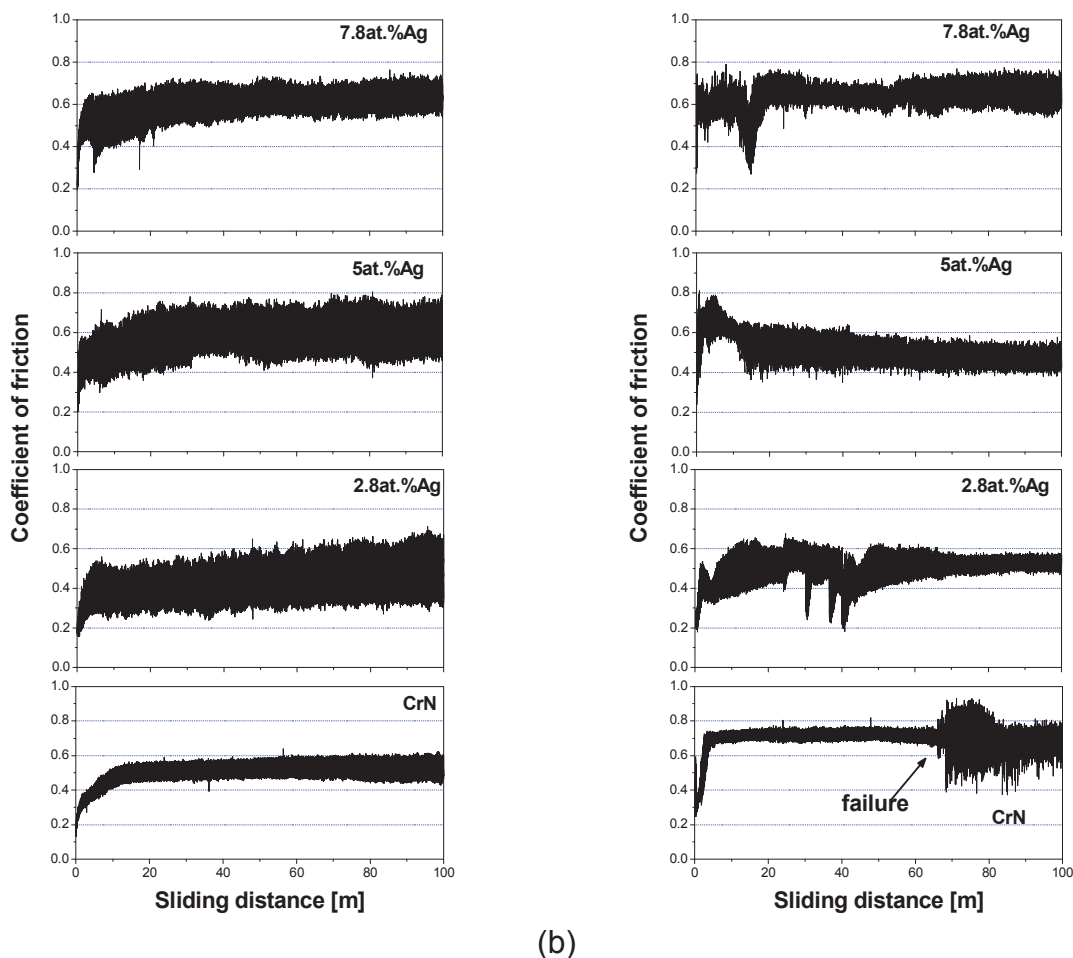
(a)   (b)

Fig. 4.17 Evolution of the coefficient of friction over a sliding distance of 100 m for CrN and CrAlN coatings with different concentrations of Ag tested at (a) room temperature and (b) 200℃ against alumina.

Fig. 4.18 - Fig. 4.20 show 3D-surface profiles of the CrAlN-Ag samples after testing at room temperature and 200℃. In Fig. 4.18 (a), a wear track is clearly visible, but the depth of the wear track is below the coating thickness. The other samples tested at room temperature show similar wear behaviour, whereas the wear increases with increasing Ag-content. Fig. 4.18 (b) shows the wear profile for the CrAlN sample with 2.8 at.% Ag tested at 200℃. The observed wear track is slightly broader, but the depth is lower than that of the room temperature sample. Again, wear increases with increasing Ag-content. The high wear of the CrAlN sample with the highest Ag-content might be connected with adhesion problems, too.

(a)   (b)

Fig. 4.18 3D-wear profiles of CrAlN-Ag coatings with 2.8 at.% Ag after a sliding distance of 100 m at (a) room temperature and (b) 200℃.

(a)   (b)

Fig. 4.19 3D-wear profiles of CrAlN-Ag coatings with 5 at.% Ag after a sliding distance of 100 m at (a) room temperature and (b) 200℃.

(a)   (b)

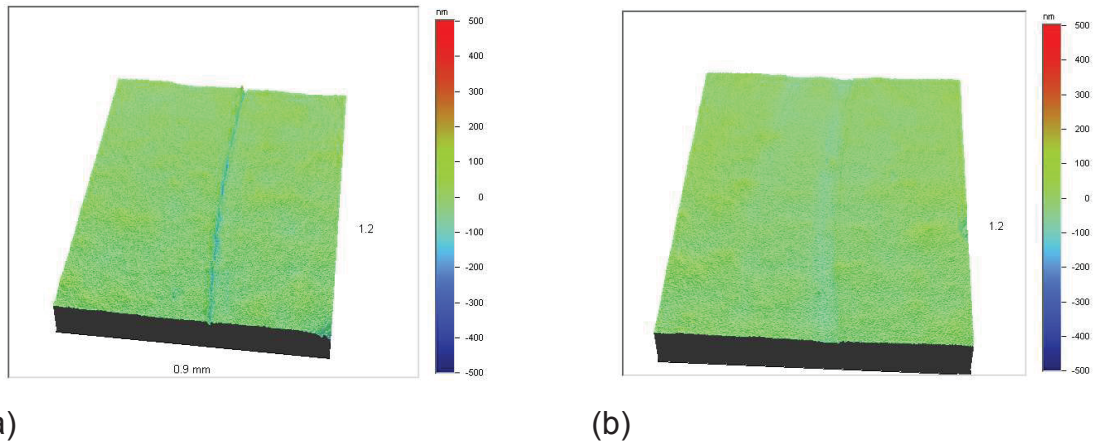**Fig. 4.20** 3D-wear profiles of CrAlN-Ag coatings with 7.8 at.% Ag after a sliding distance of 100 m at (a) room temperature and (b) 200℃.

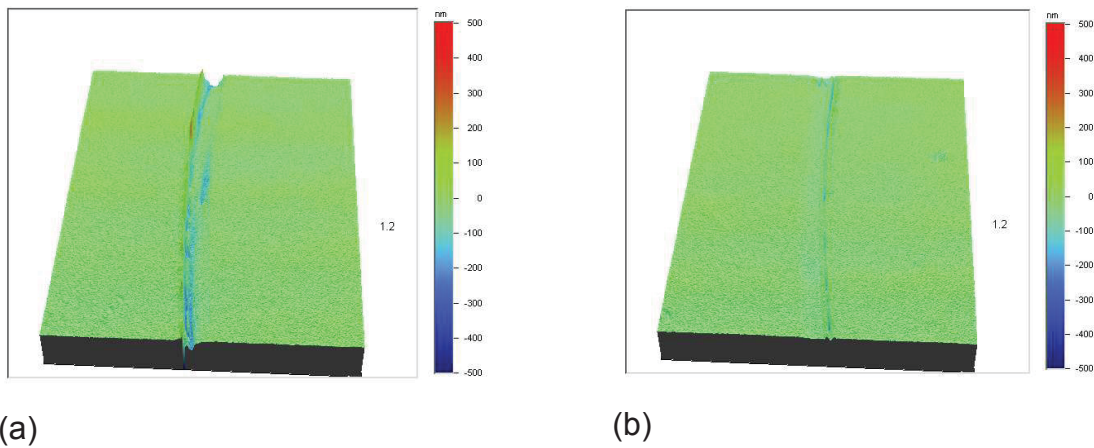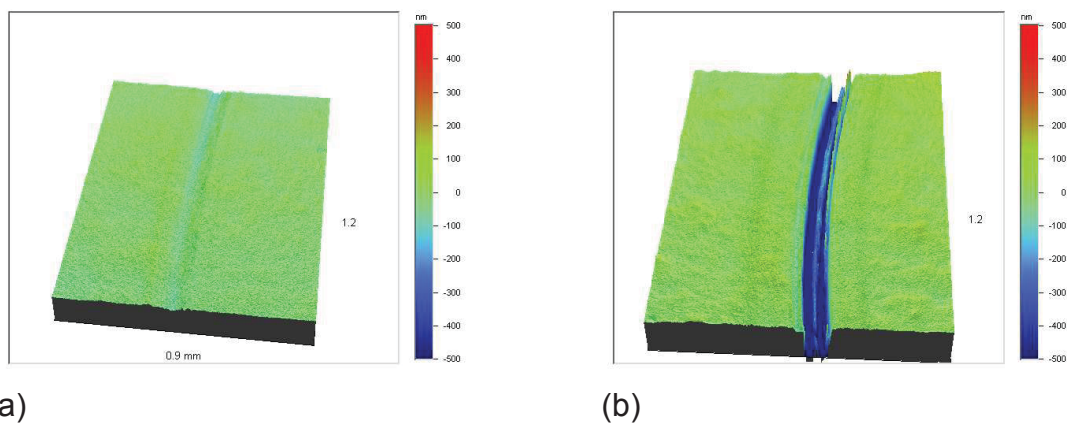In comparison to CrN, all CrAlN-Ag samples show slightly higher friction and wear at room temperature, but better tribological behaviour at elevated temperatures. The

CrAlN-Ag coatings show lower hardness values compared to CrN whereas increasing the Ag-content lowers the hardness of the coatings (cf. chapter 4.3.5). It might be possible that the real area of contact increases due to the drop in hardness, and thus, friction increases with increasing Ag content at room temperature. Since abrasion seems to be the main mechanism of wear, wear increases as well due to the drop in hardness. As reported in [3], the incorporation of ≥ 12 at.% Ag in CrN coatings results in solid lubricant surface layers which decrease friction and wear at room temperature and elevated temperatures . In the present work, however, the Ag-content might be to low to form effective surface layers. Nevertheless, diffusion of Ag to the surface at 200℃, and thus the presence of s mall amounts of this metal in the area of contact, is possible, and might be the reason for the observed slight decrease in friction.

Fig. 4.21 shows the coefficient of friction as function of sliding distance for the CrAlN-Nb samples when sliding against Al_2O_3 balls at room temperature and 200℃. The friction curves of the CrN sample are also shown and used as a reference.

At room temperature, all CrAlN-Nb samples show similar friction behaviour. The CrAlN sample with 7 at.% Nb shows a steady-state coefficient of friction of approximately 0.5 after a running-in period of 30 m. The CrAlN sample with 14 at.% Nb reaches a steady-state coefficient of friction slightly below 0.6 after a running-in period of approximately 25 m. For the CrAlN sample with 17 at.%Nb, a steady-state coefficient of friction slightly above 0.6 is reached after a running-in period of 20 m.

At 200℃, all CrAlN-Nb samples show again similar f riction behaviour. The friction coefficient starts at a value of approximately 0.2 for all coatings. All coatings reach a coefficient of friction of approximately 0.7 in the end of the experiment.

Fig. 4.22 - Fig. 4.24 show 3D-surface profiles of the CrAlN-Nb samples at room temperature and 200℃. In Fig. 4.22 (a) and Fig .4. 22 (b), wear tracks are visible, but the wear track depths are slightly above the surface roughness. Fig. 4.23 shows the wear profiles for the CrAlN-Nb samples with 14 at.% Nb. Both samples show clearly visible wear tracks, with depths around 300 nm. The same behaviour is observed for the CrAlN-Nb sample with 17 at.% Nb tested at room temperature (see Fig. 4.24 (a)), where the coating tested at 200℃ (see Fig. 4.24 (b)) shows lower wear.

(a)   (b)

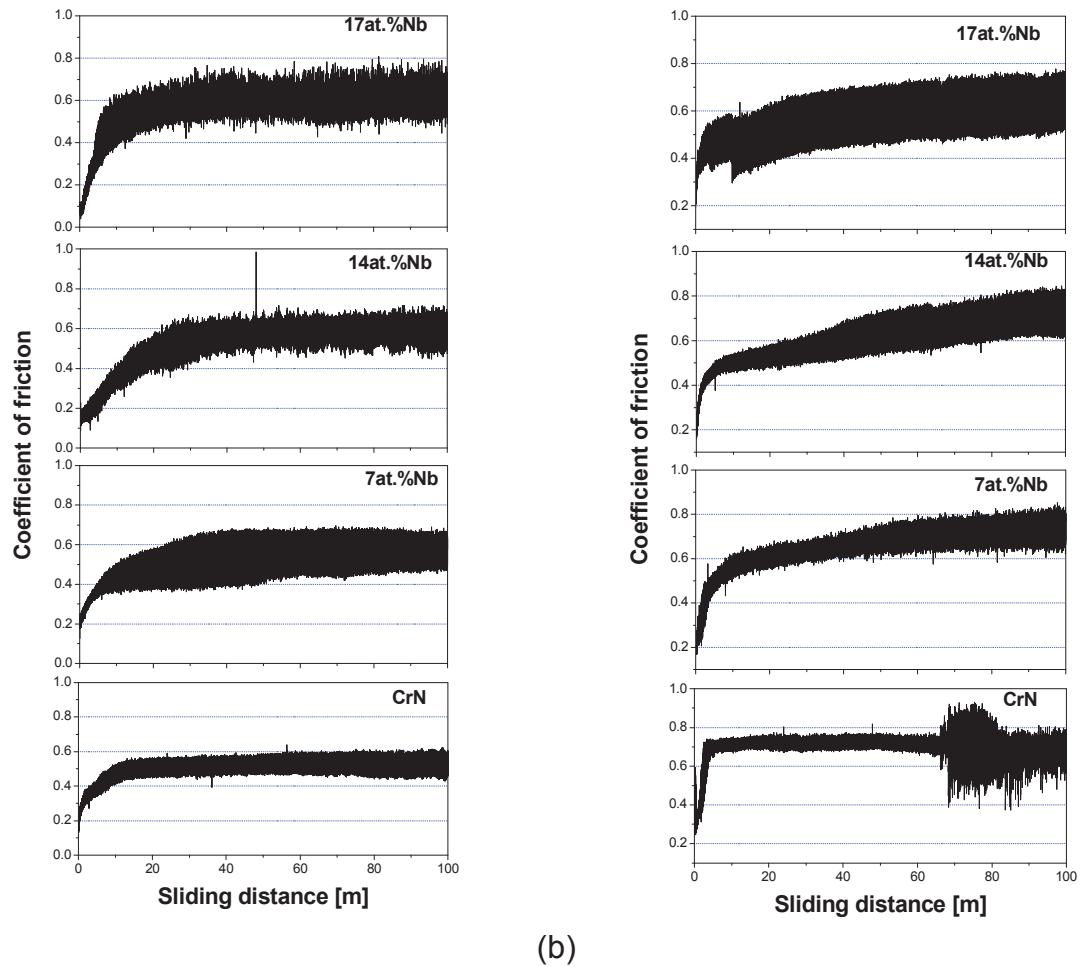**Fig. 4.21** Evolution of the coefficient of friction over a sliding distance of 100 m for CrN and CrAlN coatings with different concentrations of Nb tested at (a) room temperature and (b) 200℃ against alumina.
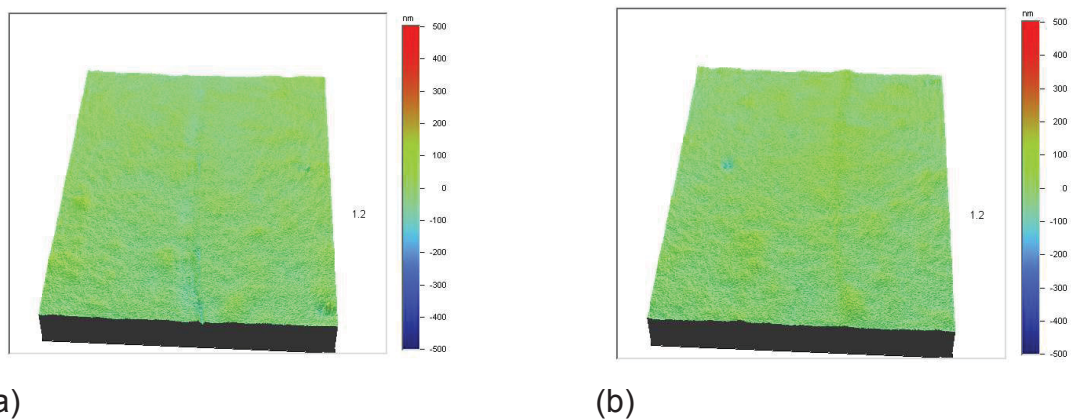

(a)   (b)

Fig. 4.22 3D-wear profiles of CrAlN-Nb coatings with 7 at.% Nb after a sliding distance of 100 m at (a) room temperature and (b) 200℃.

(a)   (b)

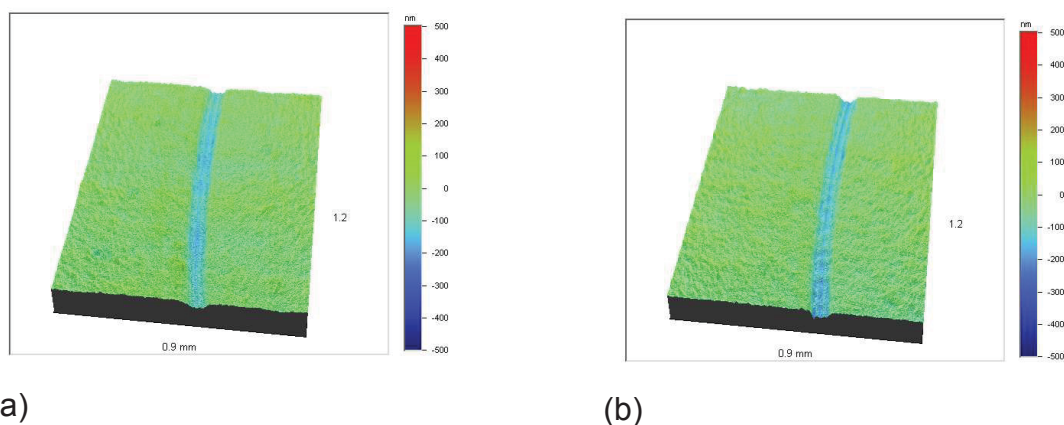**Fig. 4.23** 3D-wear profiles of CrAlN-Nb coatings with 14 at.% Nb after a sliding distance of 100 m at (a) room temperature and (b) 200℃.

(a)   (b)
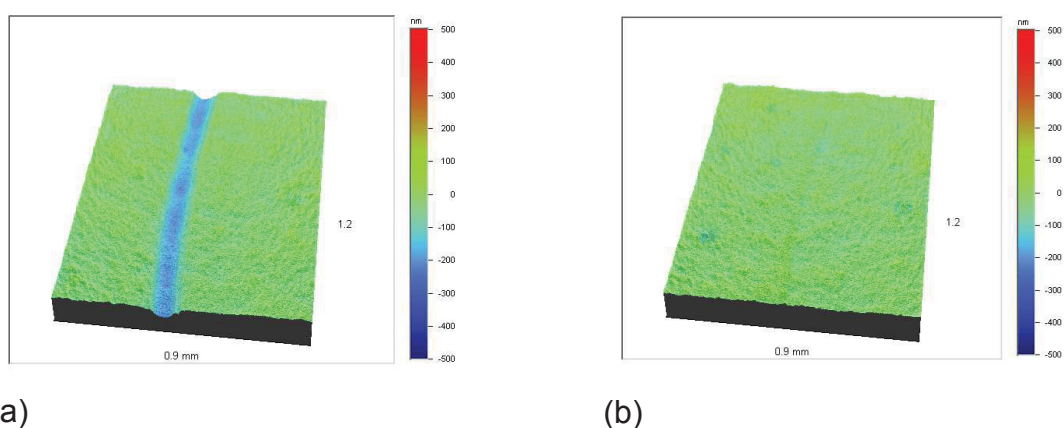
Fig. 4.24 3D-wear profiles of CrAlN-Nb coatings with 17 at.% Nb after a sliding distance of 100 m at (a) room temperature and (b) 200℃.

At room temperature, all CrAlN-Nb samples show slightly higher friction and wear than CrN. At elevated temperatures, CrAlN-Nb coatings show good wear behaviour, but slightly higher friction coefficients than CrN. Increasing the Nb-content results in a higher hardness of the coatings compared to CrN. This in connection with a higher resistance against shear might cause the enhancement of the friction coefficient at room temperature and elevated temperatures. Since the hardness of the CrAlN-Nb coatings increases with increasing Nb-content (see Fig. 4.12), higher abrasion resistance and therefore lower wear should be observed with increasing Nb-content. However, wear seems to increase with increasing Nb content at room temperature. Wear particles should show higher hardness than the surface they originated from, because they underlie plastic deformation before they are formed [33]. The higher the hardness of the surface, the higher should be the hardness of the formed wear particles, and thus, the sample with the highest Nb-content (and highest hardness) shows the highest wear. For longer sliding distances, the wear behaviour might

change, and the sample with highest hardness could show a better wear behavior than the others [33].

Fig. 4.25 shows the friction curves of CrAlN-Re samples tested at room temperature and 200℃ sliding against Al $_2$O$_3$ balls and the friction curves of the CrN sample, which is used as a reference.

(a)   (b)
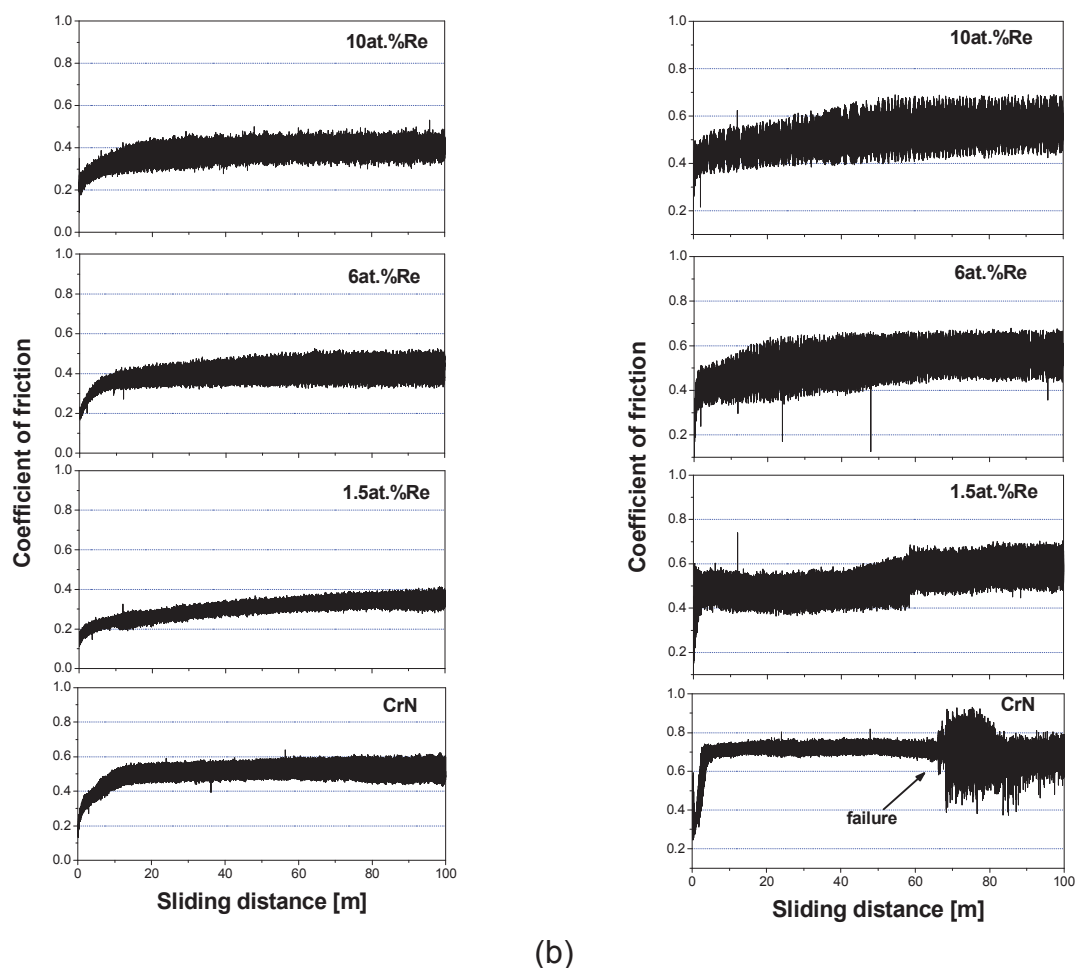
Fig. 4.25 Evolution of the coefficient of friction over a sliding distance of 100 m for CrN and CrAlN coatings with different concentrations of Re tested at (a) room temperature and (b) 200℃ against alumina.

At room temperature, all CrAlN-Re samples show similar friction behaviour. The friction coefficient starts at a value of approximately 0.2 for all coatings. For the CrAlN sample with 1.5 at.% Re, a steady-state coefficient of friction of approximately 0.3 is reached after a long running-in period. The CrAlN samples with Re-contents of 6 and 10 at.% shows a steady-state coefficient of friction in the region of 0.4 after a short running-in period.

At 200℃, the CrAlN sample with 1.5 at.% Re shows a steady-state coefficient of friction of between 0.5 and 0.6 after a short running-in period. The CrAlN sample with a Re-content of 6 at.% reaches a steady-state coefficient of friction of around 0.6

after approximately 30 m sliding distance. The CrAlN sample with 10 at.% Re shows similar friction behaviour. After a long running-in period, a steady-state coefficient of friction of approximately 0.6 is reached.

Fig. 4.26- Fig. 4.28 show 3D-surface profiles for the CrAlN-Re samples at room temperature and 200℃. On the surface of all coatin gs, almost no observable wear tracks are detected. The depth of the wear tracks might be slightly above the surface roughness.

(a)   (b)

Fig. 4.26 3D-wear profiles of CrAlN-Re coatings with 1.5 at.% Re after a sliding distance of 100 m at (a) room temperature and (b) 200℃.

(a)   (b)
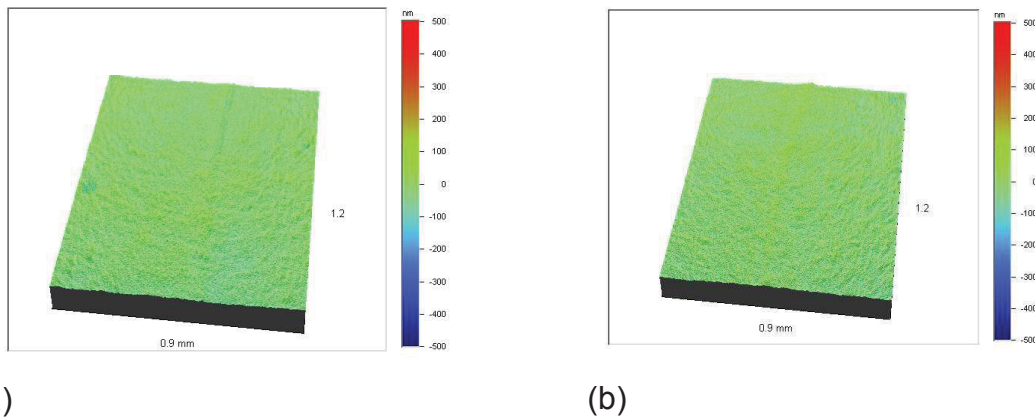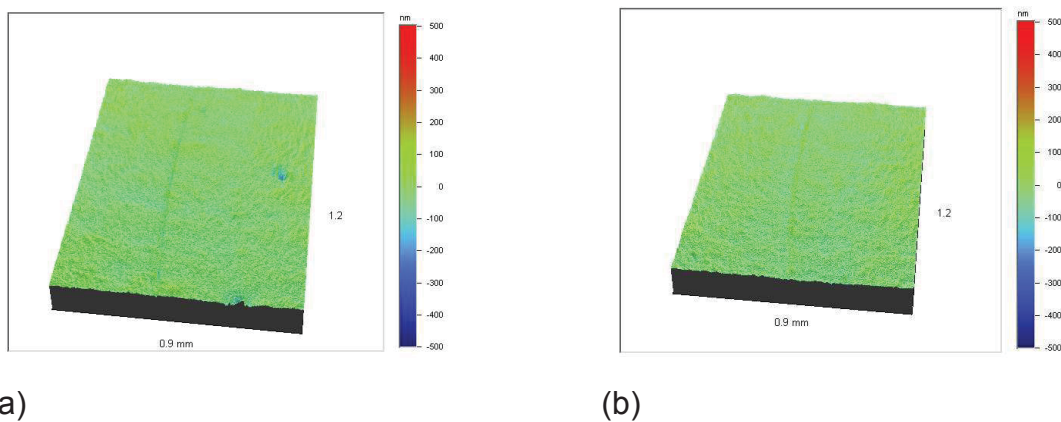
Fig. 4.27 3D-wear profiles of CrAlN-Re coatings with 6 at.% Re after a sliding distance of 100 m at (a) room temperature and (b) 200℃.

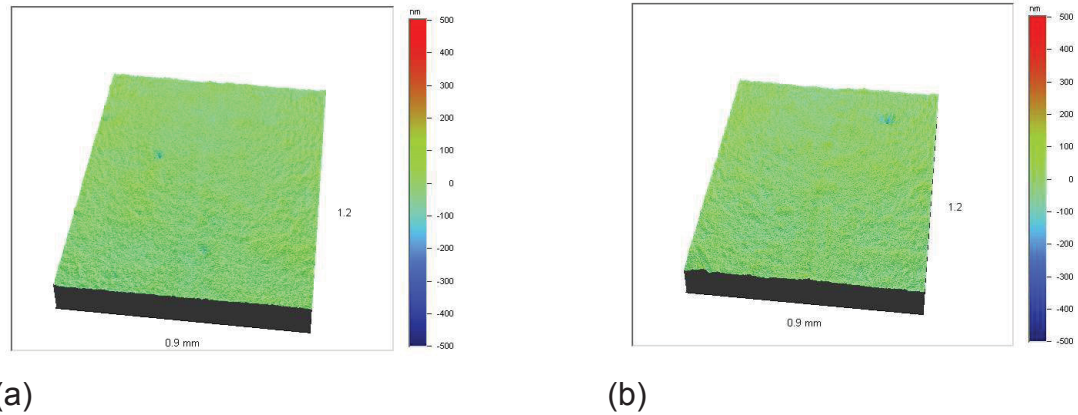(a)   (b)

Fig. 4.28 3D-wear profiles of CrAlN-Re coatings with 10 at.% Re after a sliding distance of 100 m at (a) room temperature and (b) 200℃.

CrAlN-Re coatings show the best tribological behaviour of all samples tested in this thesis. Both friction and wear at room temperature and elevated temperature are lower compared to CrN. Increasing the Re-content yields an increase in the hardness of the coatings, which lies between the hardness values of the CrAlN coating and the CrAlN-Nb coatings (cf. chapter 4.3.5). Theoretically, the Re-containing coating should show less wear resistance compared to the Nb-containing coatings. Nevertheless, the wear as well as the friction behaviour is improved. Maybe oxides with self-lubricating properties like Re_2O_7 are formed [69], which enhance the tribological behaviour of these coatings. Unfortunately, these oxides are too thin to be detected by XRD or Raman spectroscopy, and at this point no clear evidence can be delivered, but should be the content of future investigations.

5 Summary and Conclusion

The aim of this work was the evaluation of new coating concepts for piston rings, where the primary object was the reduction of friction and wear. The presently used CrN coatings show on the one hand good wear resistance at room temperature but on the other hand high wear at temperatures above 200°C due to their open, porous structure. Moreover, they lack self-lubricious properties.

To improve the mechanical and tribological properties of CrN, the addition of high amounts of aluminium to CrN has been quite widely studied over the last years. Hardness as well as oxidation and abrasive wear resistance are improved by alloying aluminium to CrN. The aim of the present thesis is to add low contents of Al to CrN in order to obtain a denser structure with improved mechanical properties and higher oxidation resistance. Ag was chosen as additional alloying element in the CrAlN coating to reduce friction. Alternative choices for alloying were Re and Nb, both might form oxides (Re_2O_7, Nb_2O_5) with self-lubricating properties at elevated temperatures.

The different CrAlXN coating systems, where X stands for Ag, Re and Nb, were deposited by co-sputtering using two CrAl25 targets and either one Ag, Re or Nb target. X-ray diffraction (XRD), energy-dispersive X-ray (EDX) analyses and scanning electron microscopy were conducted to investigate coating composition, structure and phase composition. Moreover, thickness, roughness, adhesion, hardness, elastic modulus and electrical resistance measurements were carried out. Biaxial stress temperature measurements as well as tribological tests were additionally performed.

After finding suitable parameters to deposit single phase fcc-CrAlN with good tribological performance at elevated temperatures, CrAlXN coatings were deposited on HSS and silicon substrates.

For the lowest alloying contents (2.8 at.% Ag, 7 at.% Nb and 1.7 at.% Re), a CrAlN matrix with a solid solution of the fourth element was formed. At higher contents, coatings show a dual-phase structure, where Ag and Re were present as metallic phases while Nb formed the hexagonal ε-NbN phase.

The CrAlN-Ag coatings showed lower hardness and elastic modulus values with increasing Ag-content, whereas for the CrAlN-Nb and CrAlN-Re coatings higher values with increasing amounts of the fourth element compared to CrN were obtained. In the CrAlN-Ag system, this behaviour is related to the formation of the soft face-centered cubic Ag-phase, whereas in the case of the CrAlN-Nb and CrAlN-Re coatings, it is connected to the formation of the harder ε-NbN and hexagonal Re phases, respectively.

The electrical resistance measurements indicated a reduction of the electrical resistance for all alloyed coating systems compared to CrAlN, which is explained by the lower electrical resistance of the additional phases formed.

Biaxial stress temperature measurements from room temperature to 500℃ under vacuum conditions were performed to study the stress evolution in the coatings. In case that an additional metallic phase is formed, the stresses of the as-deposited coatings decrease with increasing content while in case of Nb alloying the opposite behaviour occurred. Stress relaxation due to defect annihilation and plastic deformation of the softer phases started beneath deposition temperature of all coatings. During cooling, thermoelastic behaviour of all coatings was observed until crack formation occurred.

During tribological testing, it could be shown that the addition of 25% Al to CrN yields improved mechanical properties and higher oxidation resistance and thus, better wear behaviour, in particular at elevated temperatures.

The CrAlN-Ag coatings showed slightly improved friction at elevated temperatures compared to CrN due to the presence of lubricious Ag in the sliding contact. Nevertheless, for the formation of effective surface layers, the Ag-content might have been to low.

Alloying by Nb resulted in enhanced tribological behaviour compared to CrN, although no formation of oxides with self-lubricating properties at elevated temperatures could be observed.

The CrAlN-Re coatings showed the best tribological behaviour of all samples tested at any temperature. This might be connected with possible formation of self-lubricating oxides like Re_2O_7.

Finally it can be concluded that the investigated coating systems are possible alternatives to the presently used CrN. Compared to CrN, all coating systems showed improved wear resistance at elevated temperatures. As a consequence of the reduced wear rates, the coating thickness might be reduced compared to the thick CrN coatings in use, which would lead to cost reduction. CrAlN-Nb and CrAlN-Re coatings seem to be the most suitable candidates for a new coating concept on piston rings. However, their real potential might evolve under more severe tribological conditions. To improve the performance of the CrAlN-Ag coatings further, coatings with higher amounts of Ag should be deposited. However, changes in coating architecture by means of a hard interlayer might be necessary to counteract the losses in mechanical stability with higher Ag contents. For doing this, further research activity is definitely needed. Such research might include tribological tests under more severe conditions including higher temperatures and higher loads for the CrAlN-Nb and CrAlN-Re coatings or further investigations about the possible oxide formation on CrAlN-Re coatings.

References

1. A.E. Reiter, V.H. Derflinger, B. Hanselmann, T. Bachmann, B. Sartory, Surf. Coat. Technol. 200 (2005) 2114-2122

2. R. Franz, J. Neidhardt, B. Sartory, R. Kaindl, R. Tessadri, P. Polcik, V.-H. Derflinger, C. Mitterer, Tribol. Letters 23 (2006) 101-107

3. C.P. Mulligan, D. Gall, Surf. Coat. Technol. 200 (2005) 1495-1500

4. R.F. Bunshah: *Handbook of Hard Coatings*, Noyes Publications, Park Ridge, New Jersey, 2001

5. T. Burakowski, T. Wierzchon: *Surface Engineering of Metals: Principles, Equipment, Technologies*; CRC Press, Boca Raton, 1999

6. R.A. Haefer: *Oberflächen und Dünnschichttechnologie*, Teil 1, Springer, Berlin, 1987

7. A. Laarmann, T. Wenz: *Modern Surface Technology,* WILEY-VCH, Weinheim, 2006

8. H. Hofmann, J. Spindler: *Verfahren der Oberflächentechnik*, Fachbuchverlag Leipzig, 2004

9. A. Grill: *Cold Plasma in Materials Fabrication*, IEEE Press, New Jersey, 1994

10. B. Rother, J. Vetter: *Plasma-Beschichtungsverfahren und Hartstoffschichten,* Dt. Verlag für die Grundstoffindustrie, Leipzig, 1992

11. N.B. Chapman: *Glow Discharge Processes*, John Wiley, New York, 1984

12. R.F. Bunshah: *Deposition Techniques for Films and Coatings*, Noyes Publications, New Jersey, 1982

13. K.U. Riemann: in *Hartstoffschichten zur Verschleissminderung*, (eds. H. Fischmeister, H. Jehn), DGM, Oberursel, 1987

14.   B. Window, N. Savvides, J. Vac. Sci. Technol. A 4 (3) (1986) 453-456

15.   I. Petrov, F. Adibi, J.E. Greene, W.D. Sproul, W.D. Münz, J. Vac. Sci. Technol. A 10 (5) (1992) 3283-3287

16.   W.D. Sproul, P.J. Rudnik, K.O. Legg, W.-D. Münz, I. Petrov, J.E. Greene, Surf. Coat. Technol. 56 (1993) 179-182

17.   P.H. Mayrhofer: *Materials Science Aspects of Nanocrystalline PVD Hard Coatings*, PhD-Thesis, University of Leoben, 2001

18.   H. Frey: *Plasmaphysik-Plasmadiagnostik-Analytik*, VDI-Verlag, Düsseldorf, 1995

19.   C.A. Neugebauer: in *Handbook of Thin Film Technology*, (ed. L.I. Maissel), McGraw-Hill, New York, 1983

20.   P.B. Barna, M. Adamik: in *Protective Coatings and Thin Films, Synthesis Characterization and Applications,* (eds. Y. Pauleau, B.P. Barna), Kluwer, Dordrecht, 1997

21.   P.B. Barna, M. Adamik, Thin Solid Films 317 (1998) 27-33

22.   J.E. Greene: in *Handbook of Crystal Growth*, *Vol.1*, (ed. D.T.J Hurle), Elsevier, Amsterdam, 1993

23.   H.A. Jehn: in *Advanced Techniques for Surface Engineering*, (eds. W. Gissler, H.A. Jehn), Kluwer, Dordrecht, Brussels, 1992

24.   P.H. Mayrhofer: Lecture Script *Basics of Deposition and Material Science of Hard Coatings*, 2007

25.   J.A Venables, G.D.T. Spiller, M. Hanbrücken, Rep. Prog. Phys. 47 (1984) 399-459

26.   J.L. Robins, Appl. Surf. Sci. 33/34 (1988) 379-394

27.   J.A. Thornton, Ann. Rev. Mater. Sci. 7 (1977) 239-260

28. B.A. Movchan, A.V. Demchishin, Phys. Metals. Metallogr. 28 (4) (1969) 83-90

29. R. Messier, A.P. Giri, R.A. Roy, J. Vac. Sci. Tech. A 2 (2) (1984) 500-503

30. H. Jehn: in *Hartstoffschichten zur Verschleissminderung*, (eds. H. Fischmeister, H. Jehn), DGM, Oberursel, 1987

31. J.A. Thornton, J. Vac. Sci. Technol. 11 (4) (1974) 666-670

32. P. Blau: *Friction and Wear Transition of Materials*, Noyes Publications, Park Ridge, 1989

33. K. Holmberg, A. Matthews: *Coatings Tribology. Properties, Techniques and Applications in Surface Science*, Elsevier, Amsterdam, 1994

34. K.-H. Zum Gahr: *Microstructure and Wear of Materials*, Elsevier, Amsterdam, 1987

35. N.P. Suh, H.C. Sin, Wear 69 (1982) 91-114

36. B. Bhushan: *Modern Tribology Handbook Volume One*, CRC Press, Boca Raton, 2001

37. M. Moore: in *Fundamentals of Friction and Wear*, (ed. D. Rigney), ASM American Society for Metals, Metals Park, 1981, 73-118

38. E.W. Roberts, Thin Solid Films 181 (1989) 461-473

39. M.A. Sherbiney, J.Halling, Wear 45 (1977) 211-220

40. P. Hedenqvist, M. Ollson, S. Jacobson, Surf. Coat. Technol. 41 (1990) 31-49

41. C. Mitterer, FWF Project proposal, *Low Friction Coatings*, 2004

42. K. Nitzsche: *Schichtmesstechnik*, Vogel, Würzburg, 1996

43. H.P. Klug, L.E. Alexander: *X-ray Diffraction Procedures*, John Wiley, New York, 1974

44.   *Operating instructions*, D500/501 Diffractometer, Siemens

45.   E. Lifshin: *X-ray Characterization of Materials*, WILEY-VCH, Weinheim, 1999

46.   J. I. Goldstein: *Scanning Electron Microscopy and X-ray Microanalysis*, Plenum Press, New York, 1992

47.   *IBIS-UIMS Software Manual,* Fischer-Cripps Laboratory

48.   *IBIS User Guide*, Fischer-Cripps Laboratory

49.   A.C. Fischer-Cripps, Surf. Coat. Technol. 200 (2006) 4153-4165

50.   A.C. Fischer-Cripps, *Nanoindentation*, Springer, New York, 2004

51.   A.C. Fischer-Cripps, P. Karvánková, S. Vepřek, Surf. Coat. Technol. 200 (2006) 5645-5654

52.   H. Oettel, R. Wiedemann, Surf. Coat. Technol. 265 (1995) 76-77

53.   D. Winkler, Diploma Thesis, University of Leoben, 1997

54.   MDC, *Four-point Probe Manual*, Materials Development Corp., Geneva

55.   H. Kuchling: *Taschenbuch der Physik*, Carl Hanser, München, 2001

56.   D. Reitberger, Diploma Thesis, University of Leoben, 2001

57.   Vecco Metrology Group, *WYKO NT1000 Setup Guide*, Version 2.21, 2000

58.   Vecco Metrology Group, *WYKO Surface Profilers- Technical Reference Manual*, Version 2.21, 1999

59.   H. Jehn: *Charakterisierung dünner Schichten,* Beuth Verlag, Berlin, 1993

60.   K. Koski, J. Hölsa, J. Ernoult, A. Rouzaud, Surf. Coat. Technol. 80 (1996) 195-199

61. C. Mitterer, P.H. Mayrhofer, J. Musil, Vacuum 71 (2003) 279-284

62. H. Köstenbauer, G.A. Fontalvo, J. Keckes, C. Mitterer, Journal of Nanoscience and Nanotechnology, accepted

63. H.C. Barshilia, N. Selvakumar, B. Deepthi, K.S. Rajam, Surf. Coat. Technol. 201 (2006) 2193-2201

64. P. Basnyat, B. Luster, Z. Kertzman, S. Stadler, P. Kohli, S. Aouadi, J. Xu, S.R. Mishra, O.L. Eryilmaz, A. Erdemir, Surf. Coat. Technol. (2007), article in press

65. R. Sanjines, O. Banakh, C. Rojas, P.E. Schmid, F. Levy, Thin Solid Films 420-421 (2002) 312-317

66. *Gmelin Handbuch der anorganischen Chemie, Silber Teil A2*, Verlag Chemie, Weinheim, 1970

67. *Gmelin Handbuch der anorganischen Chemie*, *Niob Teil A*, Verlag Chemie, Weinheim, 1969

68. *Gmelin Handbuch der anorganischen Chemie, Masurium und Rhenium*, Verlag Chemie, Weinheim, 1941

69. A. Erdemir, Tribol. Letters 8 (2000) 97-102